Constructing and Testing a Mobile Time-Resolved System to Determine Optical Properties of Breast Tissue In-Vivo

Master's Thesis
by
Magnus Andersson
Anders Nilsson

In the loving memory of our fathers

Abstract

Early diagnosis of breast cancer is very important for the prognosis of any therapy. Existing diagnostic technique, are insufficient. A lot of effort and money has been spent in the research-field of laser application in medicine, to find alternative identification methods for cancer in tissue. Studies have shown that cancer tissue has different optical properties than ordinary tissue, which motivates the constructing of a time-resolved measurement tool, that determines μ_a and μ_s' *in vivo*. This has been acknowledged as a promising method for breast cancer detection.

In this work an instrument, that performs time-resolved measurements, has been constructed in Lund. The goal was to build a portable, silent and easy to handle machine. Measurements of the optical properties μ_a and μ_s' has been performed at Politecnico in Milan on breast tissue *in vivo*.

Contents

List of papers

This Master's thesis is based on the following papers:

Measurements of absorption and scattering properties using time-resolved diffuse spectroscopy – instrument characterization and impact of heterogeneity in breast tissue

Johannes Swartling, Antonio Pifferi, Eleonora Giambattistelli, Ekaterine Chikoidze, Alessandro Torricelli, Paola Taroni, Magnus Andersson, Anders Nilsson, Stefan Andersson-Engels

Additional material has been presented in:

Comparison of spatially and temporally resolved diffuse-reflectance measurement systems for determination of biomedical optical properties

J. Swarling, J.S. Dam, S. Andersson-Engels

1 Introduction

Every year about 1500 women die from breast cancer in Sweden[1]. Today breast cancer is the most common of all cancer forms among women and it is an increasing problem. Mammography offers a good possibility of discovering cancer before it is too late. Even so, this method is not flawless. In some cases women are diagnosed with cancer believed to be due to the mammography treatment itself, which makes the field of breast cancer research extremely interesting and very necessary. Sweden is taking a leading position in general health inspection to prevent late diagnoses. But this does not make the treatment safer. The method itself has a few flaws for example it does not detect all tumours and the contrast is poor. Sometimes the method gives false positives, which means that the breast has to be investigated again[2]. There are a lot of things that are considered to be the reasons why some women develop cancer and some do not. If a woman gives birth to her first child late in life or if she does not give birth at all during her life the risk of developing breast cancer increases. Age is also a factor; the older she becomes the greater the risk for developing cancer. Also overweight may cause cancer in a woman after menopause, but it may have a protective effect on women who are fertile. Inheritance is considered to have a minor effect, which means that the potential risk for women who has a mother or perhaps a sister with this illness not is much higher than for other women. But is there an alternative to mammography? Six alternative methods have been proposed[3]. These technologies include MRI-scanning (magnetic resonant imaging), infrared light scanning, thermography, high definition imaging, blood and urine tests to determine the oestrogen levels. In this thesis red and near-infrared light will be the method used combined with a time-resolved measuring device. The goal will be to measure the optical properties of breast tissue at four different wavelengths, from which one can calculate different interesting parameters.

2 Background

The overall purpose of this Master's thesis is to make an existing time-resolved system mobile, silent and easy to handle. A typical Time-Resolved system is described in the Figure 2.1.
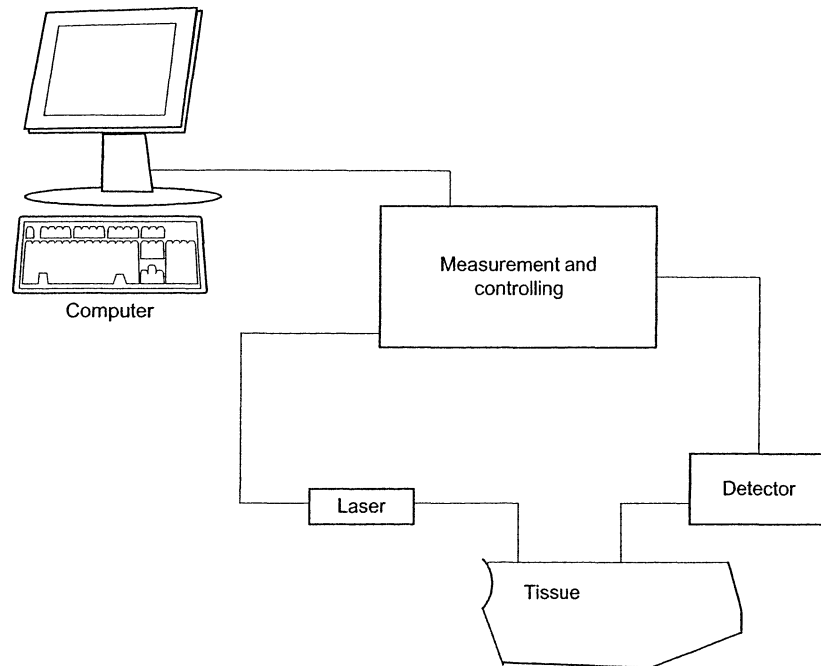

Figure 2.1. The principle of a Time-Resolved system.

In the very beginning there was a stationary system, consisting of one detector with a cooling system and a voltage source, one Ti:sapphire laser pumped by a argonion laser, one rack filled with electronic boxes also containing a constant-fraction discriminator, a multichannel analyser and a TAC (time to amplitude converter). The laser worked at a wavelength of 790 nm and had a pulse width of 100 fs, which is actually very good. But this laser is contained in a large box, about $115 \times 35 \times 20$ cm and which was quite heavy and made it very difficult to move. One possibility at the start was to use a mode-locked argonion laser that was connected to a dye laser, making it possible to change the wavelengths of the light. Such a laser-system is today used in the laboratory in Milan when they examine optical properties[4]. The cooling system of the detector was operated by a coolance-unit from Hamamatsu, which used a Peltier element to cool the detector. A Peltier element uses a current to make one side of the element hot and the other side cold. The cold side is fixed against the detector in the cooling house, while the other side is pointed away from the detector. This side, however, needs to be cooled in order for the element to work properly. Therefore this side was chilled by an internal water system attached to a tap, which made the system even more stationary. The rack contained a few separate boxes, which were quite difficult to calibrate, as each of the electronic devices individually needed to be calibrated.

This made it very difficult to measure the instrumental function of the system. All the electronics are controlled by a stationary computer via a DOS-program made at the end of the 80:s.

A second-generation version of the system had previously been constructed. The system was upgraded by replacing the rack with a box that contained all the previously individual boxes, a GPIB (General Purpose Interface Bus) and a Matlab-program that interpreted the information given by the GPIB. The laser was also changed during this time to a diode laser with a pulse width of 200 ps.

For this Master's thesis work the electronics were replaced by a computer card where all components were integrated, new diode lasers and a flat-screen computer were bought. The computer-card (spc-300 from Becker and Hickl), contained the very same things as its predecessors, the rack system and the upgraded box with a GPIB, but it was much smaller and easier to handle and it contained a program that overviewed it all. The diode lasers were a PDL 808 Sepia from PicoQuant, with four diodes, making it possible to run four different wavelengths at the same time. The computer contained a special box with an ISA-connector, in which the spc-card was placed. This was the initial position for this Master's thesis work.

3 Theory

3.1 Tissue optics

The complexities of tissue can be overwhelming due to being highly inhomogeneous, with many different kinds of structures, and various sizes. For this reason it is difficult to obtain an exact solution for the inverse problem. Inverse problem is when the solution method of the physical problem of light propagation is known, but there is no knowledge about the structure itself. Therefore it is essential to have knowledge of the principles behind light propagation in tissue.

There are quite a few theory models based on different kinds of simplifications, some of those are presented in Welch and van Gemert[5]. When to decide which model fits your problem, one may have to consider the properties of importance. If topics relating to the wave nature of light are to be examined, a model based on the electromagnetic field theory is to be preferred. If, on the other hand, as in this case, the main interest is to study light transport and absorption, averaged over a volume, a model based on transport theory seems to be an accurate choice. In transport theory light is considered only as a flow of energy and the wave nature of the photon is ignored. The basic principle of transport theory is the conservation of energy in every point in space. Within this thesis only models based on the later approach have been treated.

3.2 Optical properties

At the interaction of light with tissue transport theory considers two different kinds of events, absorption and scattering. Normal processes where photons change their energy, e.g. inelastic scattering and fluorescence, are not considered, although it is possible to take such effects into account. To be able to fully describe absorption and scattering three parameters are of major importance: the absorption coefficient, the scattering coefficient and the anisotropy factor.

3.2.1 Absorption

Absorption in tissue is described by the physical coefficient μ_a [mm^{-1}], which is defined as the probability for absorption per unit length of a photon. Absorption means that light energy is picked up, and transformed to another energy shape. The transformation of the energy is often to heat. A possibility for a photon to be absorbed by molecules is carried out by exciting

the molecule to a higher electronic state. To make this possible, the difference between two states has to be equal to the photon energy[6].

If the light is in the region of visible wavelengths, absorption of a photon by a molecule may occur, this type of molecule is often called chromophores. Important chromophores are in tissue e.g. haemoglobin and water. In skin, melanin plays a great part in absorption. A spectrum for some common chromophores can be seen in Figure 3.1.
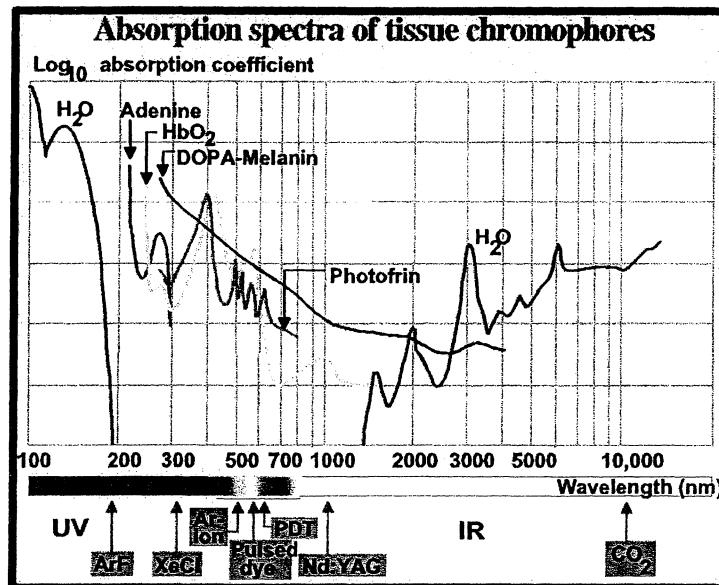

Figure 3.1. Light absorption for different absorbers in tissue[7].

The region that has less absorption is often referred to as the *optical window* in the literature. The optical windows lie in between 660 and 1300 nm. In this particular window the light can probe deep into a lesion.

3.2.1.1 Water

Water is the most common molecule in the body, and it occurs somewhat differently depending on where in the body you are looking. In muscle it can be as high as 75% according to Duck[8]. An absorption spectrum of pure water is shown in Figure 3.2[9,10]. As can be seen the absorption is negligibly small under 600 nm, and above it starts rising with an abortion peak close to 975 nm, and further more peaks, out in the infrared, not shown in Figure 3.2 but in Figure 3.1. Figure 3.2 also reveals that the absorption of water is strong above 950 nm.
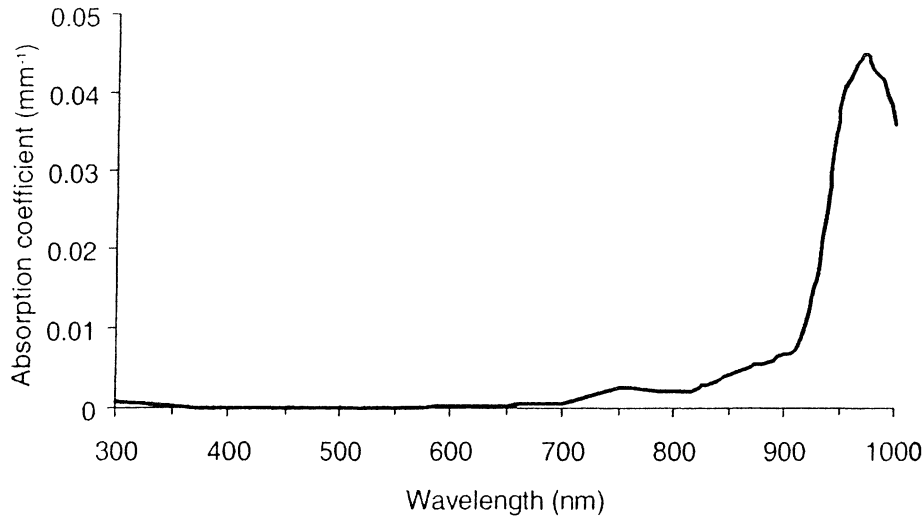
Figure 3.2. Absorption spectrum of water[9].

3.2.1.2 Lipids

There is no large variation of absorption among different types of lipids. Therefore any fat would serve the purpose for basic aspect spectrum. The statement above is true with modification. If you examine lipid in operation theatres by the naked eye, you may see a variation in colour from white to yellow due to the amount of betacaroten. The flat spectrum of the betacaroten absorption may cause factor change, which is negligible in this case. A spectrum showing soya bean oil can be seen in Figure 3.3. It has a high peak at approximately 930 nm and a lower at 760 nm. The appearance of the spectrum can be described as low absorption in the visible wavelength region, and a strong absorption in the near-infrared region. The percentage body adipose tissue is typical in the order of 18% and 29% in normal male and female, respectively Woodard et al.[11] This thesis takes a specific interest in breast tissue. The amount of adipose tissue in the breast varies a lot between individuals, depending on age, hormonal status and general physique of the women.
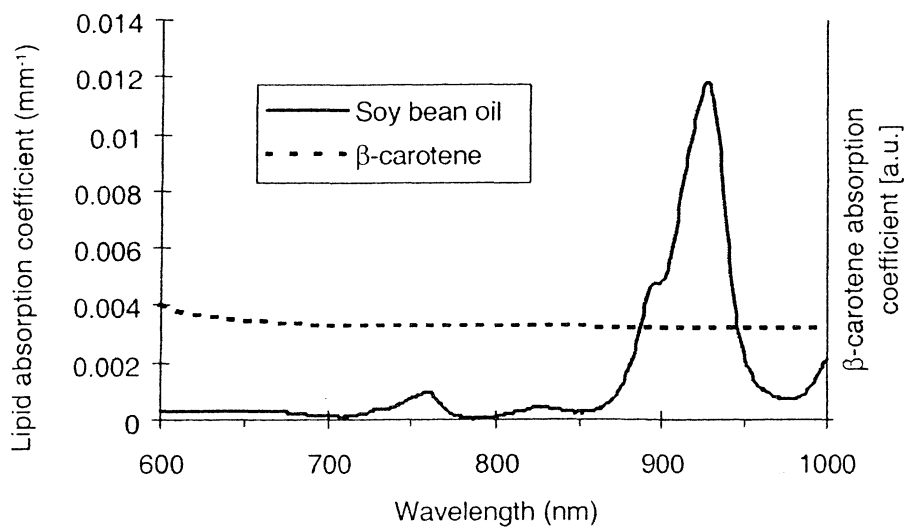

Figure 3.3. Absorption spectrum of soya bean oil and betacaroten[12].

3.2.1.3 Melanin

In skin the pigment melanin has the important roll as nature's sunscreen: It is a large organic molecule that serves the dual purpose of physically and chemically filtering the harmful effects of UV radiation; it absorbs UV rays, causing them to lose energy and it neutralizes harmful chemicals called free radicals that form in the skin after damage by UV radiation. A skin that is too dark blocks the sunlight necessary for catalysing the production of vitamin D, which is crucial for maternal and fetal bones. Accordingly, humans have evolved to be light enough to make sufficient vitamin D yet dark enough to protect their stores of folate. As a result of recent human migrations, many people now live in areas that receive more (or less) UV radiation than is appropriate for their skin colour. That is a possible explanation for the increasing amount of skin cancer. A spectrum of melanin can be seen in Figure 3.4. The spectrum shows that attenuation decreases exponentially with wavelength.
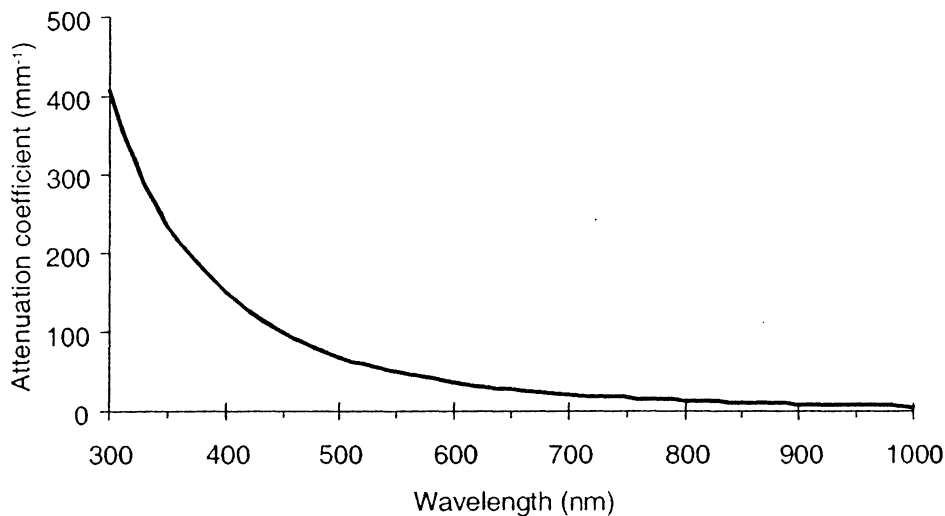
Figure 3.4. Spectrum of melanin in skin[13].

3.2.2 Scattering

Scattering in tissue is described by the physical coefficient μ_s [mm^{-1}], which is defined as the probability for absorption per length unit of a photon. The scattering is divided into two main groups: elastic and inelastic. For the elastic process, energy of the photon is not lost due to change of direction. Scattering such as Reyleigh and Mie are elastic in nature. The Mie scattering occurs when the wavelength of the light is less than particle size that the light is interacting with. The inelastic scattering results in emission of the photon with less energy. Inelastic scattering occurs when the material is Raman active. Illustration of elastic and inelastic scattering can be seen in Figure 3.5.
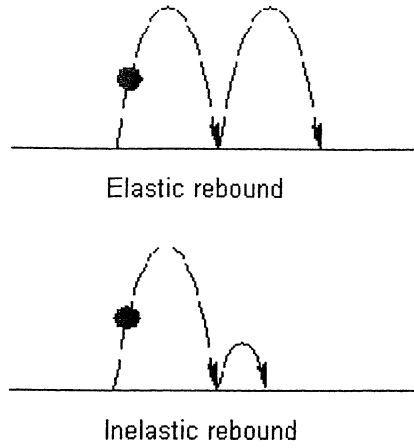
Elastic rebound

Inelastic rebound

Figure 3.5. Elastic scattering; no energy change (atoms or molecules are just points). Inelastic scattering; energy change (internal energy levels of atoms and molecules are excited).

3.2.3 Scattering anisotropy

The anisotropy or, the skew g-factor that one sometimes calls it, is described by means of probability distribution that is depending on the angle between **s'** and **s** according to

$$p(\bar{s}, \bar{s}') = p(\bar{s} \cdot \bar{s}') \tag{3.1}$$
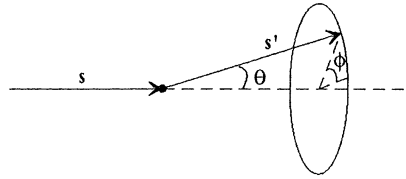
where p(s,s') is the phase function, which describes the probability for light that moves in direction **s** and is going to be scattered in direction **s'**. Probability for scattering to happen is

$$\int_{4\pi} p(s,s')d\omega' = 1 \tag{3.2}$$

where dω' is an infinitely small element of solid angle. The most widely used phase function is the Henyey-Greenstein phase function[14], which has the function form

$$p(\bar{s}, \bar{s}') = p(\cos\theta) = \frac{1 - g^2}{4\pi(1 + g^2 - 2g\cos\theta)^{\frac{3}{2}}}. \tag{3.3}$$

With the above statement leads to

$$g = \int_{4\pi} s \cdot s' p(s,s')\partial\omega'. \tag{3.4}$$

9

3.3 Theoretical model

When you try to find a theoretical model that can describe light in tissue, you may have to consider which way to describe the light due to dualism in physics. The two considerations are:

❖ Light as waves. The light is considered to be electromagnetic waves that are described by Maxwell's equations.

❖ Light as a particle. The light can be considered as a flow of energy particles, photons, that is described by the transport equation where the bottom line is conservation of the energy.

The model that is used in this Master's thesis is the one with light as the particle. The description of light interaction with tissue is based on the fact that the energy is conserved as mentioned above.

3.3.1 Transport equation

Suppose a small volume dV, where a photon penetrates in a certain direction s. This case is studied with the assumption of conservation of the energy. The different possibilities are shown in the Figure 3.6 according to Klinteberg[15].
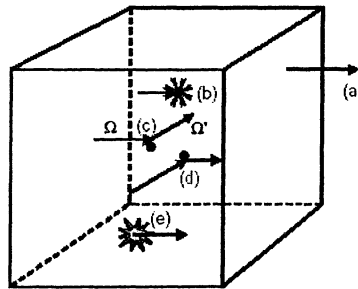

Figure 3.6. A volume where different events occur.

Before a description of the individual contribution in the Figure 3.6 above can be done, some definitions have to be made. Suppose that the photons have no impact on each other: positioning of a photon in space r, of propagation s and in time t, is achieved by a distribution function. This function can easily be related to other optical functions e.g. radiance $L(r,s,t)$ [$wm^{-2}sr^{-1}$]. Quantitative description of the propagation of photon energy is achieved by multiplying distribution function with the speed of light and the energy of the photons.

$$L(r,s,t) = N(r,s,t)hfc \tag{3.5}$$

Useful expressions are fluence rate $\phi(r,t)$ [Wm^{-2}] and photon flux $F(r,t)$ [Wm^{-2}]. The definition of fluence rate is the amount of radiated power on a small sphere, divided with cross-section area of the sphere in mind:

$$\phi(r,t) = \int_{4\pi} L(r,s,t)dw = hfc \int_{4\pi} N(r,s,t)dw \tag{3.6}$$

10

The photon flux is defined

$$F(r,t) = \int_{4\pi} L(r,s,t) \cdot sdw \tag{3.7}$$

If you consider Figure 3.6, the different contribution can be described as follow:

Change due to photon distribution function

$$\int_V \frac{\partial N(r,s,t)}{\partial t} dV \tag{3.8}$$

1. Photon that disappears through boundary

$$-\oint cN(r,s,t)s \cdot ds = [Gaussteorem] = -\int_V cs \cdot \nabla N(r,s,t)dV \tag{3.9}$$

2. Photon that disappears through absorption

$$-\int_V c\mu_a(r)N(r,s,t)dV \tag{3.10}$$

3. Photons that disappear through scattering

$$-\int_V c\mu_s(r)N(r,s,t)dV \tag{3.11}$$

4. Photons that are added through scattering

$$\int_V c\mu_s(r) \int_{4\pi} p(s',s)N(r,s',t)ds'dV \tag{3.12}$$

5. Possible light sources

$$\int_V q(r,s,t)dV \tag{3.13}$$

The addition of the possible events mentioned above lead to the transport equation, basically

$$\int_V \frac{\partial N(r,s,t)}{\partial t} dV = -\int_V cs \cdot \nabla N(r,s,t)dV \tag{3.14}$$

$$-\int_V c\mu_a(r)N(r,s,t)dV - \int_V c\mu_s(r)N(r,s,t)dV$$

$$+\int_V c\mu_s(r) \int_{4\pi} p(s',s)N(r,s',t)ds'dV + \int_V q(r,s,t)dV$$

11

And if the above equation is described with radiance instead, when the expression will yield

$$\frac{1}{c}\frac{\partial L(r,s,t)}{\partial t} + s \cdot \nabla L(r,s,t) + (\mu_s + \mu_a)L(r,s,t) = \mu_s \int_{4\pi} L(r,s',t)p(s,s')dw' + Q(r,s,t) \qquad (3.15)$$

if you drop the volume integrals.

The transport equation is rather difficult to solve analytically. Therefore one may turn to a numerical method such as Monte Carlo, which however is a quite time consuming method. A simplification of the transport equation brings about the diffusion equation, which is a lot easier to solve analytically.

3.3.2 Diffusion theory

The principle behind diffusion theory is to expand the radiance function, appearing in the transport equation, in function series of spherical harmonics (Y_{lm}), see Berg[16]

$$L(r,s,t) = \sum_{l=0}^{\infty} \sum_{m=-l}^{l} \sqrt{\frac{2l+1}{4\pi}} L_{lm}(r,t)Y_{lm}(s) \qquad (3.16)$$

So if you start with transport equation and then expand distribution equation in one isotropic part and one gradient part then you arrive at

$$N(r,s,t) = \frac{1}{4\pi}[\rho(r,t) + \frac{3}{c}J(r,t) \cdot s] \qquad (3.17)$$

A mathematic simplification through integrating equation (3.15) in all direction, leads to

$$\frac{1}{c}\frac{\partial \rho}{\partial t} = -\mu_a \rho - \frac{1}{c}\nabla \cdot J + \frac{1}{c}q_0 \qquad (3.18)$$

where $J = -c\nabla\rho = -cD\nabla\phi$ is Fick's law and

$$D = \frac{1}{3(\mu_a + (1-g)\mu_s)} = \frac{1}{3\mu_{tr}}. \qquad (3.19)$$

It can be seen from above that

$$\mu_{tr} = (1-g)\mu_s + \mu_a = \mu_s' + \mu_a \qquad (3.20)$$

and that

12

$$\mu_s' = (1-g)\mu_s \tag{3.21}$$

The property (3.21) is called the reduced scattering coefficient. It is illustrated in Figure 3.7; where an explanation is also given.
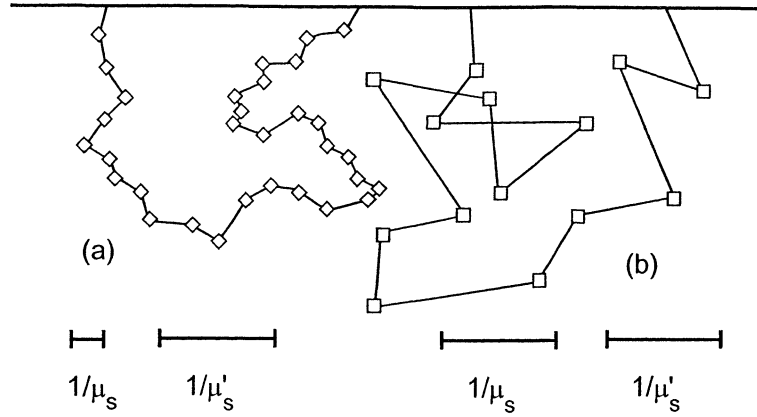

Figure 3.7. The significance of the reduced scattering coefficient μ_s' is illustrated by two photon paths. Path (a) represents a forward-scattered case where g≈0.8, while in (b) g=0 (isotropic scattering). The reduced scattering coefficients are the same (a) and (b), since in (a), the scattering can be regarded as isotropic on the scale defined by $1/\mu_s'$.

Suppose that the medium is homogeneous media. That means that D is constant in the medium, which leads to

$$\frac{1}{c}\frac{\partial\phi(r,t)}{\partial t} - D\nabla^2\phi(r,t) + \mu_a\phi(r,t) = S(r,t) \tag{3.22}$$

Equation (3.22) is the time-resolved diffusion equation that is commonly used when you want to describe light interaction in tissue. The validity of the diffusion equation is restricted by the assumption that the light propagates diffusely, i.e., almost isotropic. This means that μ_s' must be much larger than μ_a.

3.4 Analytic solution to diffusion equation for some different geometries

3.4.1 Infinite homogeneous media

In this case the source consists of a single light pulse, and the light source can be described as

$$s(r,t) = \delta(r)\delta(t) \tag{3.23}$$

According to theory for partial differential equations this gives the solution in form of the Green function[17] as

13

$$\phi(r,t) = c(4\pi Dt)^{-\frac{3}{2}} e^{-\mu_a ct} e^{-\frac{r^2}{4Dct}}$$

(3.24)

3.4.2 Semi-infinite homogeneous media

In this problem you have to consider the boundary between the layers. The index of refraction in tissue is approximately 1.4. The way to go is to extrapolate the boundary and make the fluence rate zero in that boundary. This procedure leads to an introduction of source in the point z_0 and that is mirrored in point $-2z_e\text{-}z_0$, see Figure 3.8. The time-resolved solution looks as follows

$$\phi(\rho,r,t) = c(4\pi Dt)^{-\frac{3}{2}} e^{-\mu_a ct} \left[e^{-\frac{(z-z_0)^2+\rho^2}{4Dct}} - e^{-\frac{(z+z_0)^2+\rho^2}{4Dct}} \right]$$
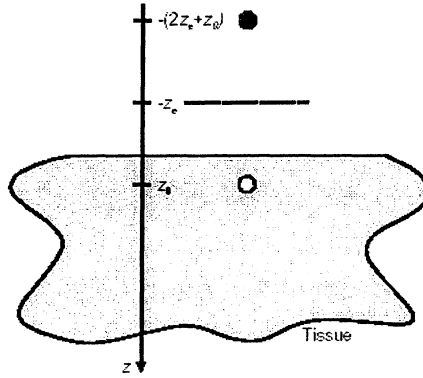
(3.25)

Figure 3.8. Illustration of an extrapolated boundary.

The steady-state solution is

$$\phi(r,z) = \frac{1}{4\pi} \left(\frac{e^{(-\mu_{eff}[(z-z_0)^2+r^2]^{\frac{1}{2}})}}{[(z-z_0)^2+r^2]^{\frac{1}{2}}} - \frac{e^{(-\mu_{eff}[(z+z_0+2z_e)^2+r^2]^{\frac{1}{2}})}}{[(z+z_0+2z_e)^2+r^2]^{\frac{1}{2}}} \right)$$

(3.26)

where $\mu_{eff} = [3\mu_a(\mu_a + \mu_s')]^{\frac{1}{2}}$. If the flux across the boundary is taken into consideration the calculation yields for the diffuse reflectance

$$R(r,t) = -D\nabla\phi(r,s,t) \cdot (-\hat{z})\big|_{z=0}$$

(3.27)

which in the time-resolved case gives

$$R(r,t) = \frac{1}{2}(4\pi Dc)^{-3/2} t^{-5/2} e^{-\mu_a ct} \left[z_0 e^{-\frac{z_0^2 + r^2}{4Dct}} + (z_0 + 2z_e) e^{-\frac{(z_0 + 2z_e)^2 + r^2}{4Dct}} \right] \qquad (3.28)$$

and for the steady-state case

$$R(r) = \frac{1}{4\pi}[z_0(\mu_{eff} + \frac{1}{r_1})\frac{e^{-\mu_{eff}r_1}}{r_1^2} + (z_0 + 2z_e)(\mu_{eff} + \frac{1}{r_2})\frac{e^{-\mu_{eff}r_2}}{r_2^2}]. \qquad (3.29)$$

Equation 3.28 describes the (diffuse) reflected light out of the tissue. This equation will later be used in an iteration of the scattering and absorption coefficients. Through this method, called the Levenberg-Marquardt method, Eq. (3.28) will be fitted to the Temporal Point Spread Function (TPSF), which is going to be explained later on. When a good fit has been done, the calculations of the optical properties are finished.

3.5 Measurement methods

3.5.1 Time-Resolved Measurements

With short pulses in the picosecond region the temporal point-spread function (TPSF) can be measured at different distances from the injection point[2]. This method is called Time-Resolved measurement and is used to determine the reduced scattering coefficient and the absorption coefficient in a small region at different wavelengths. Arrangement of the method is in Figure 2.1.

Information about the optical properties in the region gives not only a clue of what kind of tissue that has been investigated but also about things like oxygen saturation in a tumour[18]. The region is, however, considered to be homogenous, which is a fair thing to presume since tissue locally can be considered to be homogenous. A short pulse is injected into the tissue and the time from when it is injected till it is detected is measured and presented in a histogram. After this procedure has been repeated a few million times the histogram resembles the curve, which is illustrated in Figure 3.10b.

This function is called the temporal point-spread function and it can be investigated by using the Levenberg-Marquardt method[19]. This method uses the iteration of the optical properties to fit the diffuse equation, described above in Equation (3.28), to the temporal point-spread function.

In the Figure 3.10a a picture of how the reflectance is dependent on the inter-fibre distance. Here one can see that if measurements are going to be possible to perform for large inter-fibre distances the input intensity of the light must be rather great, since the reflectance decreases quite a lot with the distance between the injection fibre and the detection fibre.

3.5.2 Frequency-modulated method

Another method that is used with the same application is the frequency-modulated method. Here one uses continuous sine wave as a source and measures the signal at a specific distance. A frequency-modulated set-up is shown in Figure 3.9.
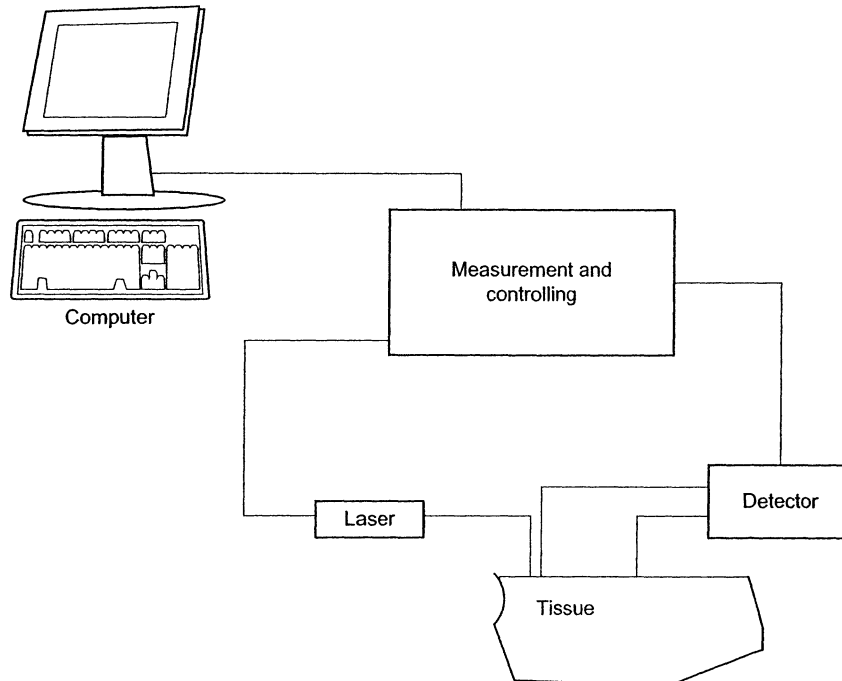

Figure 3.9. A picture of a Frequency-modulated system

A detection fibre is placed close to the injection fibre. This fibre works as a reference fibre, since the detected light within it is quite similar to the characteristics of the injected light. The frequency of the two waves will be exactly the same since nothing in the tissue changes it. The source light will oscillate between a maximum value and zero, while the detected signal never reaches either end, which is quite logical since some of the light detected has taken a longer way through the tissue before reaching the detection fibre. A typical diagram for the reflectance and transmittance is presented in the figure 3.10.
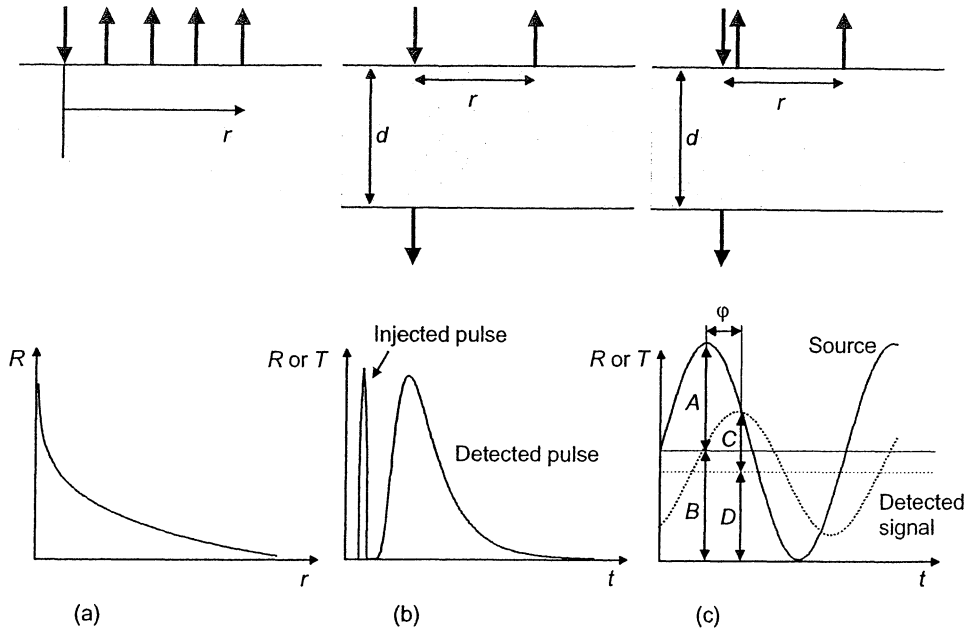
Figure 3.10. (a) The reflectance as a function of the inter-fibre distance. (b) The TPSF technique. (c) The Frequency-modulated method.[2]

Of particular interest is a factor called modulation depth that is defined by:

$$md = \frac{\left(\dfrac{C}{D}\right)}{\left(\dfrac{A}{B}\right)}$$

(3.30)

This factor and the phase shift φ are measured and evaluated to gain the optical properties. Expressions that directly link the measured factors and the optical properties have been developed, based on the diffusion theory[20]. However, if the frequency is too high the modulation depth will be too low, meaning that it will be very difficult to measure and the phase shift will also be quite difficult to measure since it will exceed 2π at some point. At this point the measured phase shift will be very low, since the detector that the shift is supposed to be the measured shift plus 2π. Another disadvantage of this method is that the phase shift is not very easy to measure. In the time-resolved case a change in the inter-fibre distance will be easy to measure, since it is a small interval of time that one measures, for the frequency-modulated case the corresponding interval in phase shift is experimentally more difficult to measure. Traditionally groups in Europe use the time-resolved method, while groups on the other side of the Atlantic use the frequency-modulated method for these biomedical applications.

3.6 Detector theory

Since four different wavelengths are to be used in the machine the spectral response of the detector must be at least between 660 nm and 970 nm. The instrumental response function must be less than 100 ps, which is a chosen number since if the instrumental function is too

wide, the temporal point-spread function (TPSF)[21] for small inter-fiber distances will be, relatively narrow. This is because the TPSF never can be narrower than the instrumental function. The quantum efficiency must be high as well, since the measuring time must be shortened as much as possible. The sensitivity must be so low that single photons can be detected and it has to be fast enough so that approximately 50 million detections can be made in one second, meaning that the rise and fall time must be less than 20 ns. Since dark current is a problem in every detector available it is minimised as much as possible. The active area in the detector must be large enough so that as much of the incoming light as possible can be detected. Since lens technology provides the opportunity to gather the rays into a small spot, the active area criteria can be reduced to the area of the fibre. Another aspect is the size of the entire detector. Since the final version of the machine is supposed to be used during surgery, basically it has to be small. Last but not least the cost of the detector must not be too high.

3.6.1 Photomultiplicator

Since version 1.0 had used a photomultiplicator (*PMT*) it was natural to search for the right detector among other *PMTs*. In a *PMT* an incoming photon uses the photoelectric effect to liberate an electron from a metallic surface in vacuum. This metallic surface is a photosensitive cathode. The electron that is liberated is accelerated in an externally applied electric field. Soon the electron strikes a second metallic surface and causes three to four electrons to liberate from the surface. These electrons accelerate in the electric field and strike a third surface causing the signal to be amplified internally by multiplication. The metallic surfaces after the cathode are called dynodes. Depending on how amplified the signal is going to be a certain number of dynodes are arranged before the final metallic surface is put in. This surface is called an anode, where the signal is finally detected as a current. The designs of some important types of *PMT* are shown Figure 3.11.
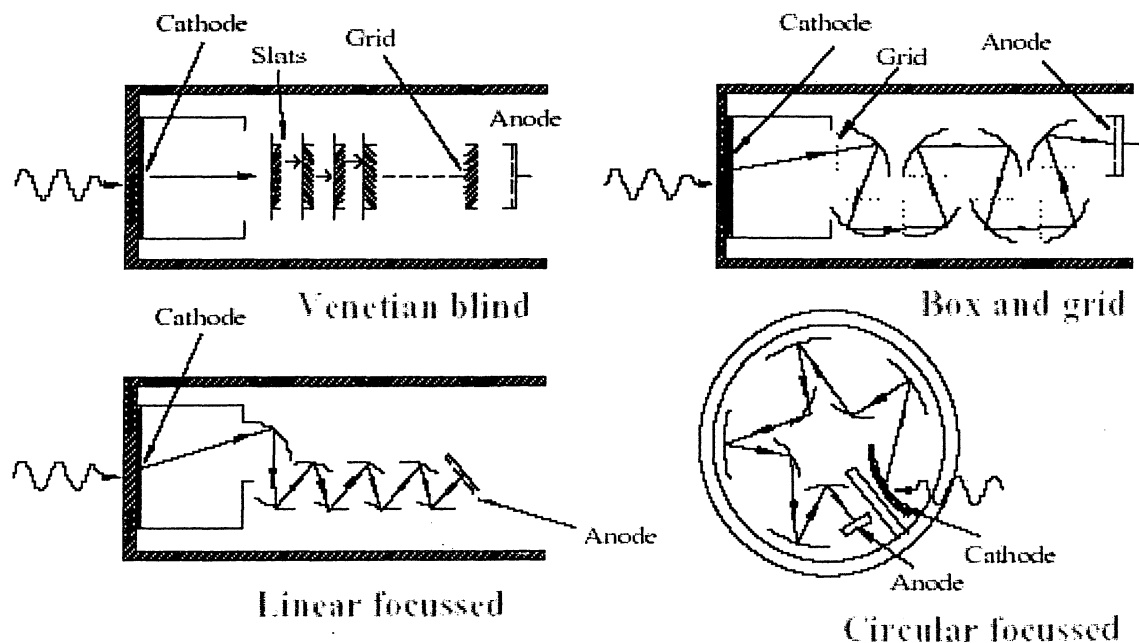

Figure 3.11. The design of four types of PMTs[22].

In order for the first electron to be liberated from the cathode the incoming photon must have a certain energy so that the electron can overcome the electrostatic forces, which form the potential well of the metal. This implies that a *PMT* is not useful if one is supposed to measure the energy of a certain photon. However, the energy of the electrons is statistically distributed, so there is a slight, but not infinite probability, that electrons will escape the metal even if the photon energy falls below the energy needed to overcome the electrostatic forces. This is actually the basic description of how a quantum detector works. Other examples of quantum detectors will be discussed later[23]. When the photon energy approaches the energy of a thermal quantum, kT, the termal noise is high. Therefore, it is very important to cool the detector in this case. *PMT* are very good at single photon counting with instrumental functions as low as 25 ps. The most common problem with *PMTs* are that they have normally have a rather bad quantum efficiency and that they are rather large in size. Since the dark current count is great at room temperature for a *PMT* a Peltier element is used to cool the tube. This introduces another box, which is to be put into the system. In order for the *PMT* to work a voltage of -4200 V must be applied to the tube. Therefore one more box enters the system. In order to make the heat from the Peltier element disappear a water cooling system must be built. Before version 1.0 was designed this system was connected to a tap in the laboratory. So, if a *PMT* is to be used in the instrument, two extra boxes and a water-cooling system is introduced, all adding quite a lot to the weight and size. After reviewing the web for different *PMTs* that fulfil the requirements explained above, only one candidate was left, the R3809U-59 detector from Hamamatsu[22]. Because of this it is interesting and important to try to find an alternative way of detecting single photons in this case an alternative to the *PMT* was searched for.

3.6.2 Imaging detectors

The use of a camera in the optical world has a lot of advantages since it can produce the whole picture. For instance the quite common CCD-camera has many applications for example in the field of fluorescence during PDT (Photo Dynamic Therapy). However they often require a flood of photons to be able to work. This means that the cameras do not count photons because they cannot[24]. This makes this detector useless for this application.

3.6.3 Temperature-sensitive detectors

A temperature-sensitive detector registers a temperature increase due to the incident radiation, by using a sensitive element, which absorbs the incident radiation. The change in temperature is expressed by

$$\Delta T_f = \frac{W_f}{\sqrt{G^2 + (2\pi f H)^2}} \tag{3.31}$$

where W_f is the input power, H is the heat capacity and G is the heat conductivity. In order for the detector to be very sensitive G and H must be small, while the input energy is high. One of the more important criteria was that the detector was fast enough so that it could

detector photons within an interval of 20 ns. The speed criterion of a temperature-sensitive detector is defined by:

$$\tau = \frac{H}{G}$$ (3.32)

which implies that the heat conductivity, H, should be low relative to the heat capacity, G. With the term τ the cut-off frequency can be defined as:

$$f = \frac{1}{2\pi\tau}$$ (3.33)

Hence the desire to have small G and H statistical fluctuations may occur, if G and H are too small, that will influence the measurements. The heat capacity is greatly dependent on the temperature of the material according to the Debye equation for heat capacities[25, 26].

The conclusion of this is that at low temperatures temperature-sensitive detectors can be useful. But since the detector needs to be cooled to very low temperatures, a problem is arising. To be able to cool the detector to these temperatures it is common to use liquid nitrogen. This introduces a problem that makes the instrumentation more complicated to handle, since the nitrogen must be refilled quite often. Therefore a temperature-sensitive detector is not a good choice in this application.

3.6.4 Vacuum photodiodes

The principle of this device is quite similar to the *PMT*. An incoming photon causes a electron via a photoelectric effect to accelerate from the cathode to the anode and the signal is later on detected over a resistance. This device is not at all adapted for single photon counting, since a single photon gives energies that are very difficult to detect. The current that one single electron creates is defined by:

$$i = \frac{e^2 U}{md^2} \cdot t$$ (3.34)

where e is the electron charge, U is the voltage supply over the diode, m is the mass of the electron, d is the distance between the cathode and the anode and t is the time required for the electron to travel from the cathode to the anode. In the Figure 3.12 a simulation of the current as a function of the supplied voltage is shown for ten different d, varying from 100 µm to 200 µm.
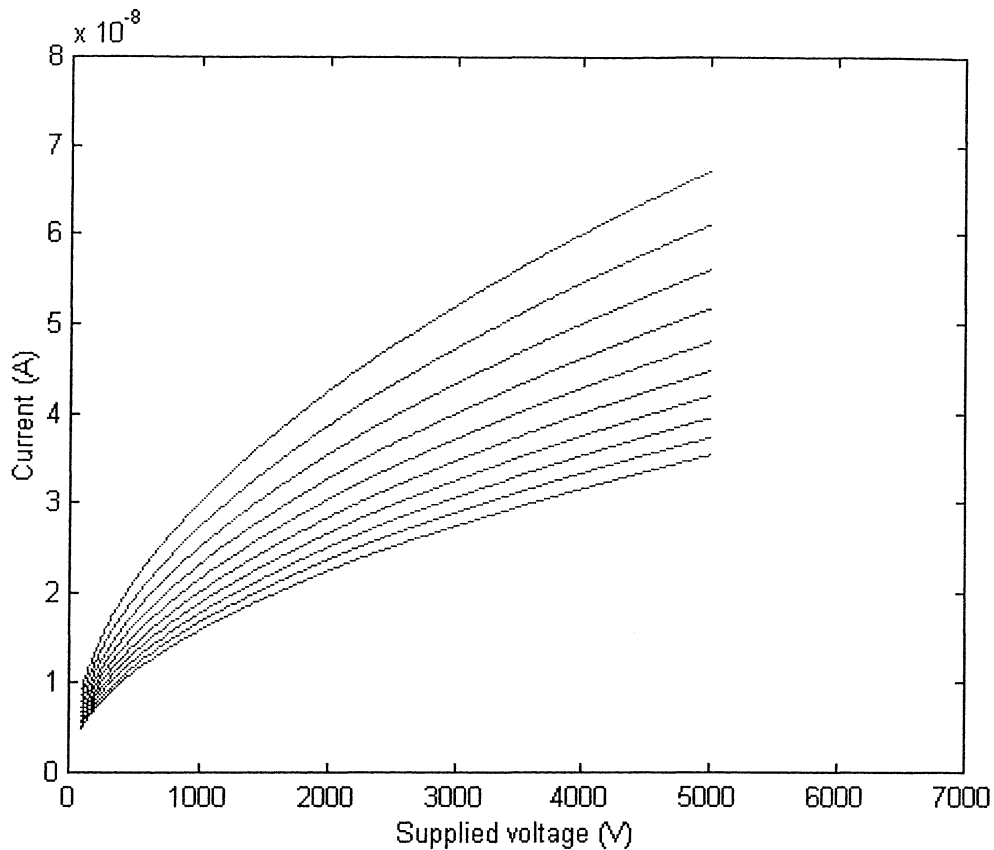
Figure 3.12. Current as a function of the supplied voltage

The curve on the top is equal to the shortest d and the curve below the first one is equal to the second shortest d and so on in the same way. However, diodes with small d, like the ones used in the plot above, are very hard to find. Normally a diode has a d of 2 mm, with a supply voltage of 3 kV giving a current of 2.6 nA. This current is very difficult to detect, since the current has to interact with a resistance to be able to be detected. If the resistance is too high reflections will occur in the circuit, if the resistance is the standard 50 Ω the voltage will be 130 nV, which is not easy to detect if the signal is not pre-amplified. In this case the dark current will also be amplified, which leads to bad results.

3.6.5 The avalanche photodiode

Avalanche photodiodes (APD's) are essentially photodiodes designed in such a way as to have high internal gain. When the photon enters the detector an electron-hole pair is created and the electron is accelerated in a region by an external voltage where it gains enough energy to release further electrons, very much like the multiplying effect in the *PMT*. The greater advantage in this application is that the quantum efficiency is very high, almost approaching 100%. In addition the *APD* are robust, can be made very small and require only small voltages <1 kV. The one problem that is causing many to choose a traditional *PMT* instead of a *APD* is the rather high dark current count at room temperature. Over past few years some progress has been made in cooling *APD's* with an attendant dramatic drop in dark count[27].

There are today no *APD's* that correspond to all the required parameters presented above, because of poor time-resolution.

3.6.6 Conclusion

After reviewing all of the detectors presented above only one detector seemed like a possible choice. The R3809U-59 is a *PMT* with an S1-cathode, which means that the cathode is made of a special material, with the chemical characterisation of Ag-O-Cs. Unfortunately the quantum efficiency is quite low, but still it is the only detector that corresponds to the demands described in the introduction to this chapter. Since this *PMT*, just like the old *PMT*, needs to be cooled to temperatures around -40°C, and the Peltier element in the detector needs to be water cooled. The entire detector system will be as large as it was in version 1.0.

3.7 Fibre theory

The choice of fibres for a time-resolved instrument system with medical applications is very important. Rules in Swedish hospitals say that the gadget brought in to the operating theatre must be at least one meter from the patient, because of electrical safety reasons and that it is difficult to disinfect this type of instruments. Therefore the fibre from the laser and the fibre to the detector must be at least one and a half-meters each, leaving the total length of the fibre at three meters. When the project started the only fibre that was available were step-index fibres with a core of 600 μm in diameter. Here it is important to investigate if the fibre is good enough for the application. NA is the numerical aperture of a fibre and is always described when searching for it in a catalogue. This parameter is defined by:

$$NA = \sqrt{n_1^2 - n_2^2}$$

(3.35)

where n_1 is the refractive index of the core and n_2 is the refractive index of the cladding, as shown in the Figure 3.13.
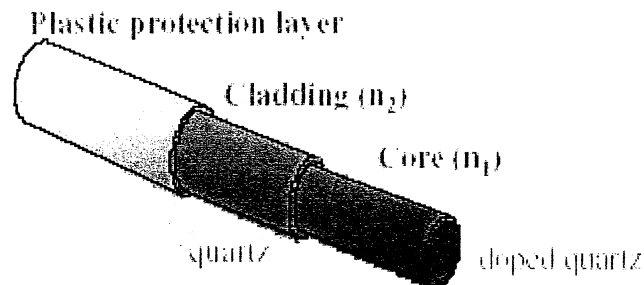

Figure 3.13. The parts of a fibre[28].

The fibre in the beginning of the project had a NA at 0.22. NA also gives a hint about what angles are allowed when the light is about to enter the fibre. Just like a flat waveguide, a circular waveguide (e.g. a fibre) has cut-off frequencies described by a number, V:

$$V = \frac{2\pi a}{\lambda_0} \sqrt{n_1^2 - n_2^2} = k_0 \cdot a \cdot NA \qquad (3.36)$$

where a is the radius of the fibre core. The cut-off frequencies are determined by the zeros of a Bessel equation with the argument $k_c a$, where k_c is the wavenumber of the cut-off frequencies. With V one is able to calculate the number of modes that can be found inside the fibre with the formula:

$$N = \frac{4 \cdot V^2}{\pi^2} \qquad (3.37)$$

When a pulse is sent through a fibre the transmitted pulse will be longer, i.e. wider. This widening is due to three dispersion factors, material dispersion, waveguide dispersion and mode dispersion. The material dispersion occurs because the light source is emitting light within a wavelength region of a certain wavelength. For a step-index fibre the material dispersion is:

$$\Delta \tau_c = -\frac{L}{c} \cdot \frac{\Delta\lambda}{\lambda_0} \cdot \lambda_0^2 \left(\frac{d^2 n_1}{d\lambda^2} \right) \qquad (3.38)$$

where λ_0 is the wavelength, $\Delta\lambda$ is the difference between the upper and the lower limit in wavelength of the region that the light source is emitting light. The λ^2 multiplied with the second order derivative of n_1 is for silica at λ=820 nm approximately 0.024[29]. For a normal laser with a normal fibre of three metres the material dispersion is as small as 0.59 ps, thus making it negligible as the rest of the dispersions are presented.

The waveguide dispersion is due to the fact that light of different wavelengths occupies different space in the fibre and therefore has different speed. It depends on the ratio between the core and the wavelength of light and can be written as:

$$\Delta \tau_W = \frac{L}{c} \cdot \left(\frac{\Delta\lambda}{\lambda} \right) \cdot \left(n_2 - n_1 \right) \cdot D_W \cdot V \qquad (3.39)$$

where D_W is a dimensionless constant. For the same laser and fibre presented above the waveguide dispersion will be about 20 fs, which is even smaller when it is compared with the material dispersion. Since the material dispersion is already neglected due to some other dispersion being much bigger, the waveguide dispersion will also be neglected.

Mode dispersion occurs because of different propagation velocities of the different modes. This factor is defined by:

$$\Delta \tau_m = \frac{L}{c} \cdot \left(n_1 - n_2 \right) \cdot \left(1 - \frac{\pi}{V} \right) \qquad (3.40)$$

For a wavelength at 660 nm V will be about 630 making it possible for approximately 160000 modes to propagate through the fibre. Using this V value one can calculate the mode dispersion for a three meters long step-index fibre to be 167.0 ps, which is considerably larger than both the other dispersion effects. As a comparison the mode dispersion for 970 nm in the same fibre will be 166.6 ps. So the dispersion in the fibre in the wavelength region 660-970nm will be about 167 ps, with the kind of application that is used in this thesis.

Could there be another solution? Is there as a matter of fact something that will decrease the dispersion sufficiently for it to have no impact on the measurements? There are two options. Either one chooses to use a single-mode fibre which removes the mode dispersion or one chooses a graded-index fibre, that has a core with a refractive index that varies decreasingly as the radius increases as the Figure 3.14 shows.
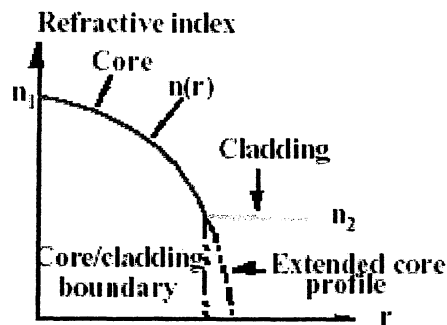
Figure 3.14. The refractive index as a function of the radius in a graded-index fibre[28].

As a single-mode fibre has low dispersion the real problem is that it loses its meaning if one tries to guide four different wavelengths through it, since the number of modes in the fibre is dependent on the wavelength. The criterion is that V has got to be lower than 2.405 in order for the fibre to be a single-mode fibre. But if V is 2.405 then the radius for a single-mode fibre at 660 nm will be 1.15 µm and for 970 1.69 µm, if NA is assumed to be 0.22. This means that the fibre must be at least 0.37 µm wide if all four wavelengths are to go through. But now according to equation (3.37) above N will be 105 for 660 nm, which makes the fibre a multi-mode fibre for this wavelength, thus adding to the mode-dispersion effect again.

The dispersion in a graded-index fibre is described by:

$$t \cdot \Delta \tau = t \cdot \frac{\Delta^2}{2} = t \cdot \frac{\left(\frac{n_1^2 - n_2^2}{2n_1^2} \right)^2}{2} \approx t \cdot \frac{\left(\frac{n_1 - n_2}{n_1} \right)^2}{2}, \quad \text{if } \Delta \ll 1 \tag{3.41}$$

where t is the time the light needs to get from one end of the fibre to the other expressed by equation (3.42) below and n_1 is the refractive index in the centre of the core, while n_2 is the refractive index of the cladding.

$$v = \frac{L}{t} = \frac{c}{n_1} \Rightarrow t = \frac{L}{c} n_1 \tag{3.42}$$

If n_1 is 1.45 and n_2 is 1.43 the time dispersion in a three-meter long graded-index fibre will be 1.4 ps. This is much smaller than the time dispersion for a multi-mode fibre, which makes

the graded-index fibre a natural choice in this kind of application. One major drawback with graded-index fibres is that in a small region the wave will penetrate via tunnelling into the cladding. This means that the mode will eventually lose its energy.

4 Experimental set-up

4.1 Set-up

4.1.1 SPC-Card

The rack in the original system from the end of the 1980:ties was as mentioned before, updated to a GPIB-box and before this project started this part of the instrument was once again updated to a spc-300-card from Becker and Hickl. This card features the very same thing as its forerunner, namely a time-correlated single photon counter (TCSPC), constant fraction discriminators (CFDs), one time-to-amplitude converter (TAC) and a multichannel analyser (MCA). The card is able to tell the Sepia with which repetition frequencies the lasers are going to work. It has a channel resolution that can be as low as 813 fs, making it possible to create curves that are in the interval 0-832.5 ps. Up to 4096 time channels per curve can be used, this makes it possible to measure the four wavelengths with 1024 time channels for each laser, which is more than enough to evaluate the measured curve. The shortest measurement time is 1 ms. Altogether it has a maximum count rate at 8 MHz, which seems small compared to the 80 MHz that the laser can work with. However, the probability of one pulse to be detected is considerably small, therefore the eight million count rate limit is not a problem. The general principle for the SPC card is described in Figure 4.1.
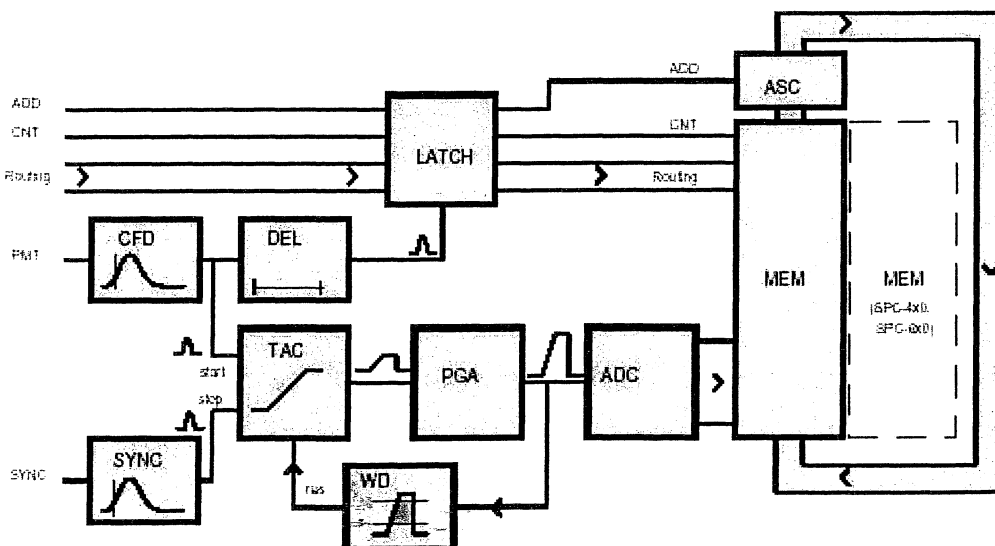

Figure 4.1.The general principle for the SPC card[28].

When the measurement starts the constant fraction discriminator (CFD) delivers a pulse to the time amplitude converter (TAC), which immediately starts to generate a voltage ramp that increases linearly with time. When the pulse is detected the SYNC circuit will deliver a stop

pulse to the TAC, which creates a voltage that corresponds to the time between injection and detection. This pulse is amplified in the programmable gain amplifier (PGA) and later on delivered to the analogue-digital converter (ADC). The ADC converts the amplified TAC-signal into the corresponding address in the memory (MEM). In this address a number between 1 and 255 is added. Values>1 are used to get full-scale recordings in short collection times. In this way the histogram representing the TPSF, described in section 3.5.1, will be created.

4.1.2 Laser source

To be able to use four different wavelengths at the same time it was very important to have a laser source that had four different diode laser heads. Other things that had to be considered were that the diode laser must be able to produce a certain amount of pulses every second in order to achieve fast measuring. The instrumental function must be quite small since the machine will never be able to measure a curve that is narrower than the instrumental function. Of course the laser source must be able to communicate well with the Spc-card and it should also be able to use its four lasers at the same time. According to the datasheet, as provided by Photonic Solutions PLC[31], one can order a PDL 808 Sepia with either four or eight laser drivers. In this Master's thesis a Sepia with four laser drivers was used. This system has user-selectable repetition frequencies of 80, 40, 20, 10, 5 Mhz, which means that the user can select the number of pulses per second that are going to be pumped out of the laser. These frequencies are derived from a crystal controlled oscillator module. The pulse width is 70 ps wide, which is acceptable, since the criterion is set that both the detector and the laser must have an instrumental function that is not wider than 100 ps. This is mainly so that the instrument must be able to measure time-resolved curves with a short (1 cm) inter-fiber distance. The Sepia communicates well with the spc-card and the clever design makes it possible, via a sequencer, to measure with all four wavelengths at the same time.

4.2 Version 1.0

Since time was limited, the first part of the work consisted of making the entire system mobile, so that it could participate in the Milan campaign. Therefore the first order of priority was to get all the pieces to work if it was all placed on a chart. However, two major problems were soon discovered. The box, intended for the measuring card (the SPC-card), on the back of the flat-screen computer, was too small for the application and the cooling of the Peltier element in the detector house, that had originally been connected to a tap. Purchasing a special box that was screwed on to the back of the computer solved the first problem. The card was placed inside this box. Yet the problem of connecting it to the computer remained. A few different suggestions were discussed, when finally the solution of making a flat-cable extender was born. The painful work of welding 200 small spikes to 200 small peeled threads was performed The water cooling system had to be a confined system, so a water pump (from Eheim), some hoses, a radiator (Black ice II from Hardware Labs) and a fan was purchased. The detector was placed in a box and the water was installed. The voltage-unit that is needed to feed the detector, so that electrons are accelerated in the photomultiplicator process, wasn't integrated in this first version of the device. Nor was the cooling-unit, used to cool the

detector to temperatures at -40° C, included inside the box. The cooling- and the voltage-unit were temporarily placed beside the system. An on/off switch was soldered to the laser, but later in Milan this device fell off due to hard handling. A picture of the 1.0 version of the system is shown in Figure 4.2.
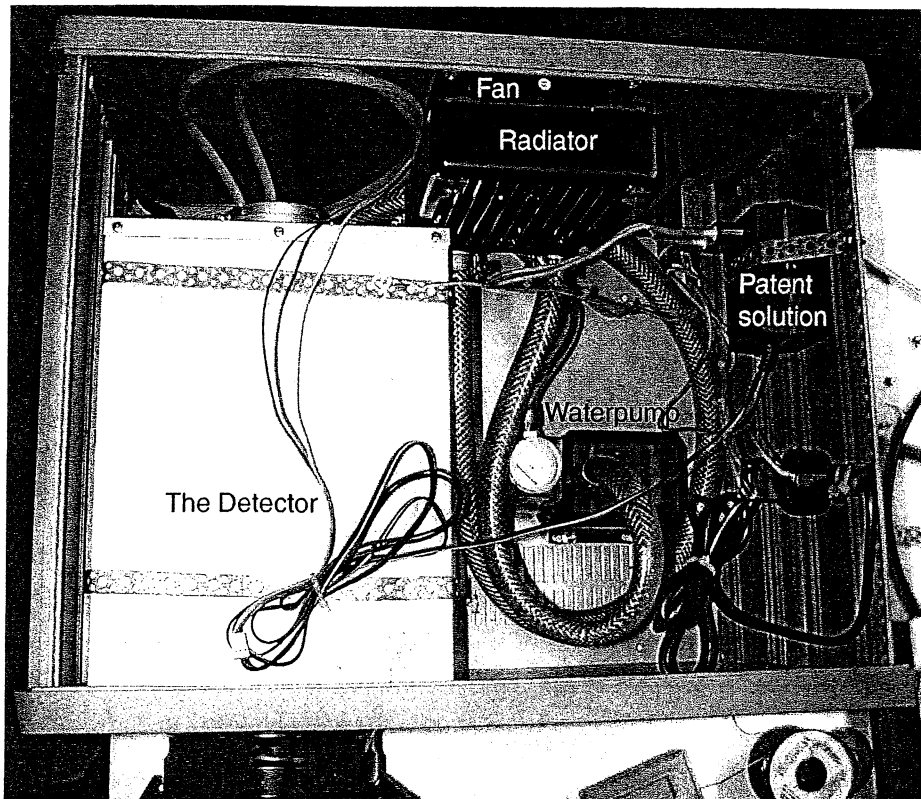

Figure 4.2. Version 1.0. As one can see, it doesn't contain all things necessary if the instrument is going to work. Notice the patent solution on the right of how the 12 V, that the fan needs to work, is created.

4.2.1 Milan

During the two weeks the system and its users spent in Milan, a lot of experience was gained, specially concerning the knowledge about the system's parameters, its function and what could be improved to the final version of the instrument. Results of the measuring will be discussed later on in this thesis. The basic idea was to make the system small, mobile and easy to use, which means that the user should simply be able to press one button and everything would happen automatically. In version 1.0 nothing at all was automatic, which was one of the greater challenges when construction of the final version started after the Milan campaign ended. One of the higher priorities was to get a new detector that responded to a certain amount of parameters.

4.3 Final version

4.3.1 Hardware

The controller system is based upon data acquisition modules from Advantech Co, Taiwan, called Adam 4000-serie. The ADAM Series is a set of intelligent sensor-to-computer interface modules containing built-in microprocessors. They are remotely controlled through a simple set of commands issued in ASCII format and transmitted in RS-485 protocol. Our computer is connected to the RS-485 network with one of its COM ports through the ADAM RS-232/RS-485 converter.

4.3.1.1 Controlling the laser module

Since the laser system is not computer prepared, some modifications had to be made so the laser could be controlled from the computer environment. The easiest way to go was the mechanical, because of a minimal interference of the electrical lasers drivers, to rule out possible noise into the system. The first thing was to control the intensity of the laser. This was previously done manually via a potentiometer. The main modification entails a step motor for controlling the motions forward, backwards, on and off. The motors were assembled to the potentiometers as shown in Figure 4.3 and Appendix A. For holding track of the position of the potentiometer an assembling had to be carried out. The assembling consists of an optical switch that consists of an infrared emitted diode and a phototransistor. To run the motor an electric circuit board was constructed that contained necessary electronic, which can be seen in appendices B. Now, we had the possibility of computer controlling with Adam. Just giving a TTL signal from Adam with one channel, controlling back and forth, and with another channel controlling on and off is feasible.
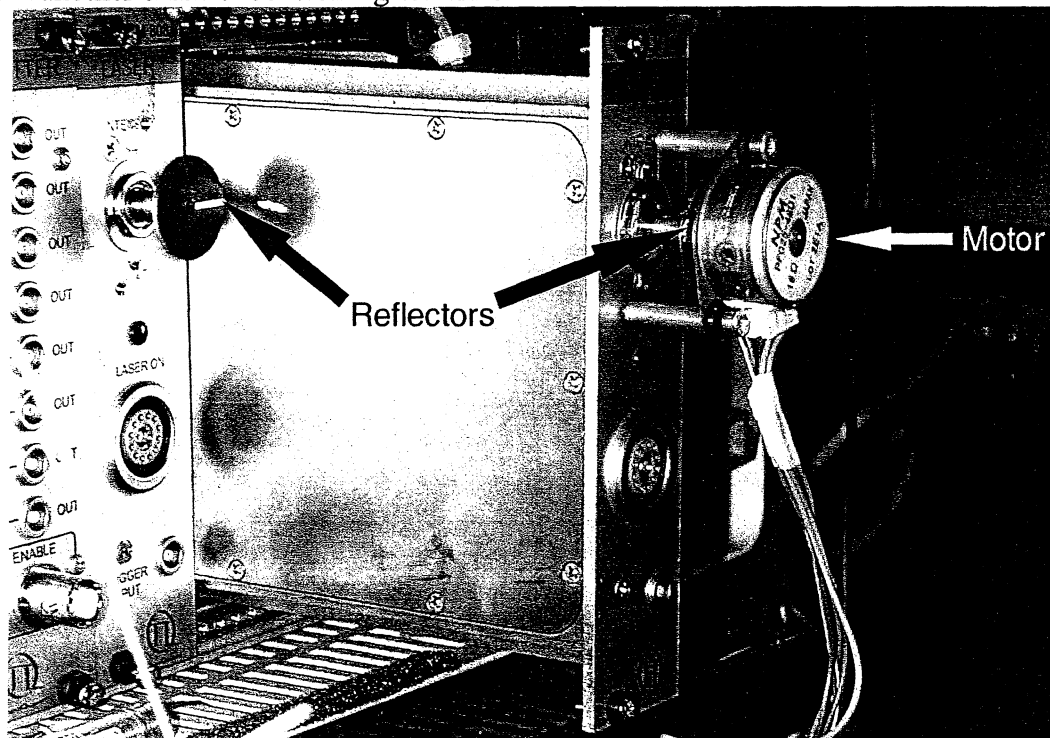
Figure 4.3. A motor and with reflector.

4.3.1.2 Basic configuration and hook-up

Before placing a module in a network, it has to be configured, see Appendix C.

4.3.1.3 Fibre construction

The intention was to have only one fibre out-going and one in-going. The fibre that comes from the tissue sample is only connected to the detector so there is nothing peculiar about that. However, the light from the laser heads is delivered through four individual fibres. So the solution is based on building an attachment of the four smaller fibres into one larger fibre. Four 200 μm step-index fibres made the connection between the four lasers and the external laser-fibre. On one side four SMA-connectors were put on each individual fibre, while all four fibres were put into one SMA-connector on the other side, thus making it possible to put four wavelengths into one fibre. In Figure 4.4 one can see the finished product.
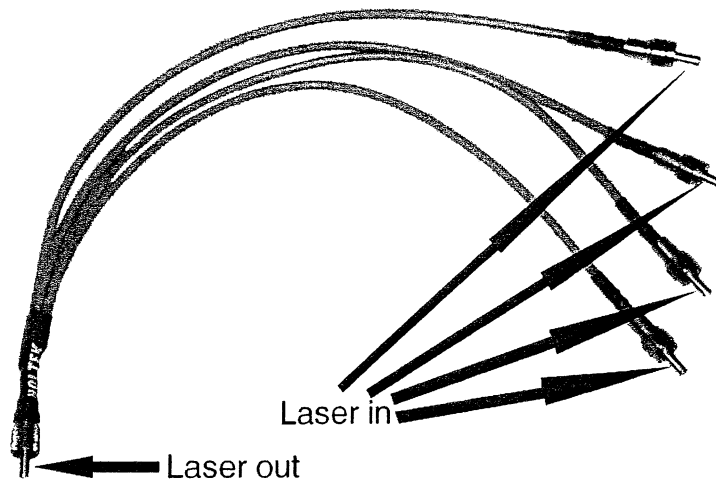
Figure 4.4. The four-into-one laser fibers connector.

In the picture below the connector is shown when it is connected to four fibres on one end and to one fibre on the other end.

Figure 4.5. The four-into-one laser-fibre connector, connected. On the right side the four source fibres are connected and on the left the external fibre.

Nevertheless, one can argue that there will be mode-dispersion in the connector. According to equation 3.40 the mode-dispersion in the connector will be 14 ps, which can be neglected in this application, since the pulse is almost ten times as wide.

4.3.1.4 Power supply

The laser module already contains a power supply and it only needs a connector to the main power supply 230 VAC. For the water-cooling system the water pump can also be directly connected to the main power supply 230 VAC. On the detector side the supply is arranged in the high voltage module and in the cooling module, so they could be connected directly to the main power supply 230 VAC. The pre-amplifier that is attached between the SPC card and the detector demands a voltage of 12 V. This is delivered by a separate voltage supply. The same supply also feeds the fan to the cooling system. Separated supply to the step motors was necessary because of the amount of consumption of current. The Adam system voltage was taken from the laser system voltage supply.

4.3.2 Software

The software can be divided into three main parts: the controlling of the Adam system, the controlling for the SPC-card and the calculation of μ_a and μ_s'. There were two programming languages in use, Labview from National Instrument, USA, and Matlab from Mathworks Inc, USA.

4.3.2.1 Labview

The User Interface was made in Labview, because it is easy to use, Man-Machine Interface (MMI) is a fundamental component in the computer system. It could also be mentioned that the built-in capabilities of communication with peripheral equipment, or at least support by most third party companies, made this program ideal for the task.

Labview is a graphical programming language that makes a distinction from ordinary sequential programming e.g. C, which is based on text file with command rows. A Labview program, called Virtual Instrument (VI), consist of a front panel and a block diagram, see Figure 4.5. On top there is a front panel, in which you define the variables you may use. It is also in the front panel that the variables' values are shown during execution. Under the front panel there is the block diagram, which itemizes all of the programming being done. Graphical representations of functions in the block diagram are wired together so they resemble a flow chart.
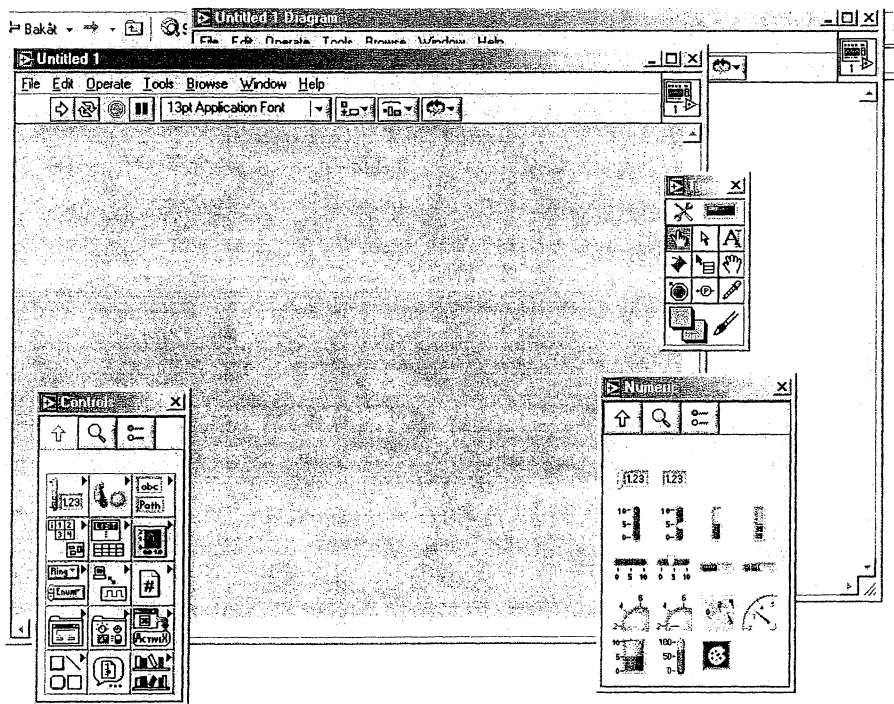
Figure 4.6. Labview, front panel and diagram panel.

4.3.2.2 Matlab

Matlab has a more traditional interface with sequential programming than Labview. This makes it more suitable and handy, for some tasks. Some of the advantages that can be mentioned are, interactive program parcel, suitable technical calculation and visualization of data. Results from reliable calculations can be represented with advanced graphic. The

program parcels are flexible and manageable, and could be used in many applications where the uses of numerical calculations are needed.

4.3.3 Implementation

4.3.3.1 SPC

Included in the shipment of the SPC-card was the 'SPC standard software'. The software provides functions such as set-up of measurement parameters, 2-dimensional and 3-dimensional display of measurement results, mathematical operations, selection of subsets from 4 dimensional data sets, loading and saving of results and system parameters, control of the measurement in the selected operation mode, etc. The SPC Standard Software runs under Windows 3.1, Windows 95/98 and Windows NT/2000/XP. This program works well, but it is difficult to get it to cooperate with other programs mentioned earlier in the thesis. A developed SPC- 32 bits dynamic link libraries (DLL) delivered by Becker and Hickl the same company as the SPC-card, works in the Labview environment. Therefore a program was constructed to fill the space of lack of information exchange. A program is presented in a block diagram in Figure 4.7, which uses some DLL for measurement with the SPC-card.
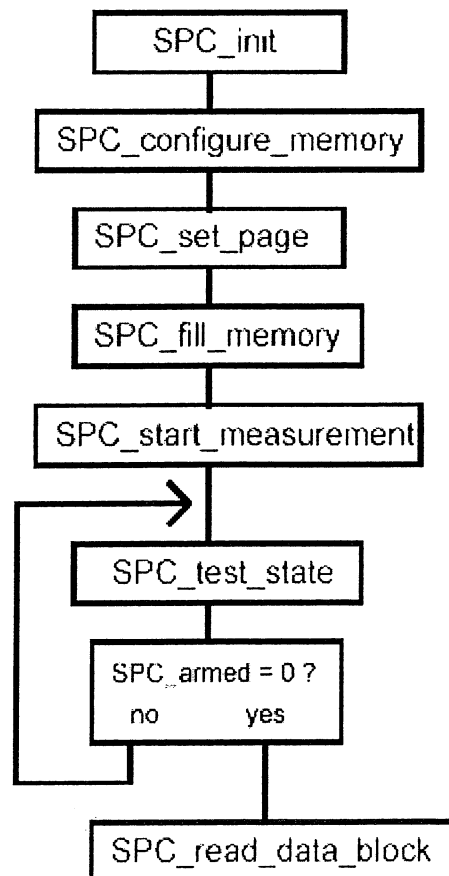
Figure 4.7. A measurement sequence

At the beginning of the sequence the parameters are read from an initialisation file with parameters necessary for the measurement. These parameters are then sent to the SPC module by the SPC_init, and the memory is conFigured by the SPC_conFigure_memory. The data is recorded in memory page, and SPC_set_page sets it. SPC_fill_memory is used to clear the data blocks (normally the current page) into which the data will be measured. When the measurement has been started by SPC_start_measurement a decay curve (or several decay curves if a router is used and no_of_routing_bits was >0 in the call of SPC_conFigure_memory). The measurement runs until a stop condition (specified in the measurement parameters) is reached. In this case the call of the SPC_test_state returns SPC_armed = 0 indicating that the measurement has been stopped and the data can be read from the module memory.

4.3.3.2 Adam

The controlling of the Adam modules was managed by Labview environment. After installation of Advantech's 32-bit Labview drivers in windows, two different sets of VIs are available, easy I/O (Input and Output) and advanced I/O. The easy I/O is a collection of I/O blocks that are used to perform basic I/O operations. The advanced I/O is more flexible than the easy I/O, at the cost of complexity. The advanced I/O is called in a specific order, see Figure 4.8.
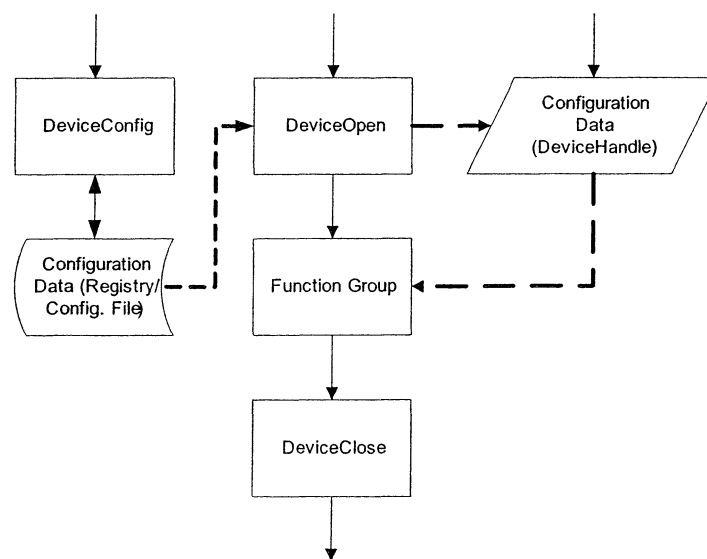
Figure 4.8. Basic flow chart of advanced I/O.

The main program is the one in the middle, which starts with DeviceOpen. The DeviceOpen has the task of opening the device specified by number, which is conFigured when the Adam modular is installed in the system by "DEVINST.EXE". Further down the chart is the function group, which is where the main programming is done. The last thing is the DeviceClose, which is the opposite of the DeviceOpen, it is the closing device. For the thesis a similar flow chart is used, and with function groups. Analogue Output Flow Chart and Digital Input /Output Flow Chart, see Figures 4.9 and 4.10.
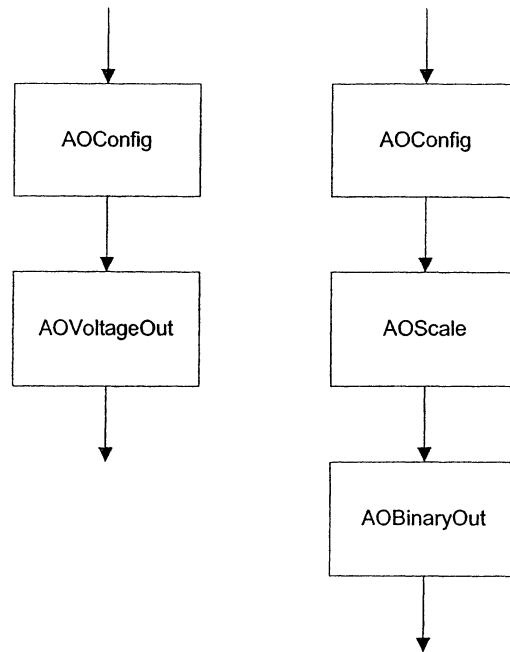
```
            │                           │
            ▼                           ▼
    ┌───────────────┐           ┌───────────────┐
    │   AOConfig    │           │   AOConfig    │
    └───────────────┘           └───────────────┘
            │                           │
            ▼                           ▼
    ┌───────────────┐           ┌───────────────┐
    │  AOVoltageOut │           │    AOScale    │
    └───────────────┘           └───────────────┘
            │                           │
            ▼                           ▼
                                ┌───────────────┐
                                │  AOBinaryOut  │
                                └───────────────┘
                                        │
                                        ▼
```
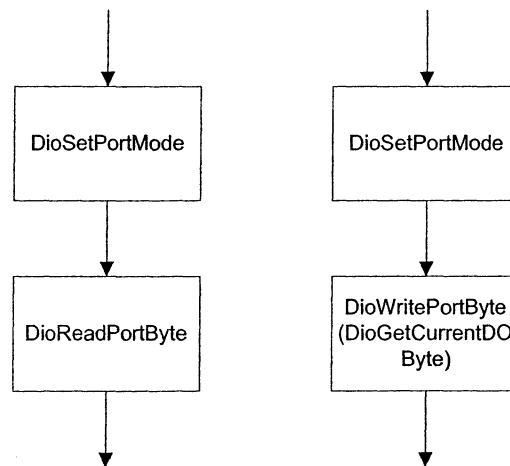
Figure 4.9. Function flow chart, analogue output.

```
            │                           │
            ▼                           ▼
    ┌───────────────┐           ┌───────────────┐
    │ DioSetPortMode│           │ DioSetPortMode│
    └───────────────┘           └───────────────┘
            │                           │
            ▼                           ▼
    ┌───────────────┐           ┌───────────────┐
    │ DioReadPortByte│          │ DioWritePortByte│
    │               │           │ (DioGetCurrentDO│
    │               │           │     Byte)     │
    └───────────────┘           └───────────────┘
            │                           │
            ▼                           ▼
```

Figure 4.10. Function flow chart, digital input and output.

4.3.3.3 Data Evaluation

The fitting was made with Matlab, according to the theory in section 3.4, with the solution of the diffusion equation for a semi-infinite homogenous medium with extrapolated boundary condition. This leads to obtaining absorption and transport scattering, μ_a and μ_s', from measured data. The theoretical curve was convoluted with the instrumental transfer function. This results in a new curve that was fitted to the data over a range starting at 80% of maximum intensity on the rising edge and ending at 1% on the tail. An example is described below in more detail:

First of all the measured data was read, as seen in Figure 4.11.
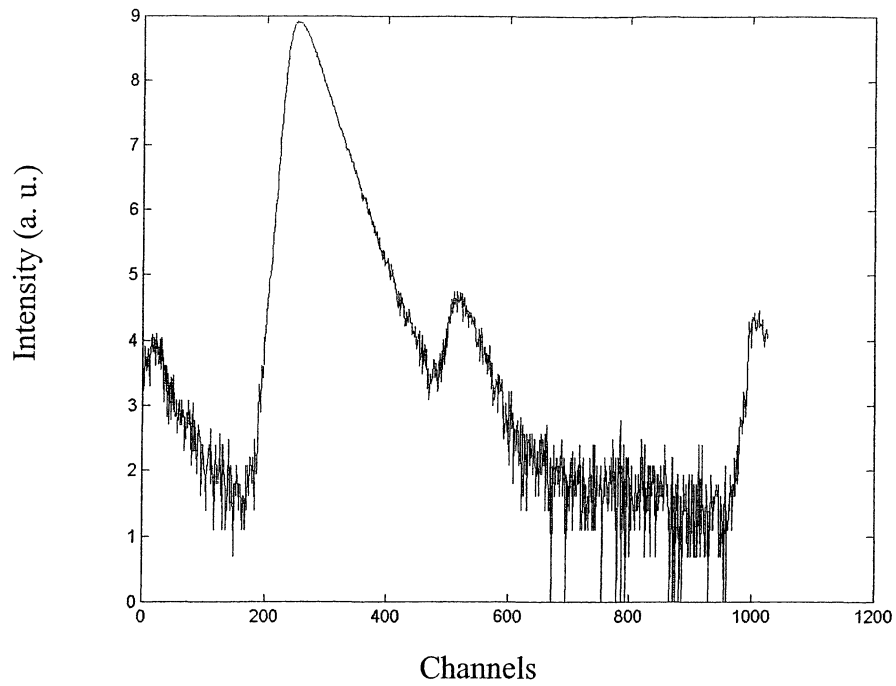
Figure 4.11. Measured data.

To eliminate some of the nois,e a filter was applied which also leads to the reduction of half of the channels, which can be seen in the Figure 4.12.
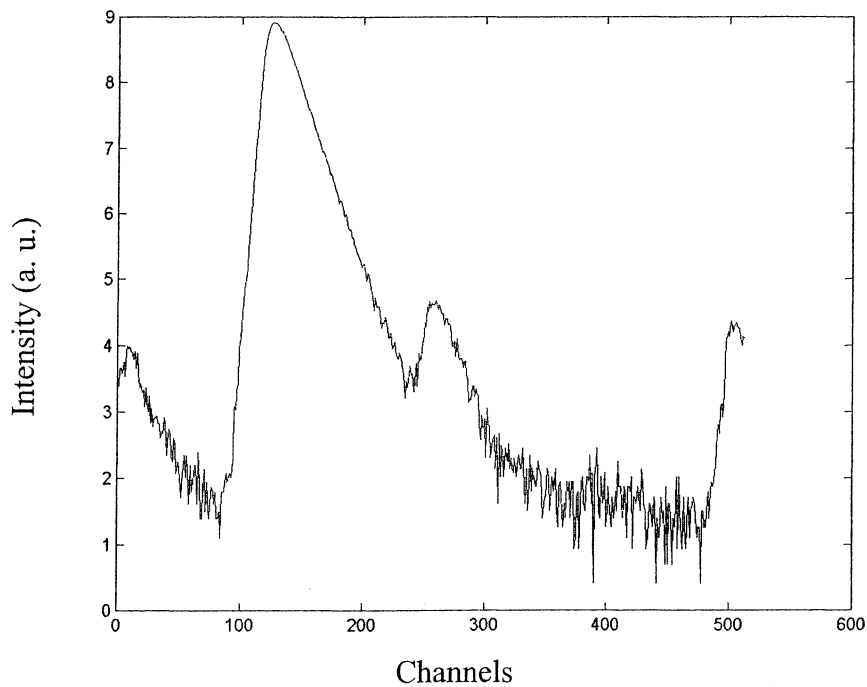
Figure 4.12. Filtered data.

The next data set to be read is the instrument response function as can be seen in Figure 4.13. This curve also went through the noise filter.
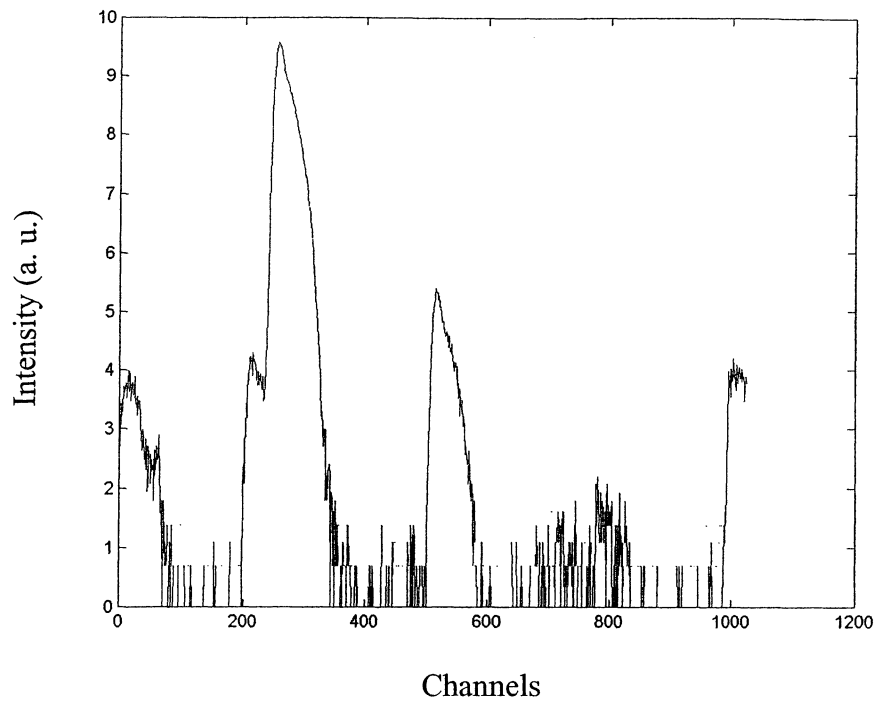
Figure 4.13. Instrumental response function.

To eliminate the problem that the two data curves do not have the same amplitude (they may have, but normally do not) they have to be normalised. It can be seen in Figure 4.14 and 4.15.

Channels
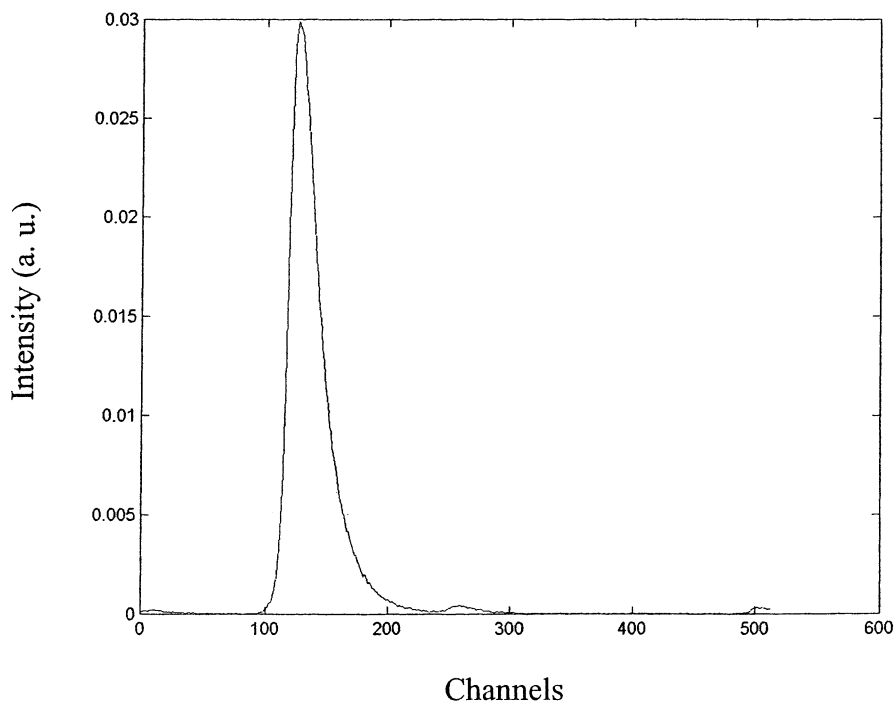
Figure 4.14. Normalised data.
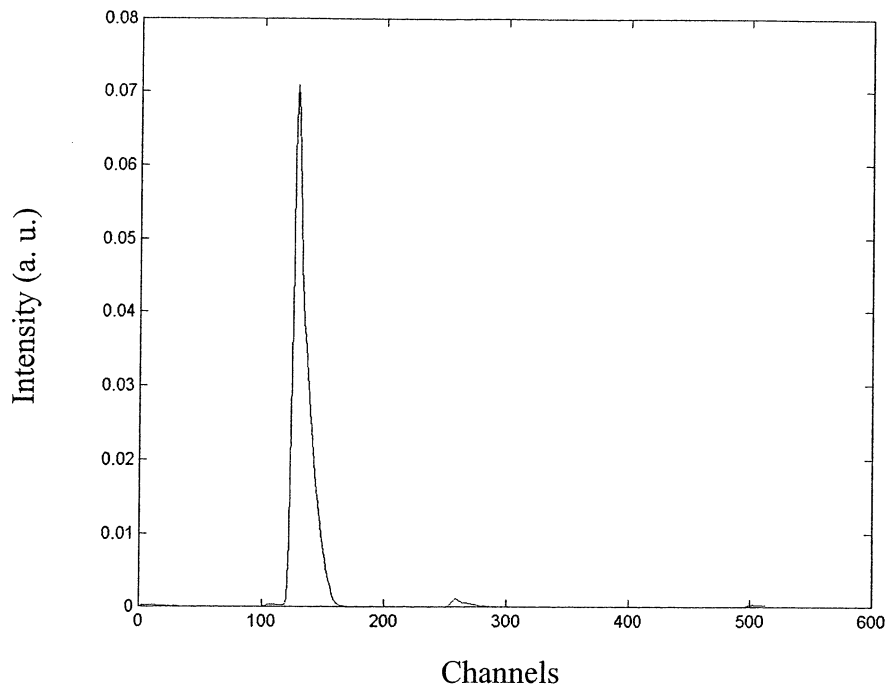
Figure 4.15. Normalised instrumental response function.

At present all is set for the convolution of the data and the instrument response function. The result is shown in Figure 4.16.

Channels
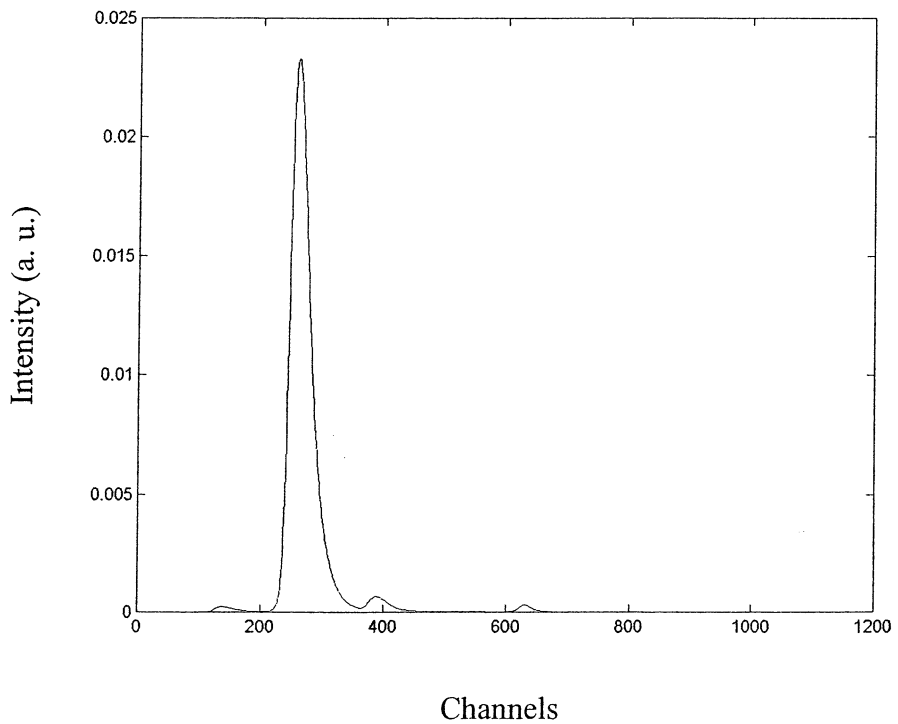
Figure 4.16.Convoluted data.

The fitting was achieved by varying μ_a and μ'_s achieved via Levenberg-Marquardt algorithm. The Matlab routine LSQNONLIN was used to incorporate the Levenberg-Marquardt algorithm. A result can be seen in Figure 4.17.
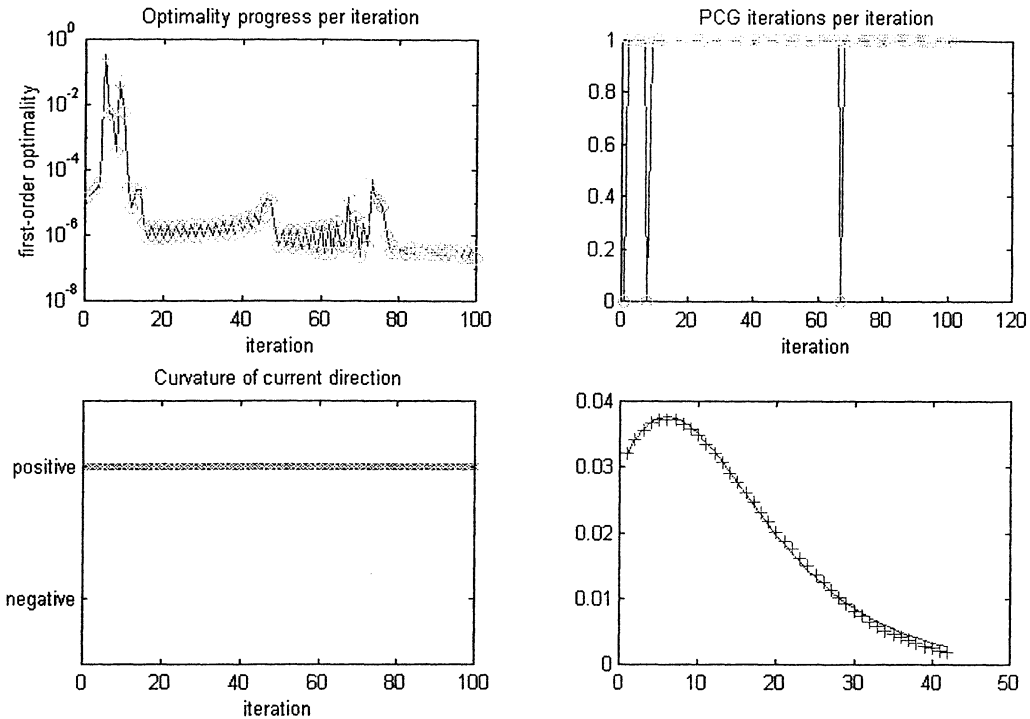
Figure 4.17. Picture bottom right shows fitted theoretical curve to measured data, + measured data and continuous line the diffusion equation.

4.3.4 Assembling of all the parts in the box.

The initial request was that the system should be as small as possible. A special box was ordered from ELFA that measured $520 \times 290 \times 490$ mm^{32}. The entire system, except for the computer of course, was meant to be placed inside. However this required a lot of modifications to the system, some explained above. The first problem was where the detector and the water- cooling system were going to be placed. Different suggestions were made with the detector on the floor and the waterpump mounted on the inside of the top lid with the detector on top and the waterpump on the floor to prevent any damage to the electronics if it should break down. These suggestions were not good enough as one should be able to remove the top lid without any difficulty. Thus a new solution was constructed, where the detector was placed on four rods and therefore space was created under the detector where the waterpump and the hoses from the rest of the watercooling system could be placed. This also made it possible for the ADAM-controlling devices to be placed here and so creating a two-plane solution for this side of the system. The other side of the system was also divided in two planes, but in a more concrete way. A stripped version of the Sepia was placed on the floor, next to the detector. Onto this a metal plate was placed containing stripped versions of the

voltage unit and the cooling unit. On this four cardholders with the step-motor-drivers were added and a transformer that transforms 230 V to 12 V. On the front of the box four holes were drilled in which two light emitted diodes (LED) and two SMA-SMA-mating connectors were placed. The LEDs indicate when the machine is on and when the laser is on, while the SMA-SMA-mating connectors form the joint between the inner and outer fibre system. On the back of the box a power switch, one RS232-connector and one radiator with a fan. The power switch is the main switch for the entire system. In this assembly a 2 A fuse is placed. The female RS232-connector communicates with the computer via the serial com-port. This makes it possible to control the Adam-units in the instrument. Because of the limited space inside the box the radiator and the fan were placed on the back. Now follows a collage picture that describes how the instrument is assembled.
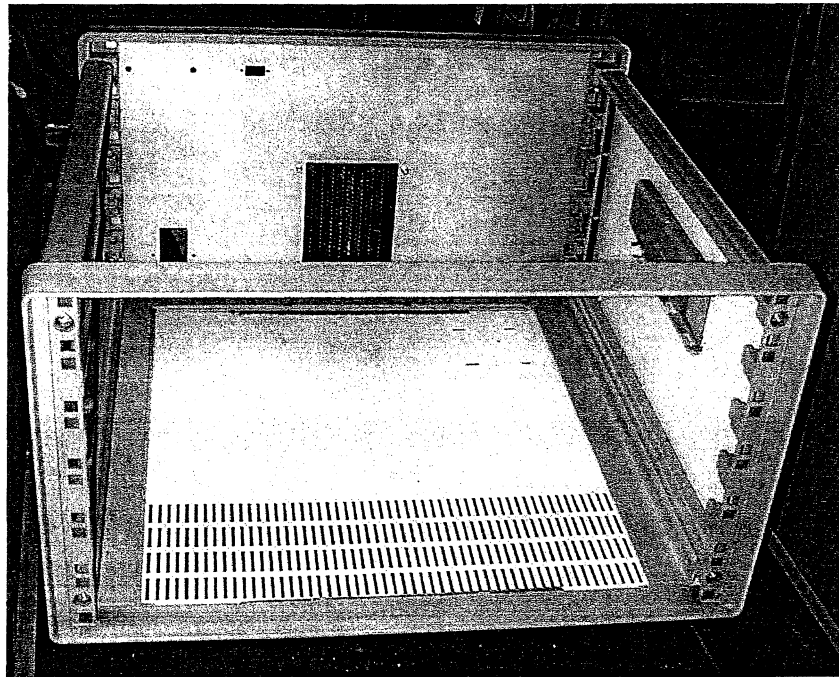
Figure 4.18. Side view. The box before.
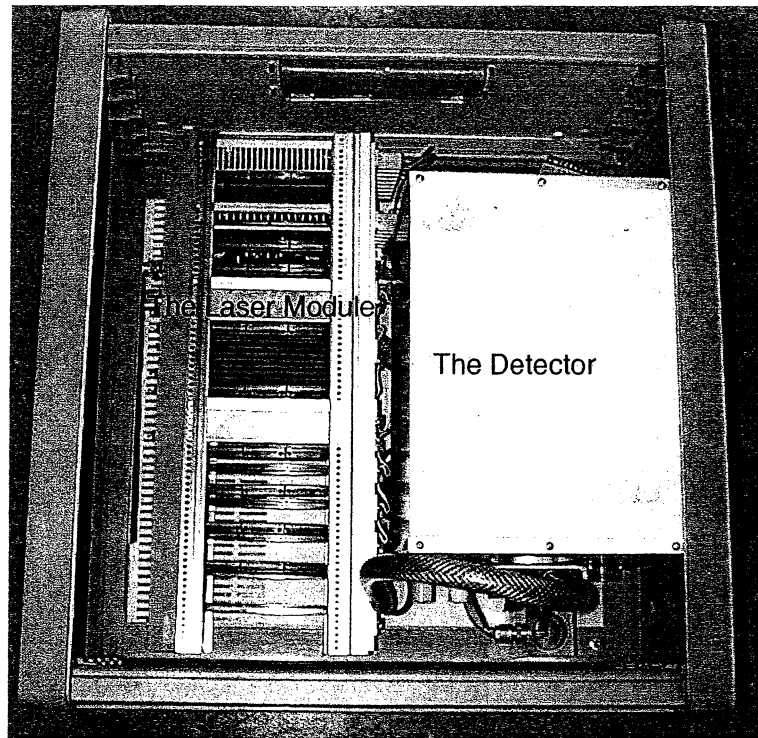
Figure 4.19. Top view. The placement of the detector and the laser.
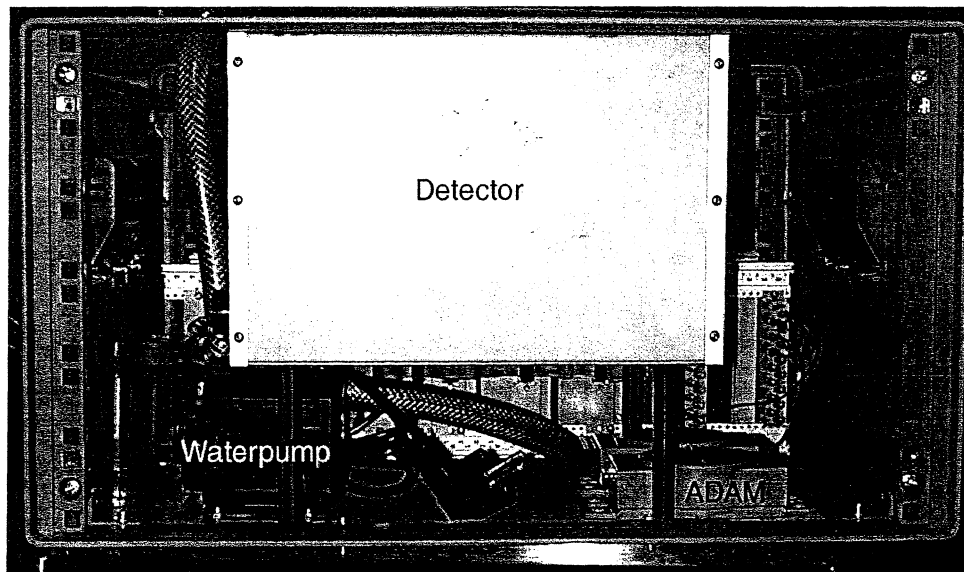
Figure 4.20. Side view. The placement of the waterpump and the rod-solution for the detector.
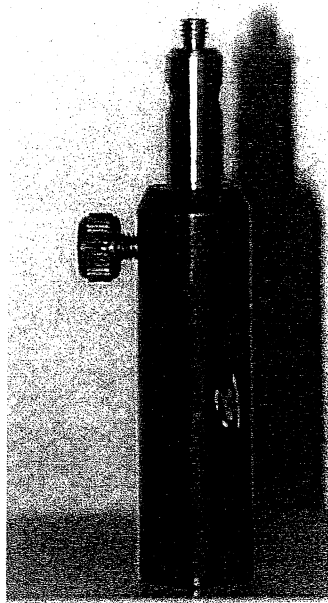
Figure 4.21. The first version of the rods to the detector solution.

Figure 4.22. The back of the box.
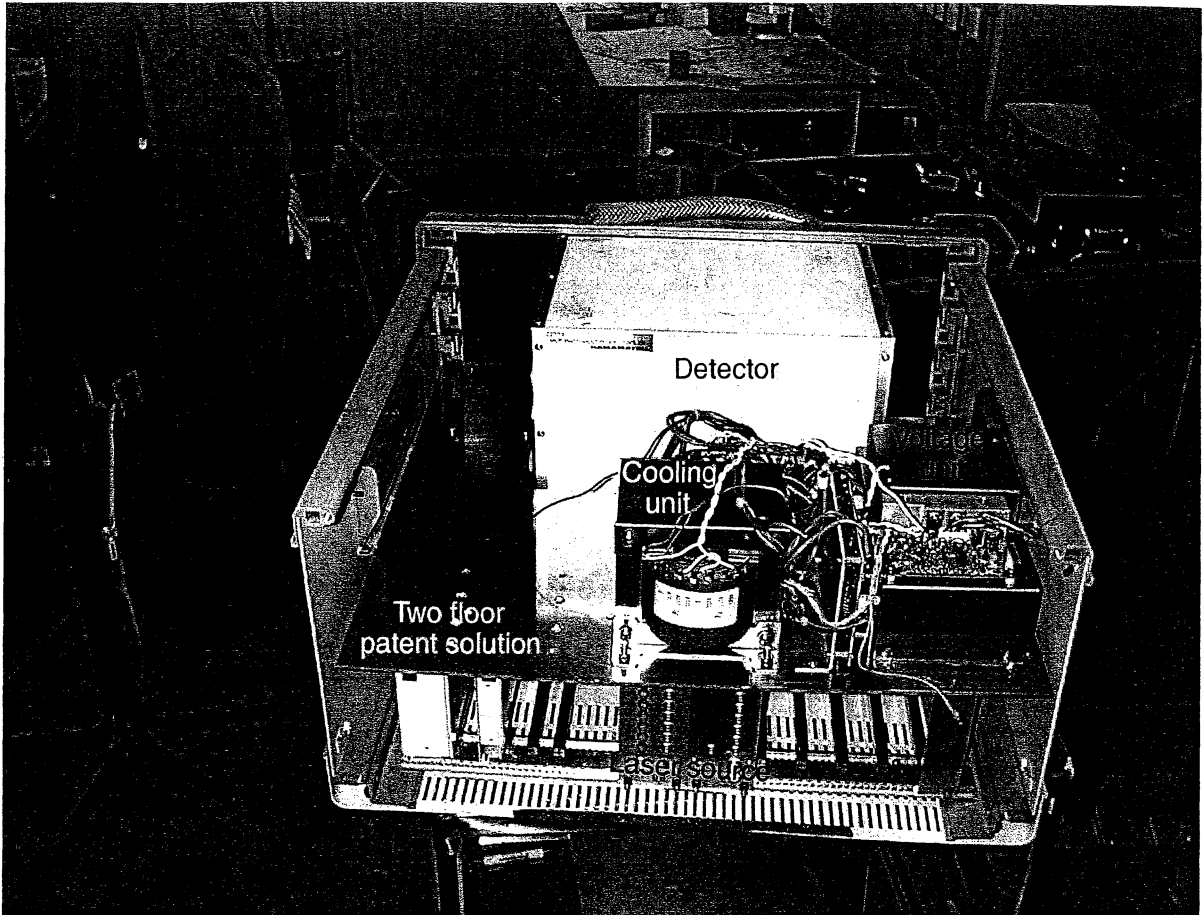
Figure 4.23. The two floor solution with the stripped versions of the voltage unit and the cooling unit installed.
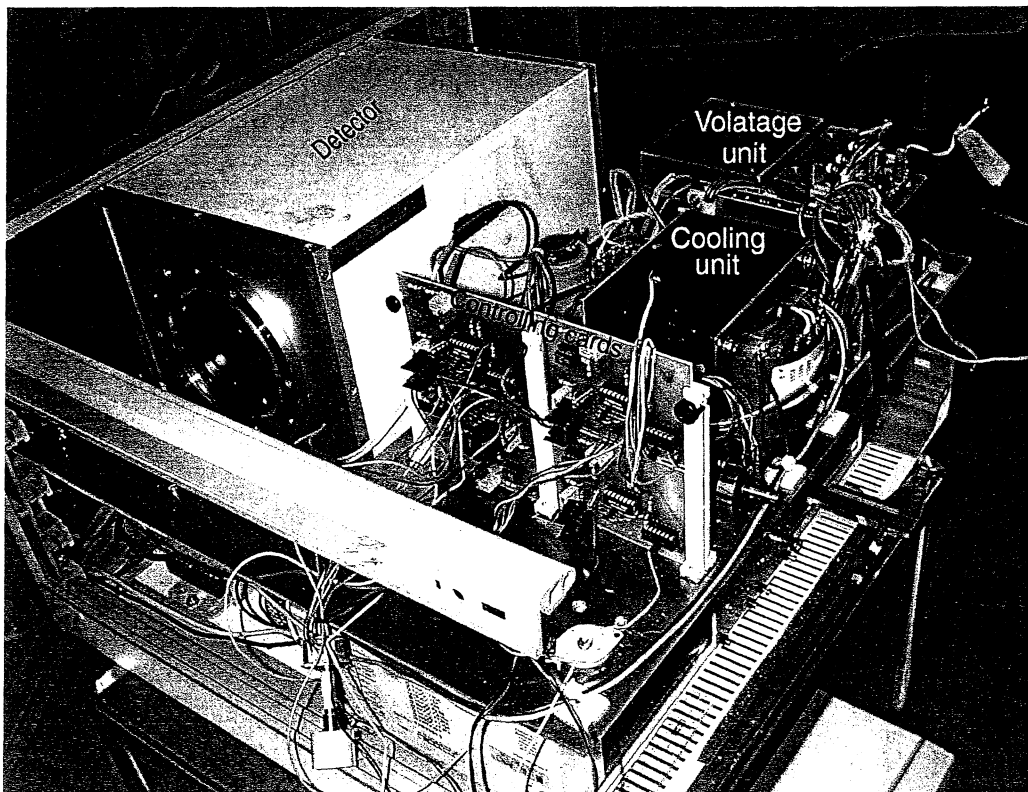
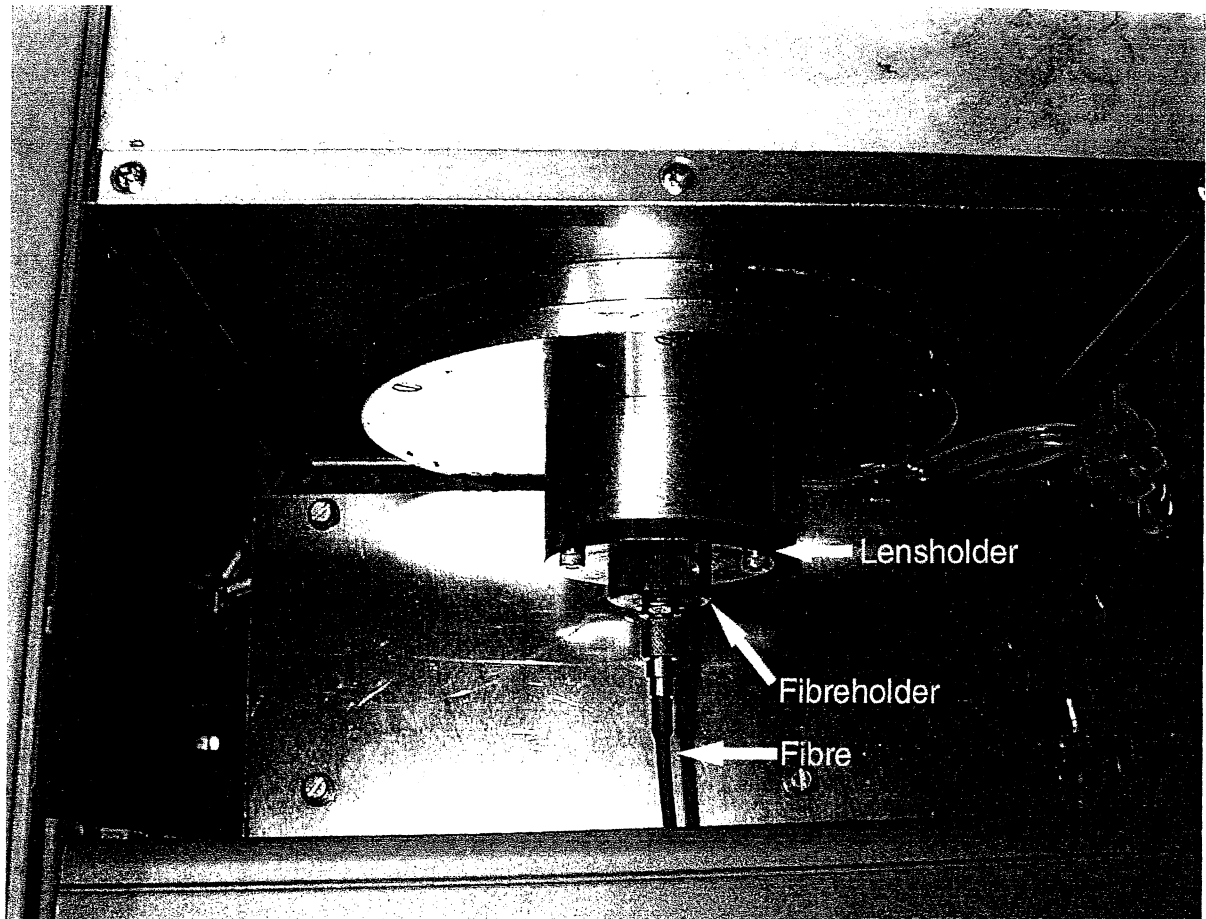Figure 4.24. The placement of the controlling cards.
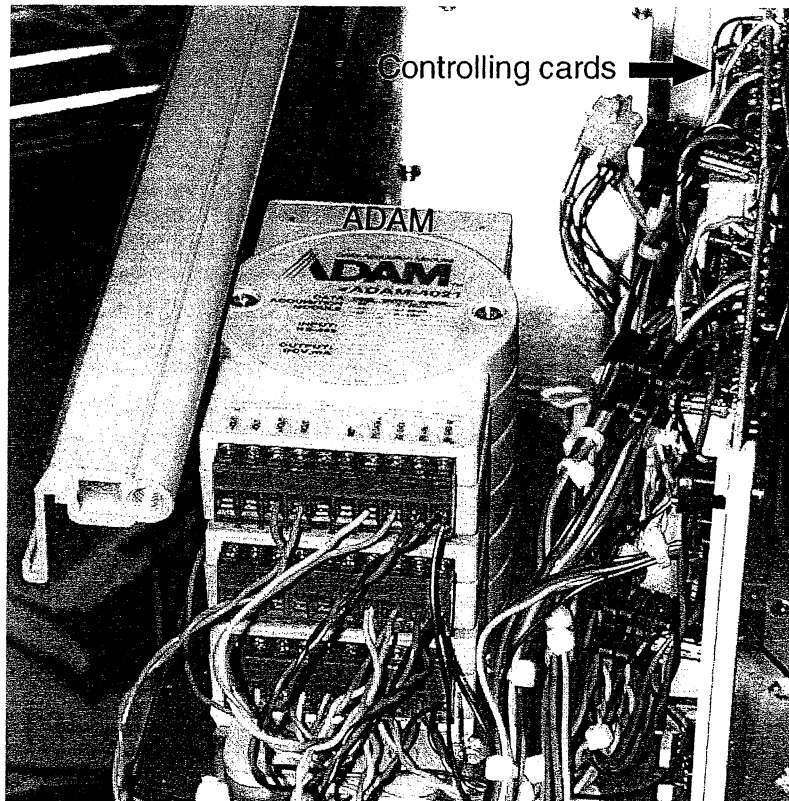
Figure 4.25. The Adam controlling units.

Figure 4.26. The front of the detector.

4.3.4.1 The front of the detector

On the original cooling house (the insulating box that protects the detector and chills it) a clumsy front existed that made the effective length of the detector 50 cm (when a fibre is connected). This length was not appropriate as the box wouldn't be big enough in the end. Another problem was that the shutter was manual and couldn't be operated via a computer. So the goal was to decrease the length of the detector from 50 cm to 40 cm and at the same time install some kind of shutter that could be controlled by the computer. To solve the problem the entire front from the original cooling house was deconstructed. As it turned out most of the front consisted of space to make the lens in the system focus on the *PMT* active surface. The inner part of the old front was used in the new front, although it was modified by the addition of three threaded holes. This part was screwed on to the cooling house. On this part a modified lensholder with a diameter of 2.5 cm was placed via the same three holes. To be able to control the shutter via a computer, a new shutter was constructed. This shutter operates in either an open or shut mode. This shutter was constructed on the side of a U-bracket on the opposite side of a gradient neutral-density filter wheel, see Figure 4.28. The idea with this is to prevent to destroy the detector by an overexposer of light. Here the filter acts as first order security and the shutter is second. If the incoming light is too bright the wheel will turn to a higher attenuation thus letting less light enter the detector. But if the wheel uses its maximum filter and if there is still too much light in the detector, the shutter will close and no light will enter the detector. A picture of the arrangement is presented in Figure 4.28 and Figure 4.29.
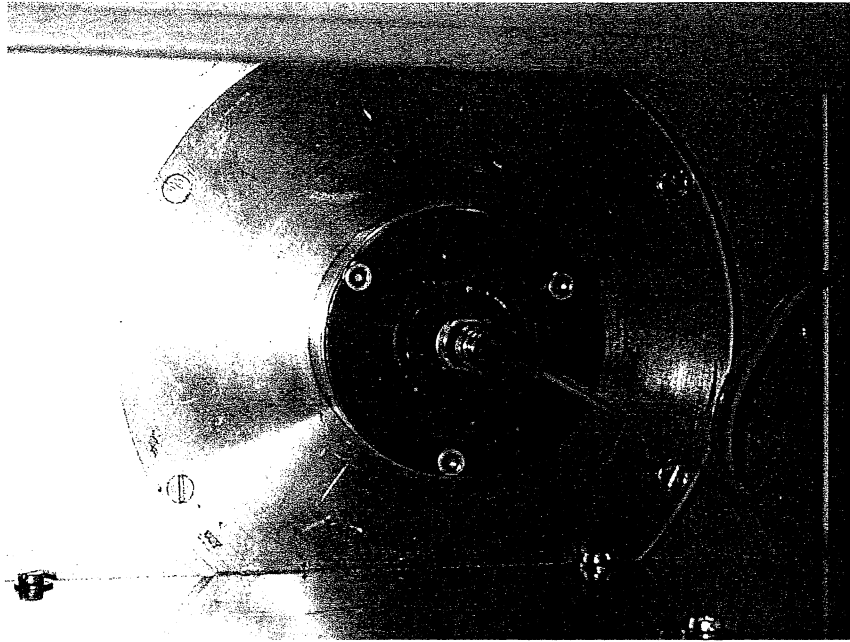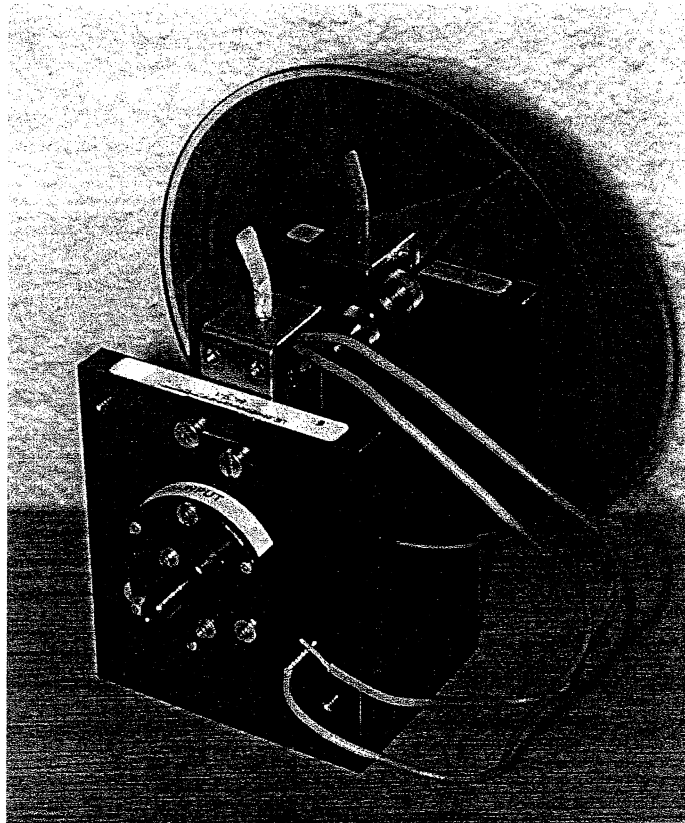
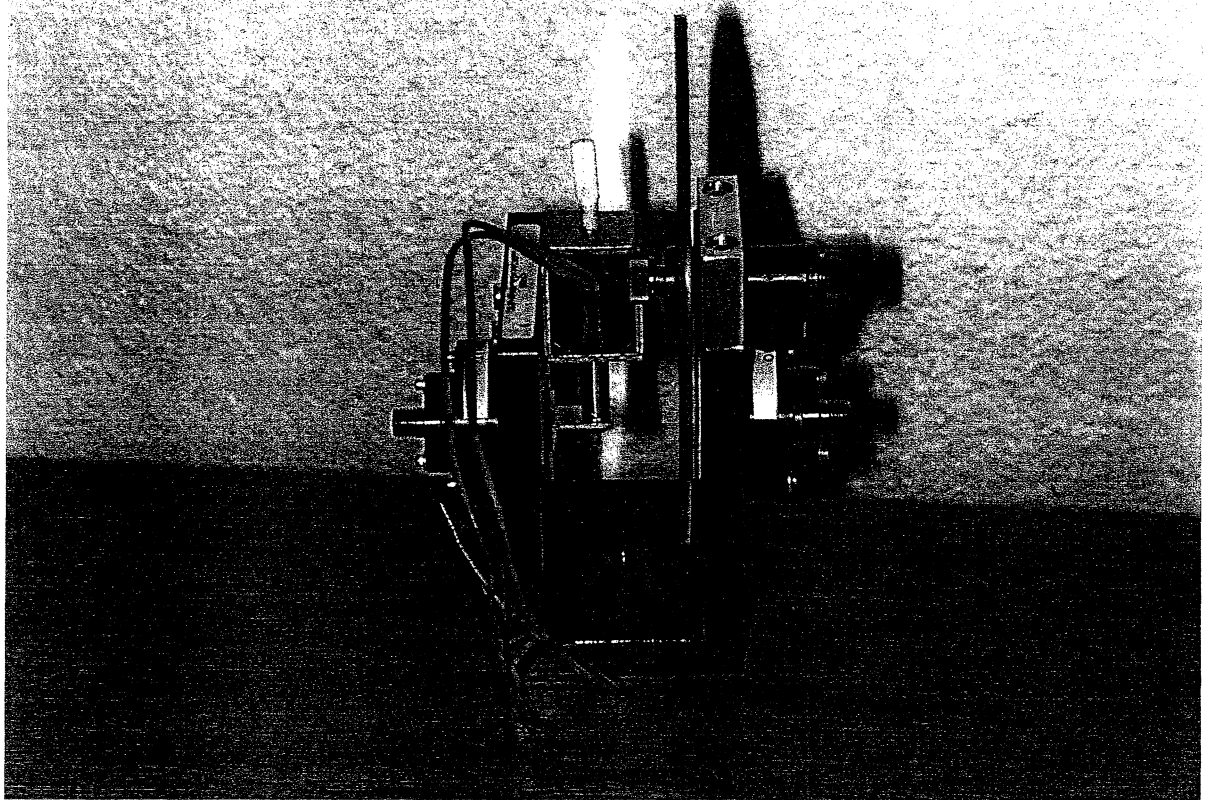Figure 4.27. The front

Figure 4.28. The U-bracket assembly.

Figure 4.29. A side view of the U-bracket arrangement.

To be able to construct a new front a special lens had to be ordered with the specific purpose of focusing on a point right in front of the lens (in this case the light that leaves the fibre) nine and a half centimetres behind it. Some calculations were performed and a lens with focal length of 1.15 centimetres was chosen.

5 Results

5.1 Measurements

All the measurements for the version 1.0 were made during two intense weeks in Milan, Italy. These measurements where performed according to the protocol prepared in a project called Medphot. In this the parameters accuracy, linearity, precision/sensibility, stability and reproducibility are measured. Each of these parameters will be discussed in the following sub-chapters. This version of the instrument also had a unique chance to measure *in vivo*, which means that measurements was performed on living breast tissue. To aid measuring the five different parameters, a special five times five matrix of phantoms was created, with linearly varying scattering and absorption coefficients, that were confirmed by measurement with an integrating sphere. The first element of the matrix is called A1 and the last is called E5. These phantoms are artificial samples that are important for validation of light propagation models and they can also play an important role for calibration[2]. A picture of a phantom is presented in Figure 5.1. All the evaluations made in this thesis are done using a program provided by the Milan group[33].
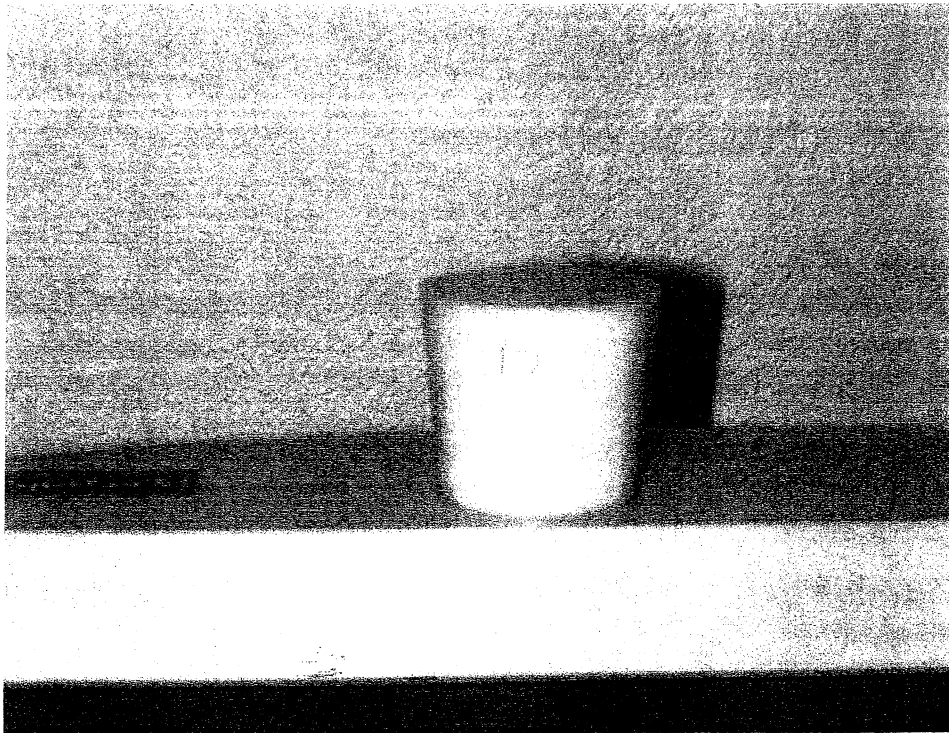
Figure 5.1. A phantom. This phantom is the phantom that imitates breast tissue.

5.1.1 Accuracy

To be able to decide if the system is working properly, the accuracy has to be evaluated. This was performed by measuring the optical proprieties for every phantom in the five by five matrix of phantoms for one inter-fibre distance and one wavelength. In this thesis a 15 mm inter-fibre distance was used for 660 nm. In the Figure below the result is presented with the scattering on the y-axis and the absorption on the x-axis, together with the corresponding values measured from the integrating sphere measurement. In this Figure the results from the Milan-group is also presented.
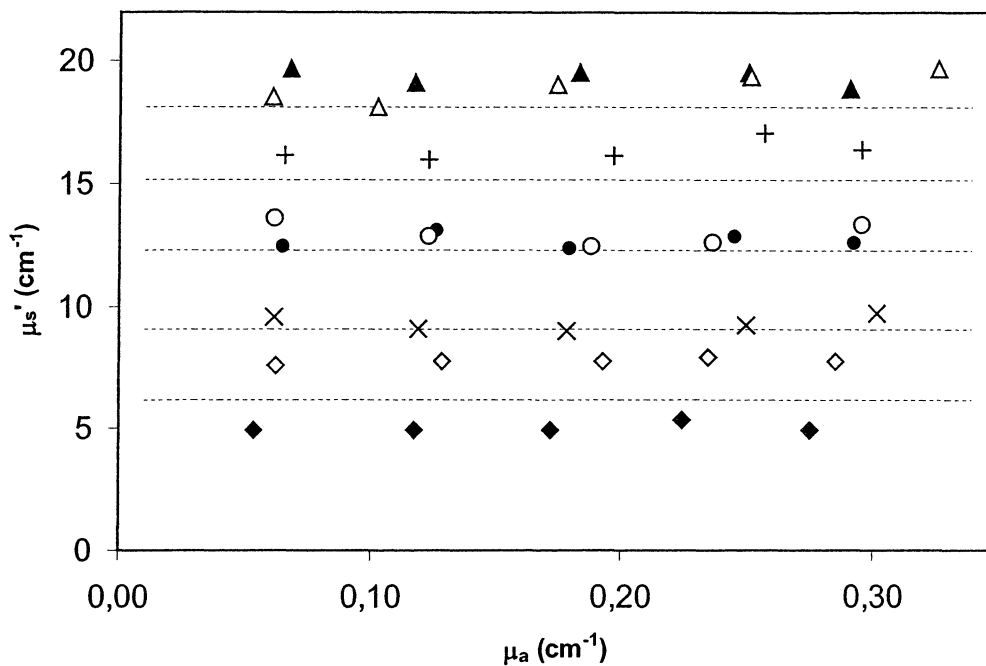
Figure 5.2. μ_a as a function of μ_s'[34]. The dashed lines represent the average values from the integration sphere measurements for rows A-E, which means that the absorption data from the integrating sphere is not shown. The empty symbols are the measurements performed by the Milan group. Note that they did not perform any measurements on B and D.

As one can see the integrating sphere values differ slightly from the time-resolved values, but all in all the accuracy between the two measuring methods is quite similar, especially for the B and C phantoms.

5.1.2 Linearity

This parameter may be thought of as a completion of the accuracy measurement or perhaps an easier version. It is most common to make a comparison with another system using this parameter, since the accuracy measurement and evaluation may tend to be a bit strenuous to perform. In this particular case the linearity is easy to extract from the accuracy results. However, in this presentation the accuracy was used to calculate the linearity. Five different points for each optical property were calculated by taking the average of the data points that

was supposed to be the same, for instant the points in one row of dots in the diagram above are the data points that are supposed to have the same scattering coefficient, see Figure 5.3 and 5.4.
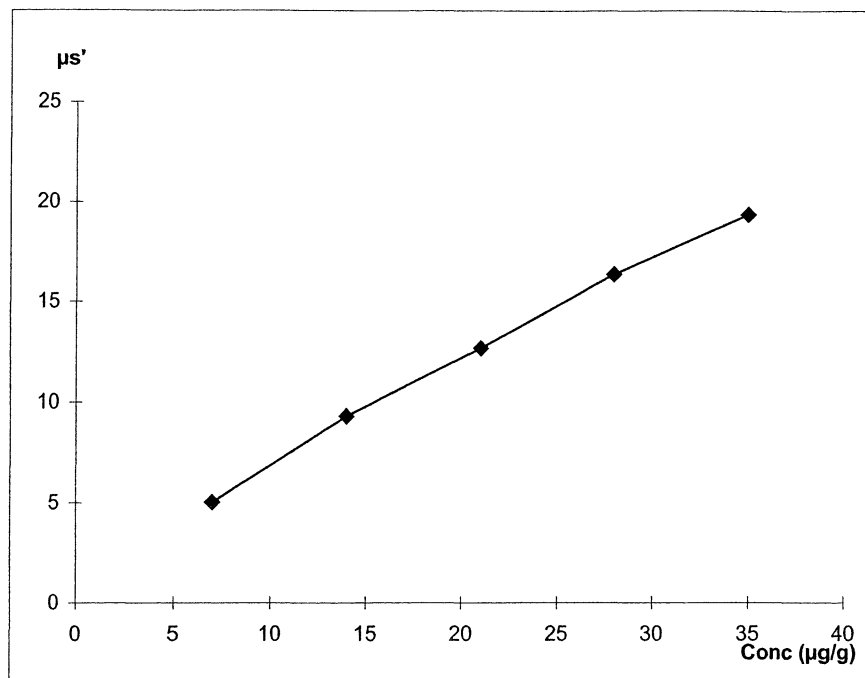

Figure 5.3. μ_s' as a function of concentration of black pigment in the phantoms.
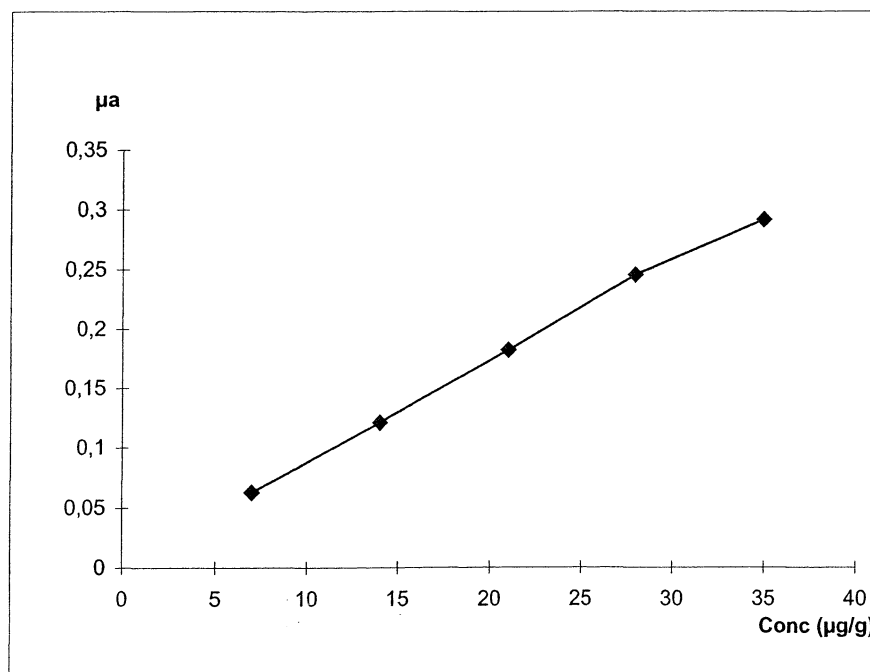

Figure 5.4. μ_a as a function of the concentration of black pigment in the phantoms.

Both of the diagrams correspond to a straight line, which is very appropriate, since the measurements from the integrating sphere also show the same characteristic.

5.1.3 Precision/sensibility

One parameter of particular interest is the sensibility. It will indicate how long one has to measure before the values are good enough to be considered stable. This was the most time consuming parameter to evaluate. First of all 3000 measurements were performed, where each measurement was made during 0,2 seconds, then 8 different time intervals (0.2, 0.4, 0.8, 1.6, 3.2, 6.4, 12.8, 25) were creative using superposition of the retrieved data. This task was not as easy at it may sound, since it required some algorithms that did not exist. The std-files could not be transformed into the dat-format that the evaluation program needed. The 3000 files were to be converted into a major matrix so that different time intervals could be created. The program that came with the spc-card had some bug in it so that the curve sometimes ended up displaced in time and the T_0 (the time where the peak of the curve is at) for the system had an increasing trend in time, which had to be compensated for in order to get valid optical properties. In Figure 5.5 a diagram of how the countrate per second varied with time is presented. This is of major interest; since it is important to know that the countrate will drop the longer the instrument is running.
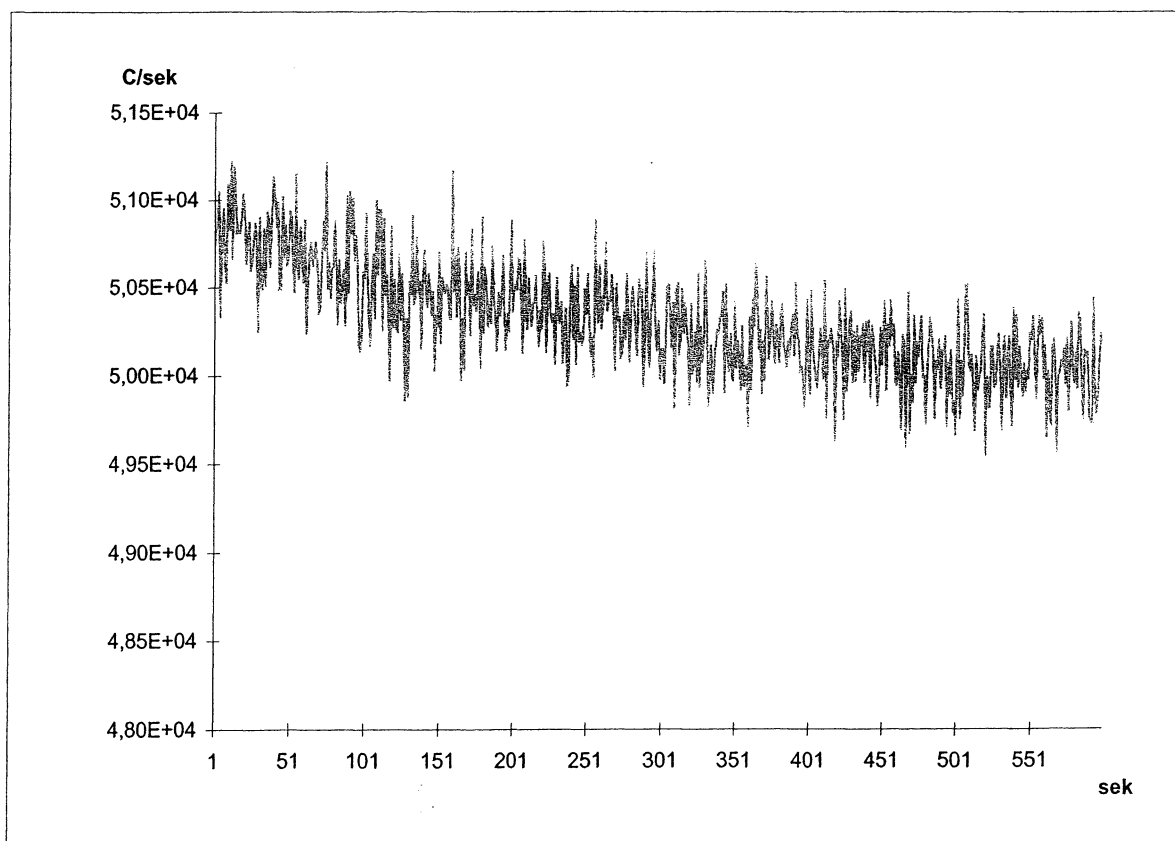

Figure 5.5. Count/sec (C/sec) as a function Time (sec).

If the measurement is to be redone one can always do it for shorter time intervals than 0.2 seconds, preferably 0.001 seconds, which is the lowest possible measuring time, as given

above in the chapter about the SPC-card. In Figure 5.6 and 5.7 the sensibility is presented with a logarithmic scale, for both optical properties, as the standard deviation divided by the mean value and the time.
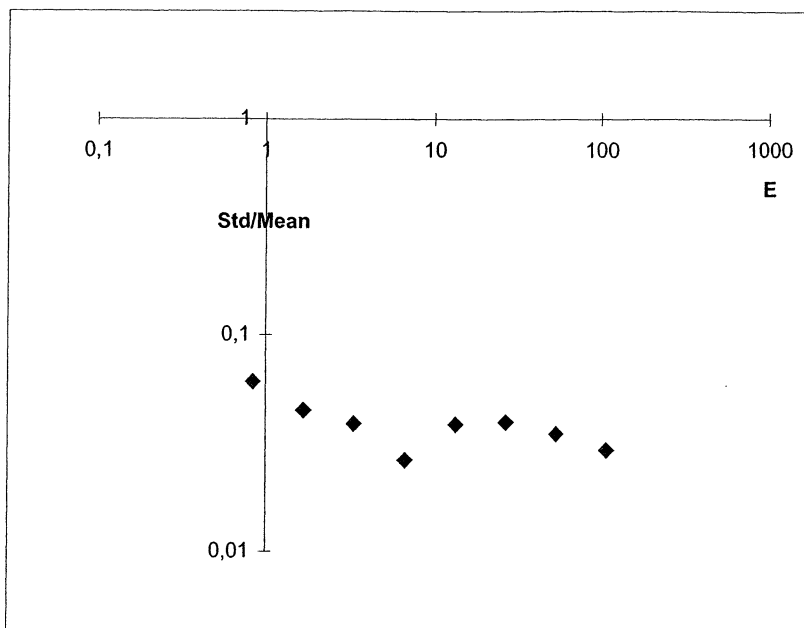

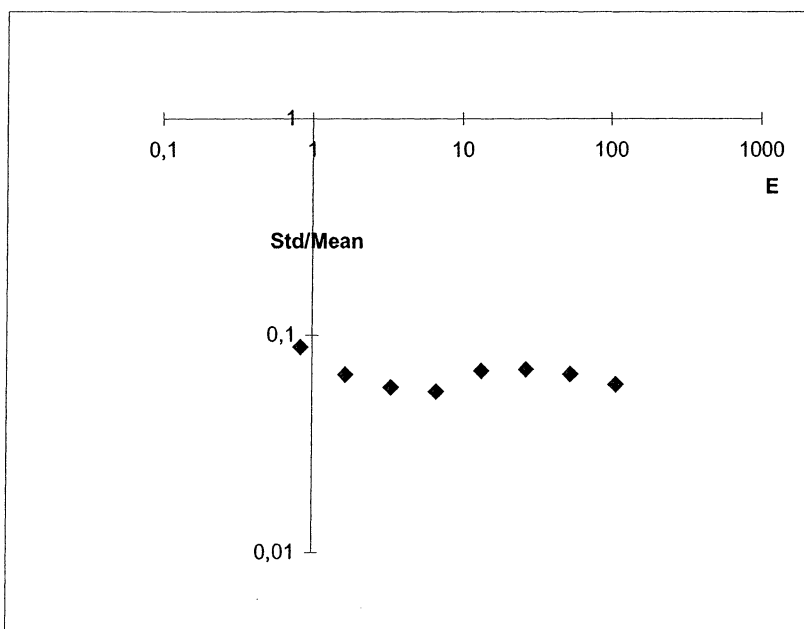Figure 5.6. The sensibility as a function of the energy for μ_a.

Figure 5.7. The sensibility as a function of the energy for μ_s'.

5.1.4 Stability

The curve for one specific phantom was measured during a longer period to see if the optical properties were stable in time. In this measurement the results from the sensibility were used to evaluate how the absorption and the scattering vary in time. The measuring time was set to 1.6 seconds and ten different points were considered. The algorithm made in Matlab randomly selected 12 different points, from 12 specified intervals during the 10 minutes the measurement was made. The most interesting result actually turned up during the sensibility evaluation when the T_0 of all 3000 curves was plotted against time. In the diagram below this plot is presented. The conclusion is that T_0 increases in time, which could be a consequence of varying temperature. This must be taken into consideration when the curve is evaluated. In the table 5.1 below 12 different values of the optical properties are listed.

OptMua	OptMus'
0.0842	10.85
0.0854	11.14
0.0854	11.12
0.0863	11.58
0.0859	11.59
0.0854	11.47
0.0872	11.89
0.0887	12
0.0912	12.55
0.0879	12.29
0.0879	12.44
0.0914	12.97

Table 5.1. Stability values

What is of major interest in the table is to see how the properties have tended to increase in time, even though the increment is not that large. This result could be examined together with the results gained in Figure 5.5. A fast cross-examination shows that when time goes on, the optical properties tend to increase, while the countrate decreases.

5.1.5 Reproducibility

To see if the system is stable enough from day to day, the parameter reproducibility comes in handy. Every day the curve for one specific phantom (C1) was measured to see how much the optical properties vary. This is of specific interest when the reliability of the machine is considered, see table 5.2.

Date	OptMus	OptMua
10 Okt	0,0575	11,14
30 Okt	0,0526	10,41
31 Okt	0,0583	11,41
Std:	0,003086	0,517333

Mean:	0,056133	10,98667
%:	0,054976	0,047087

Table 5.2. The reproducibility of the system.

As one can see in the table only three parameters has been evaluated, since some of the measurements in Milan were not reliable. However, the system is quite stabile from one day to another, but further measurements must be performed in order to make sure that the measurements are reproducible.

5.1.6 *In vivo* measurement

Four different women (ages 26, 28, 39 and 50) were kind enough to volunteer to be measured. Five different points on the breast were measured with two wavelengths and three inter fibre distances (10 mm, 15 mm and 20 mm). In picture 5.8 a sketch shows where the measurements were performed.
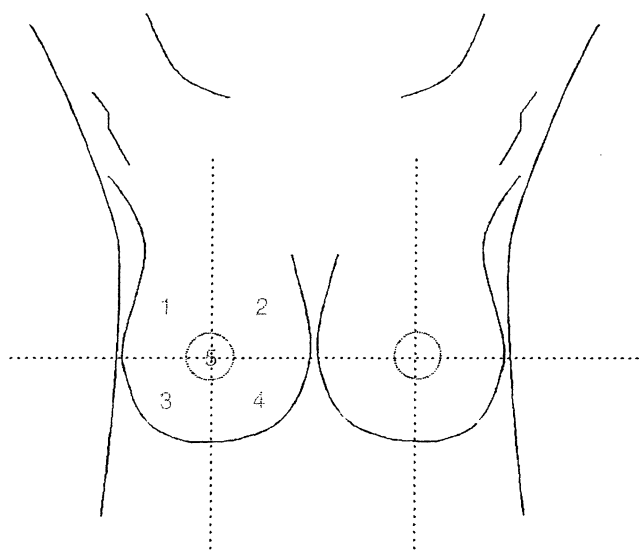
Figure 5.8. A sketch of where the measurements were performed on the breast (taken from the Optimamm protocol).

One of the volunteers returned a week later and the measurements were performed again, this time with the addition of a measurement on a small matrix in region 1. This last measurement was mainly performed to see how the optical properties differ over a small region in one part of the breast. Analysing this part of the breast is very interesting and important since it is the most common part of the breast that develops cancer. The optical properties will differ from person to person and with time on one person. During further studies one can see that this is because of all the water that gathers in the body during menstruation, which makes a comparison in time interesting. The laboratory that was visited in Milan performed the very same measurements and could via a more complex method decide even more successfully which of the volunteers had the most lipid (fat) in their breasts. In Figure 5.9-5.12 all data acquired during the *in vivo* measurement is presented. The distance *d* is the inter-fibre distance. In Figure 5.13 is a diagram the matrix in region 1.
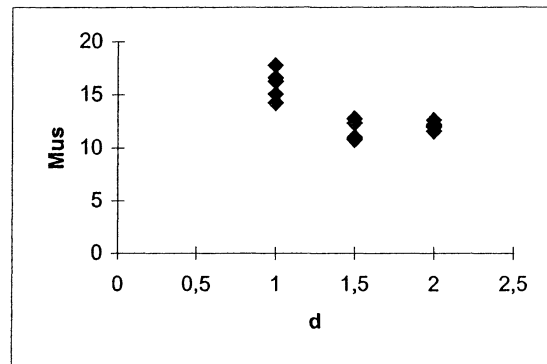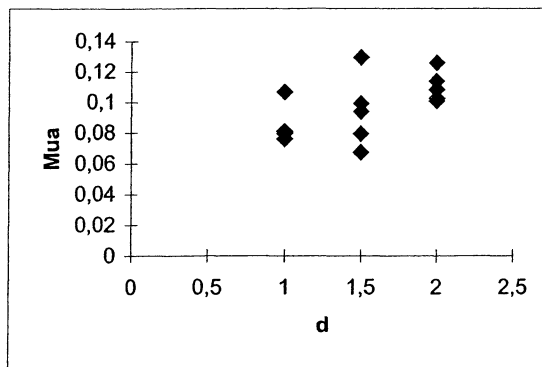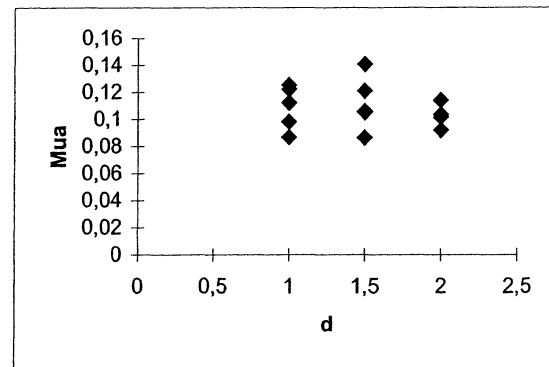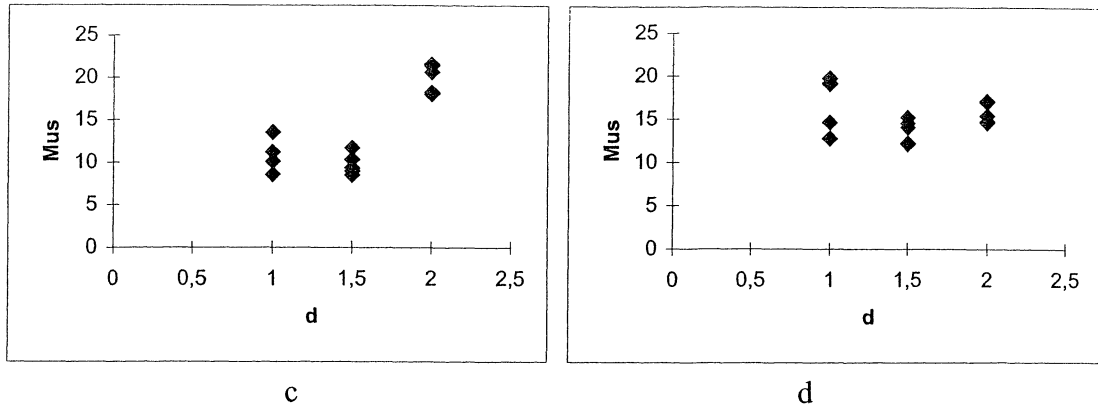
a

b
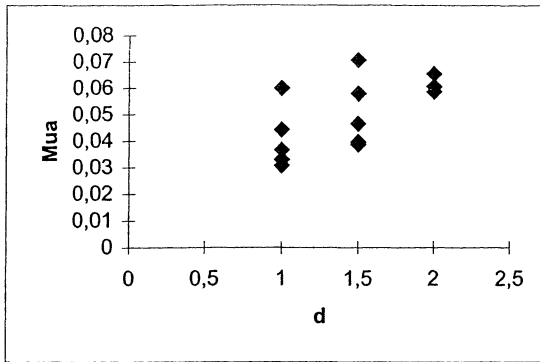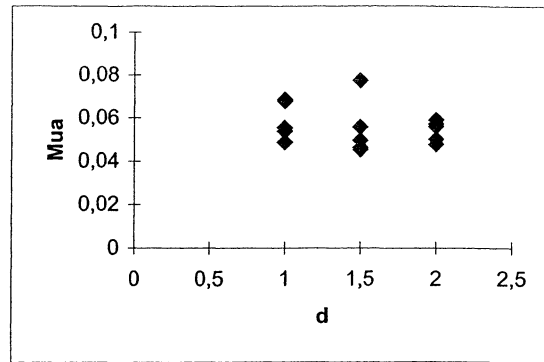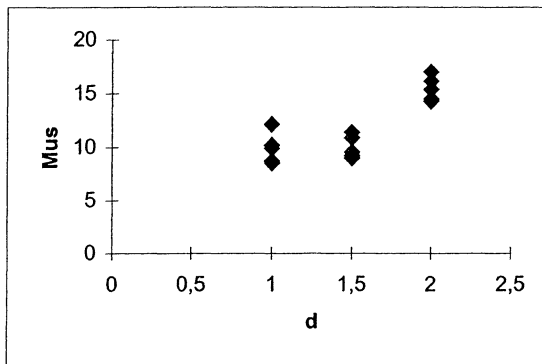
Figure 5.9. The results for the 26 year old woman. (a) μ_a versus d at 660 nm. (b) μ_a versus d at 785 nm. (c) μ_s' versus d at 660 nm. (d) μ_s' versus d at 785 nm.

c

d

a

b

c   d

Figure 5.10. The results for the 28 year old woman. (a) μ_a versus d at 660 nm. (b) μ_a versus d at 785 nm. (c) μ_s' versus d at 660 nm. (d) μ_s' versus d at 785 nm.

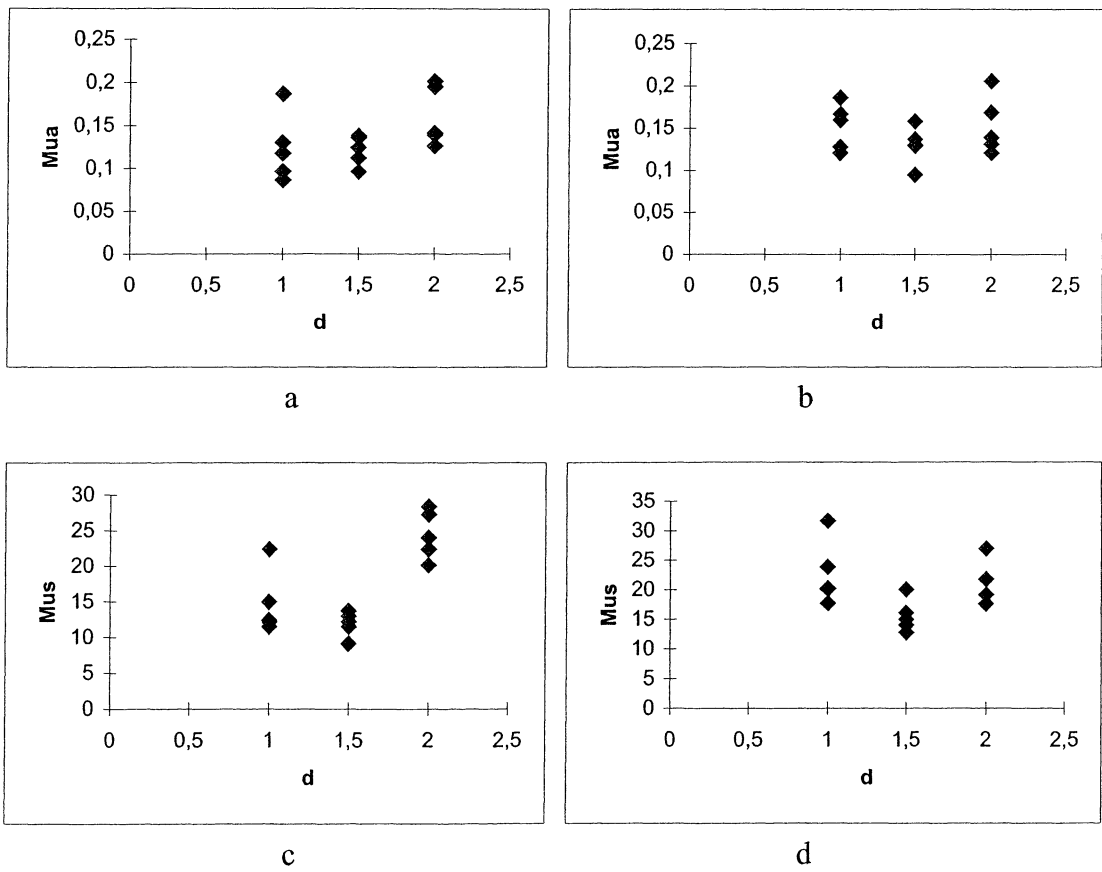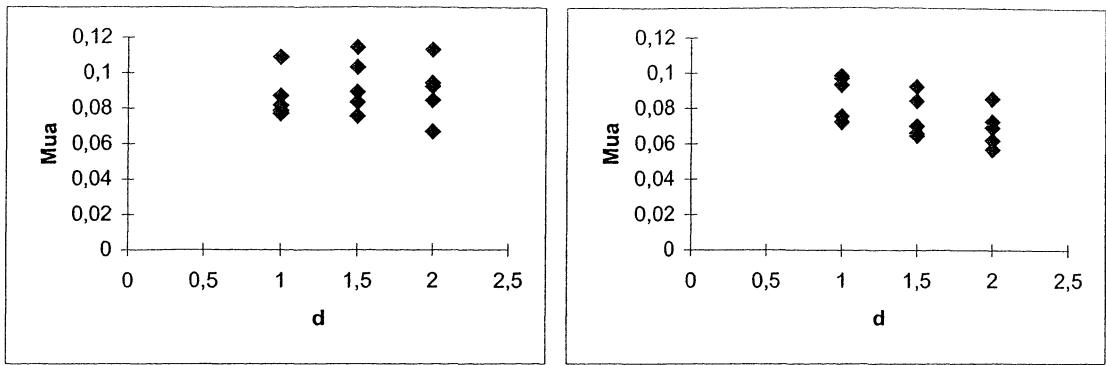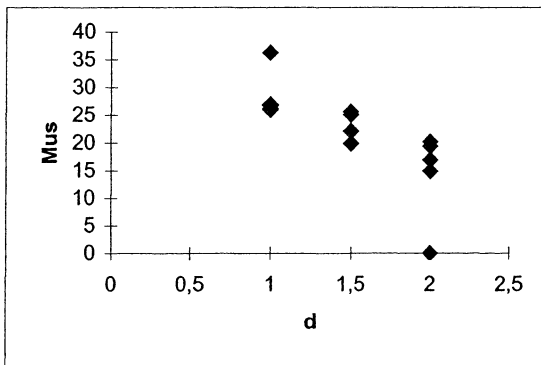a   b

c   d

Figure 5.11. The results for the 39 year old woman. (a) μ_a versus d at 660 nm. (b) μ_a versus d at 785 nm. (c) μ_s' versus d at 660 nm. (d) μ_s' versus d at 785 nm.
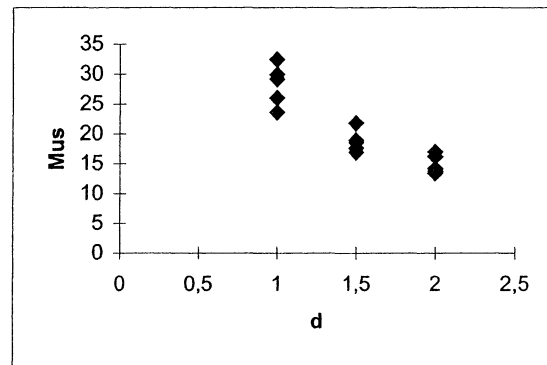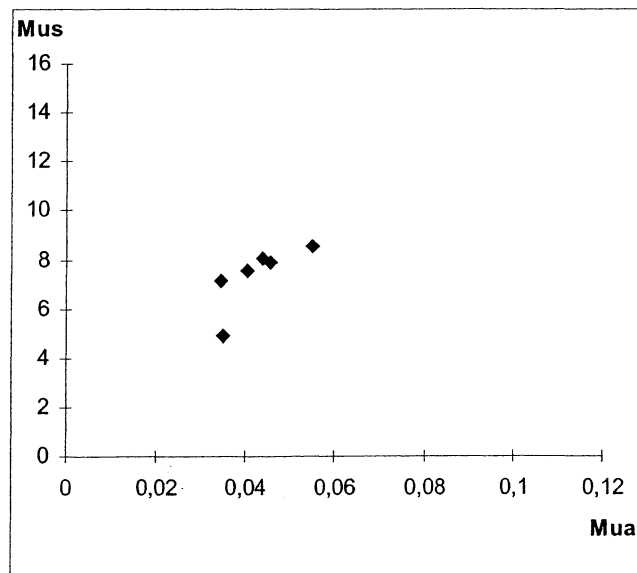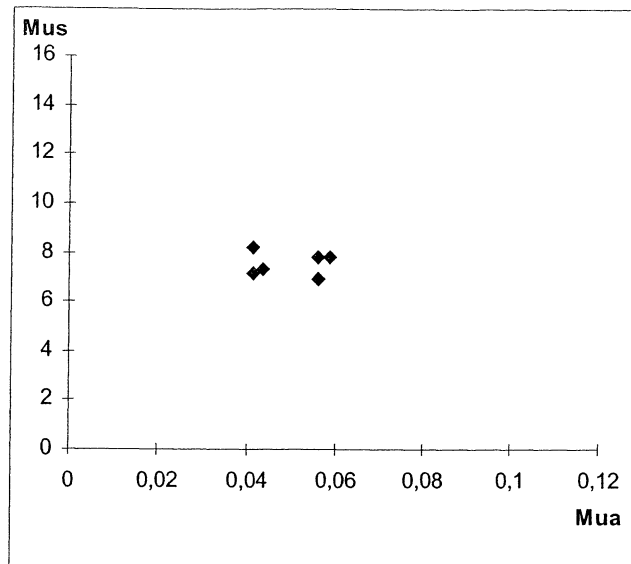
Figure 5.12. The results for the 50 year old woman. (a) μ_a versus d at 660 nm. (b) μ_a versus d at 785 nm. (c) μ_s' versus d at 660 nm. (d) μ_s' versus d at 785 nm.
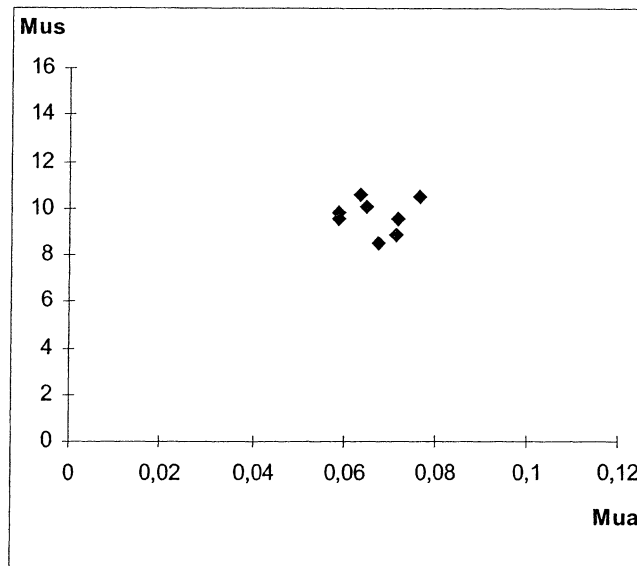

a

b

c

Figure 5.13. The accuracy of the *in vivo* matrix. (a) 1 cm inter-fibre distance. (b) 1,5 cm inter-fibre distance. (c) 2 cm inter-fibre distance.

5.1.6.1 Conclusion of *In vivo* measurments

These measurements did not give much information about the breasts. However, much of the evaluation in Figure 5.13.a-c gave some information about the homogeneity of breast tissue. The wider the inter-fibre distance gets, the deeper in the tissue one measures, which gives information about the tissue in different layers. Unfortunately the measurements were performed with only two wavelengths, when more relevant information about the breast tissue could have been extracted if all four wavelengths had been used. The Milan group, however, was able to give more information about the tissue. The values obtained with the system

corresponds relatively well the values according to Welch and Van Gemert[5]. However it would be of major interest to perform measurements on malignant tumours as a comparison with this system, so one can see the difference in optical properties.

6 Discussion and conclusion

In conclusion the constructing of the instrument was completed before the time limit originally set for the project. However that was possible because we worked under heavy pressure during most of the time, since it needed to be completed as soon as possible so that other Master's students could use it. One major problem that was discovered during the project, was that the program that came with the spc-card or sometimes the spc-card itself, moves the curve in time without any real reason. This affects the evaluation, especially sensibility, in a way that makes the fit-routine an unstable. Of major interest is also thestudy of the countrate for time longer than 10 minutes. Measurements must be performed so that it is clear when and if the instrument finds a stable countrate. It may also be interesting to examine how the countrate per second varies with the optical properties, as discussed in section 5.1.4. This problem is the main reason to why the special programming was needed when the sensibility was evaluated. It is recommended that tests are performed to evaluate whether it is the program or the spc-card that is causing this. Since there will be a new detector in the system, it is recommended that all the Medphot measurements are repeated, in order to make sure that the performance of the new instrument is stable. Another test that should be performed is just letting the machine run for a very long time, to see if the cooling system is good enough. If it turns out that the fan doesn't work as well as it should, a second fan should be put inside the box, next to the radiator.

7 Acknowledgements

First of all we would like to thank our two supervisors Johannes "Jojje" Swartling and Stefan "Stiffo" Andersson-Engels for their help throughout the project and for the great time we spent with them in Milan.
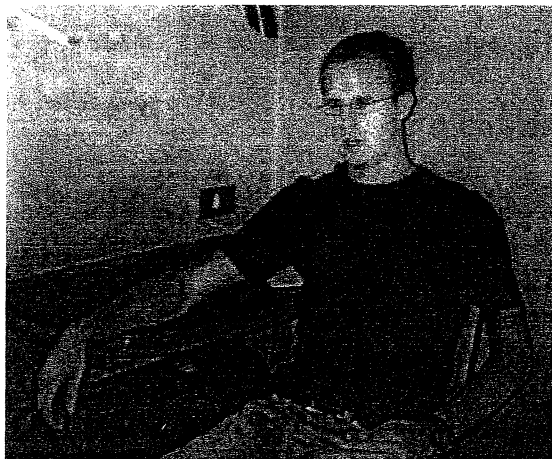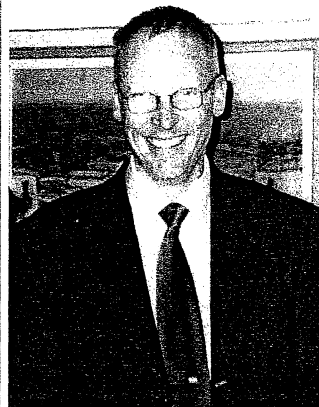
Jojje   Stiffo

Åke Bergquist and his partner in crime Bertil Hermansson also deserves a spot in the light, since they always had time for all our stupid questions and requests. Thank you for a great time, boys.

Åke   Bertil

Antonio "Piffo" Pifferi and his group at Politecnico in Milan for the great stay we had during our two-week trip.

Piffo, Eleonora and Andréa from the Milan group.

Mr Rinaldo Cubeddu at Politecnico for letting us use the *fit*-program. Also that we could use his office as a meeting room during the Milan campaign, even though we never met him.

The poor guy that was hired to take care of security at Politecnico, who had to sit in the cold lobby the entire day and do absolutely nothing.

Margaret Malmström for helping us with our English and for having the stamina to point out all the "off":s that was supposed to be "of" and all the "trough":s that was supposed to be "through".

Karin Kolmert for enduring all our curses during the entire time we shared room with her, without ever complaining. Also for being our number one supporter, when it comes to successfully complete the machine as fast as possible.

Filippo "Pippo" Inzaghi for scoring three goals in a single game at San Siro on October the 6:th. You gave us the spirit to carry on.

Filippo

Too our families and our girlfriends for not being too angry with us when we haven't had time to associate with them. Also for caring about us and constantly reminding us that one needs to sleep, eat and rest in order to do a good job.

To the many people we corresponded with during the project, who helped us with different parts of the machine. Among others we would like to acknowledge Wolfgang Becker (Becker & Hickl), Ersoy Urgyr (Oz optics) and Henrik Sivert (Hamamatsu).

8 References

1. Socialstyrelsen, Hälsoundersökning med mammografi, http://www.sos.se/FULLTEXT/9803-017/9803-017.htm, January 2003

2. J. Swartling, "Biomedical and atmospheric applications of optical spectroscopy in scattering media", Doctoral Thesis, Department of Physics, Lund Institute of Technology December 2002, Lund Reports of Atomic Physics LRAP-290.

3. S. Epstein, "The breast cancer prevention program", October 1997

4. R. Cubeddu, A. Pifferi, P. Taroni, A. Torricelli, and G. Valentini, "Noninvasive absorption and scattering spectroscopy of bulk and diffusive media: An application to the optical characterization of human breast", February 1999.

5. A. J. Welch and M. J. C. van Gemert, eds., "Optical-thermal response of laser-irradiated tissue", Plenum Press, New York, NY, 1995.

6. S Svanberg, "Atomic and molecular spectroscopy, Basic aspects and practical applications", Springer 2001.

7. P. A. Cadby, E. Dimitriadis, I. J. Forbes, "In Porphyrin Photosensitation", 1983

8. F. A. Duck, "Physical Properties of Tissue", Academic Press Ltd., London, 1990.

9. G. M. Hale and M. R. Querry, "Optical constants of water in the 200 nm to 200 microm wavelength region", Appl. Opt. 12, 555-563, (1973).

10. S. A. Prahl, "Tabulated molar extinction coefficient for hemoglobin in water", http://omlc.ogi.edu/spectra/hemoglobin/summary.html, (2002-12-22).

11. H. Q. Woodard and D. R. White, "The composition of body tissues", Br. J. Radiol. 59. 1209-1218 (1986)

12. C. Eker, "Optical characterization of tissue for medical diagnostics", Doctoral Thesis, Department of Physics, Lund Institute of Technology October 1999, Lund Reports of Atomic Physics LRAP-249.

13. S.L Jacques and D.J. McAuliffe, "The melanosome: Threshold temperature for explosive vaporisation and internal absorption coefficient during pulsed laser irradiation, *Photochem. Photobiol.* 53, 769-775", 1991

14. L. G. Henyey and J. L. Greensteine, "Diffuse radiation in the galaxy", Astrophys. J 93, 70-83 (1941.)

15. C. af Klinteberg, "On the use of light for characterization and treatment of malignant tumours", Doctoral Thesis, Department of Physics, Lund Institute of Technology April 1999, Lund Reports of Atomic Physics LRAP-245.

16. R. Berg, "Laser-based cancer diagnostics and therapy - Tissue optics considerations", Doctoral Thesis, Department of Physics, Lund Institute of Technology 1995, Lund Reports of Atomic Physics LRAP-184.

17. G. Sparr and A. Sparr, "Kontinuerliga system", Studentlitteratur 2000.

18. T. H. Pham, R. Hornung, M. W. Berns, Y. Tadir, B. J. Tromberg, "Monitoring Tumor Response During Photodynamic Therapy Using Nearinfrared Photon-migration Spectroscopy", February 2003

19. R. Cubeddu, A.Pifferi, P. Taroni, A. Torricelli, and G. Valentini, "Experimental test of theoretical models for time-resolved reflectance", Med Phys. 23, 1996

20. M. S. Patterson, J. D. Moulton, B.C. Wilson, K. W. Berndt, and J. R. Lakowicz, "Frequency-domain reflectance for the determination of the scattering and absorption properties of tissue", 1991

21. S. Andersson-Engels, R. Berg, O. Jarlman, and S. Svanberg, "Time-resolved transillumination for medical diagnostics", 1990

22. http://kurslab-fysik.lth.se/FEOptisktek/detector1_2001.pdf, January 2003

23. http://usa.hamamatsu.com/hcpdf/R3809u-50series.pdf, January 2003

24. H. Hogan, "Advances Boost Photon Detection", Biophotonics international July/August 2002

25. http://www.chembio.uoguelph.ca/educmat/chm386/rudiment/tourexp/heatcap.htm, January 2003

26. http://www.plmsc.psu.edu/~www/matsc597c-1997/systems/Lecture4/node4.html, January 2003

27. http://www.biophotonen-online.de/abstract/abs2000-22.htm, January 2003

28. Becker & Hickl GmbH, "Time-Correlated Single Photon Counting Modules", Users manual, November 2000

29. Sven-Göran Pettersson, Stig Borgström, Hans Hertz, "Optisk Teknik", 1999

30. http://kurslab-fysik.lth.se/FEOptisktek/Fibres_2001.pdf, January 2003

31. http://www.psplc.com/downloads/acrobat/picoquant/pqsepia.pdf, January 2003

32. "ELFA-catalogue 51", Users manual 2003

33. R.Cubeddu, A.Pifferi, P.Taroni, A.Torricelli and G.Valentini, "Experimental test of theoretical models for time-resolved reflectance", 1996.

34. J. Swartling, A. Pifferi, E. Giambattistelli, E. Chikoidze, A. Torricelli, P. Taroni, M. Andersson, A. Nilsson, S. Andersson-Engels, "Measurements of absorption and scattering properties using time-resolved diffuse spectroscopy – instrument characterization and impact of hetrogeneity in breast tissue", Manuscript in preparation. January 2003.

9 Glossary

ADAM – The computer-controlling units.

Chromophores – A molecule that absorbes a photon in the visible region.

Female connector – The part of a connection that gets plugged.

Frequency-modulated method – Alternative method to Time-Resolved Measurements used on the other side of the Atlantic.

In vitro – When tissue measurements are performed *in vitro* they are performed on a sample of the tissue.

In vivo – When tissue measurements are performed *in vivo* they are performed on tissue that is alive in its natural enviroment.

Labview – Programming language that is almost impossible to use.

Mammography – Today the most used method to search for detecting cancer in breast tissue.

Matlab – Programming language that is more likeable than Labview.

Milan – Big Italian city.

Monte Carlo method – Simulation technique that is based on "Throwing the dice".

Optimamm – A collaboration between nine groups around Europe with the goal to find a method to detect breast cancer using non-ionizing radiation. For more information about the project, please visit: http://www.berlin.ptb.de/wdbctx/optimamm/OPTIMAMM.home

Optical mammography – The method of scanning the breast for cancer using non-ionizing radiation.

Optical Window – Wavelength region where tissue is "transparent".

Patent solutions – Most of the solutions in the machine.

PDT – Photo Dynamic Therapy. Optical method to remove cancer tumours.

Peltier element – An element that get hot on one side and cold on the other side when a current is sent through it.

Phantom – Artificial samples that imitates the optical properties of tissue. They can play an important role in calibrating machines.

PMT – Photomultiplier Tube.

TAC – Time to Amplitude Converter. Part of the TCSPCM that converts the time to an amplitude that can be interpretated by the memory.

TCSPCM – Time-Correlated Single Photon Counting Module. The card used to gain the TPSF.

TPSF – Temporal Point-Spread Function. The function gained through a Time-Resolved measurement.

TTL signal – Transistor-Transistor Logic. Logical levels of voltage. The binary bit 0 corresponds to 0 V and the binary bit 1 corresponds to 5 V.
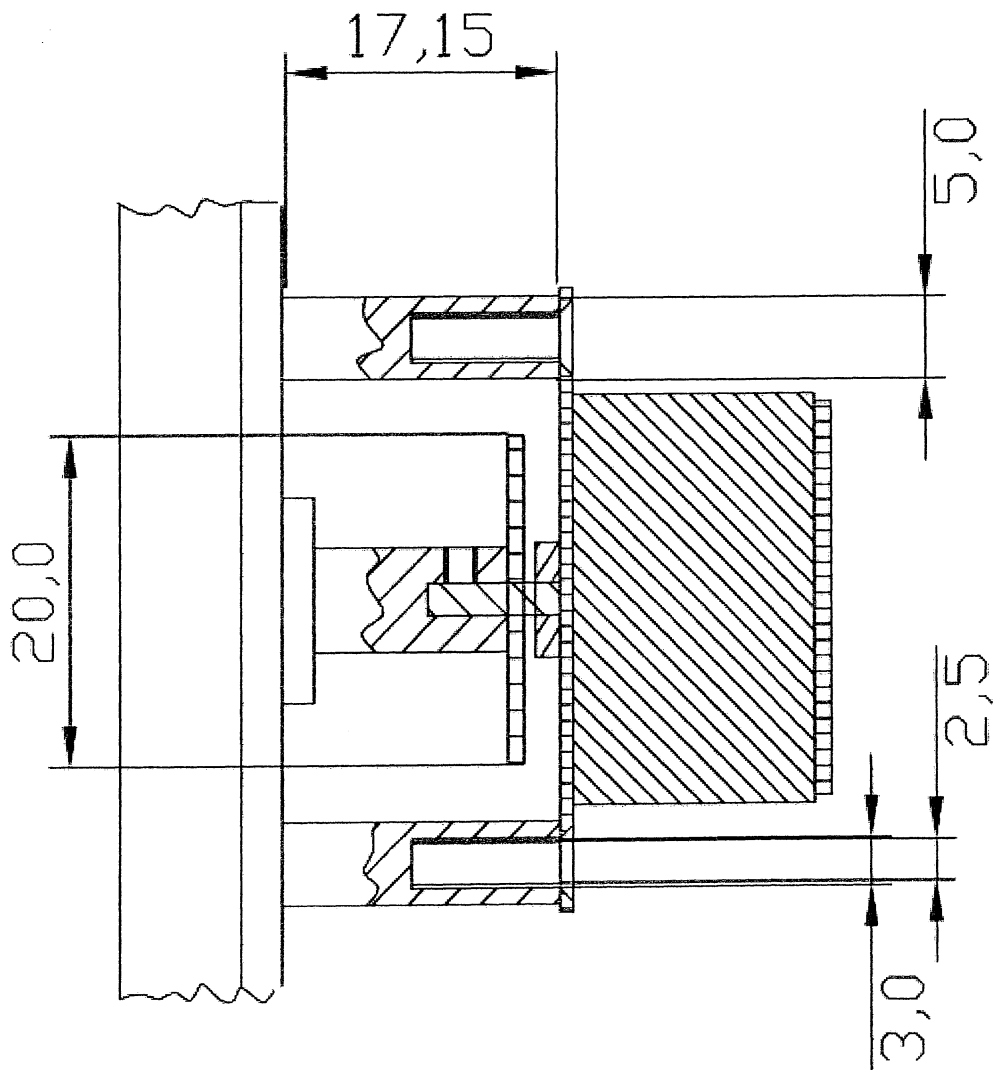
VAC – 230 VAC is what one finds in a socket in the wall, 230 voltage of alternating current.
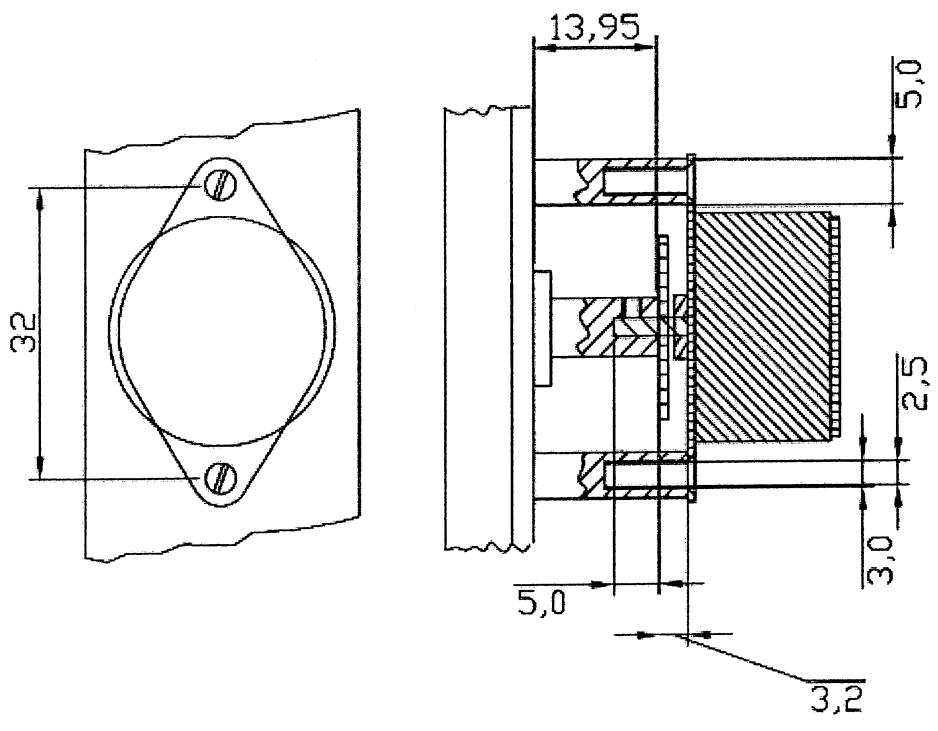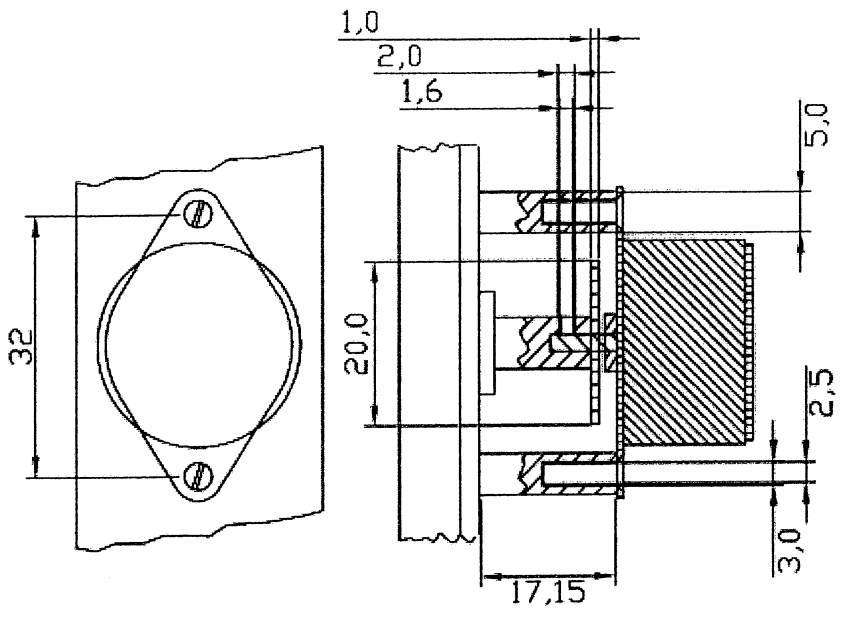
10 Index

Appendices

A Diagram of step motor assembling

1,0
2,0
1,6
5,0
32
20,0
2,5
3,0
17,15

13,95
5,0
32
2,5
3,0
5,0
3,2

2

B An electrical scheme of controller driver to the stepping motors
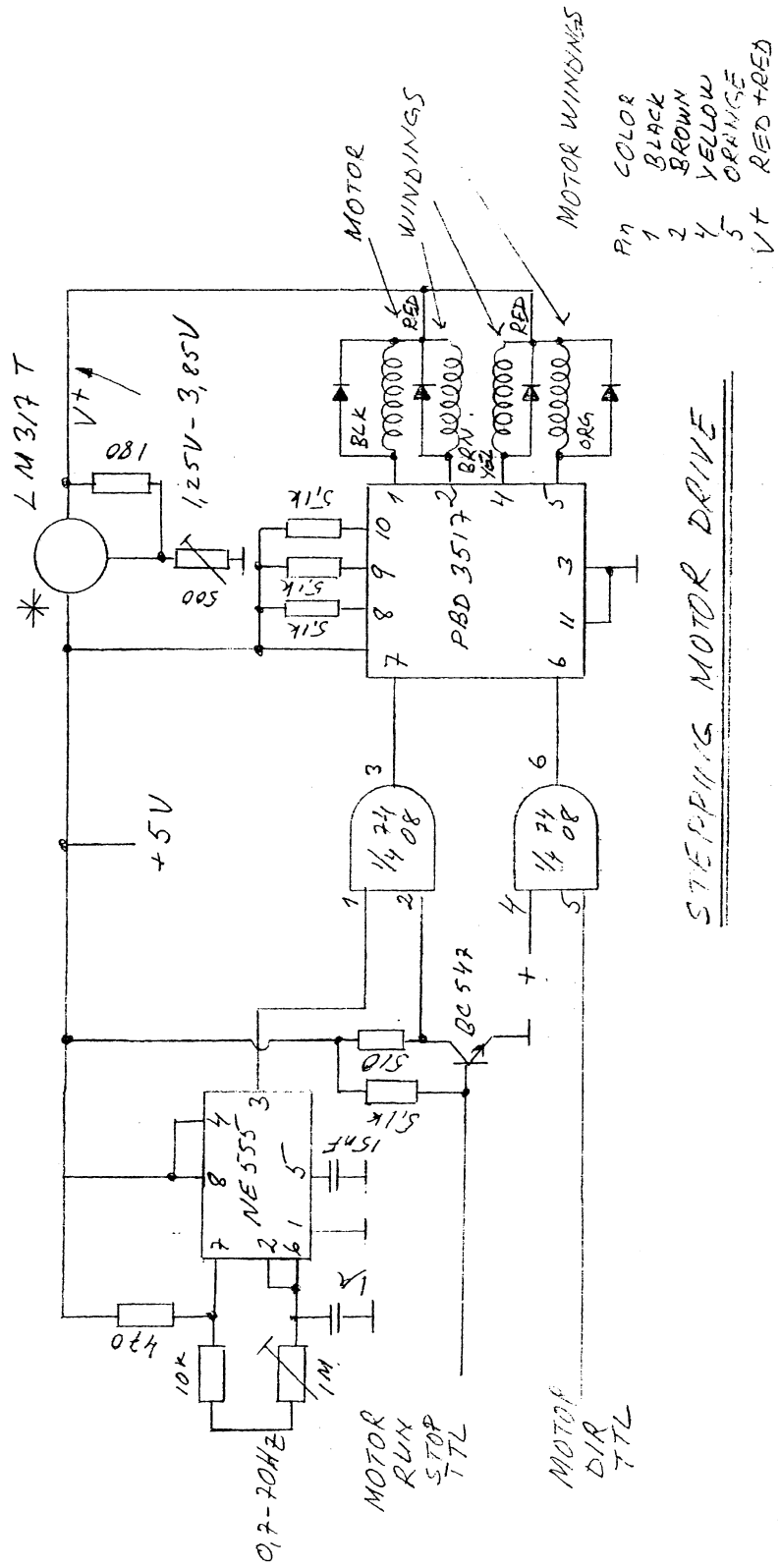
C Adam User's guide

This is a brief introduction regarding how to set-up the Adam system and how to hook-up to a computer. It includes:

❑ Preparing RS-485 interface
❑ Communication Wiring of ADAM-4K
❑ Configuring the ADAM-4K

C.1 Preparing RS-485 interface

This standard is based on data exchange between two communicating devices. If more than two are required several units can be connected together and share a common line. The RS-485 standard allows data rate up to about 10 MBit/s [], and the standard presents many features similar to bus systems. In the RS-485 model several units are connected via twisted pair, balanced electrical cable. The units can be transmitter, receiver or both combined. The cables have two terminating resistors of at least 60 Ω each at both ends. See Figure c1.
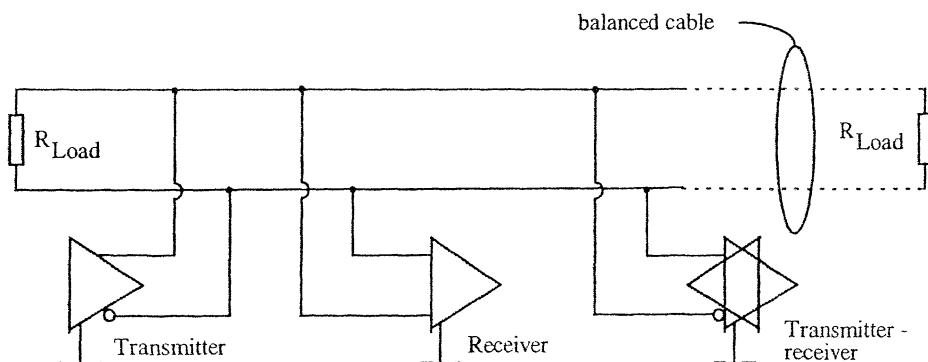
Figure c1.

There is no RS-485 interface in PC. This can be arranged by connecting the Adam-4250 adapter to the serial port on the PC, acting as a 232/485 converter or to connect a CPU card with on-board RS-485 port to one of the PC's buses (PCI, ISA or EISA).

C.2 Adam-4250 wiring

Using Adam-4250, you will need:

1) Adam-4250
2) Direct-through cable
3) DC power supply
4) Twisted pair cable
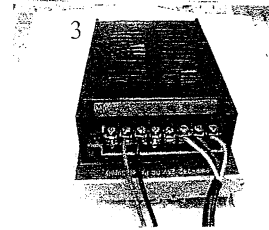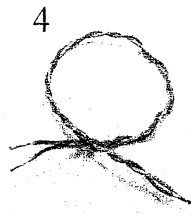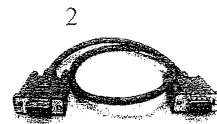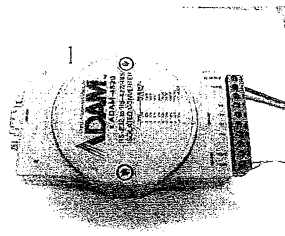
C.3 Adam-4250 Dip switch

Open the shell of ADAM-4520. You will find two dip-switches:
1) SW1, used to set the data bit of serial communication,
2) SW2, used to set the baud rate on both 232 and 485 sides.
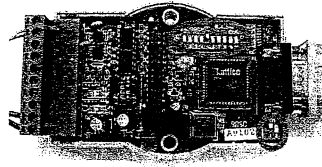
C.4 Communication-Wiring

As described above the units are connected by a twisted cable in a daisy chain.

Daisy Chain
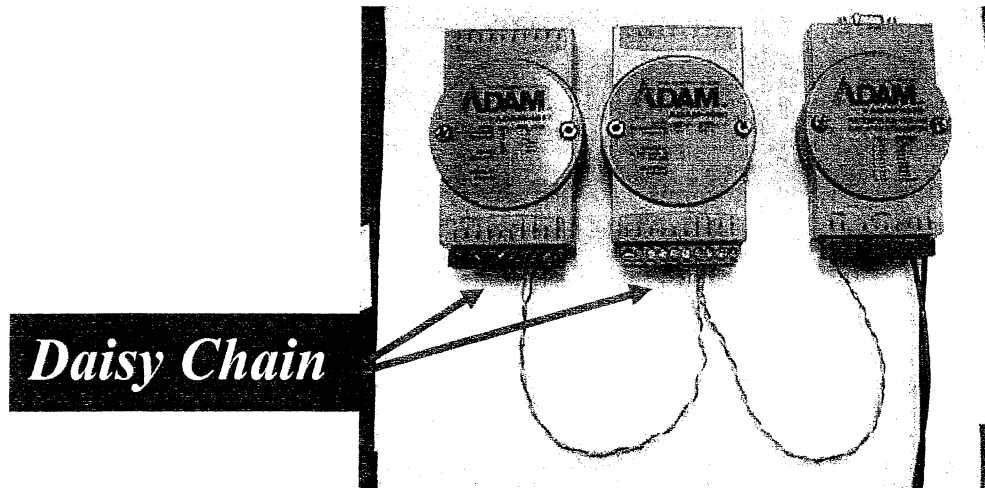
Terminal resistance
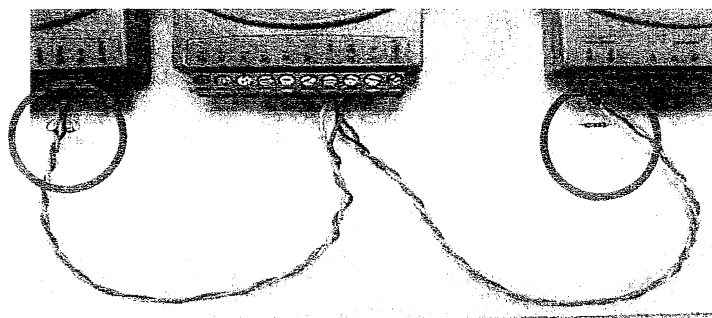
Configure the Com port property on the first page

C.5 Configuring the ADAM modules

On this note software has to be installed in Windows® for proper configuration. Special care is required if the module is to be used in Labview®, when the configuration is done. Do not forget to save to file with file name.reg. Then double click on the file to load it into Windows register. For the configuration do as follows:

    I. Start program ADAM utility
   II. Select com port
  III. Configure the Com port property from the first page
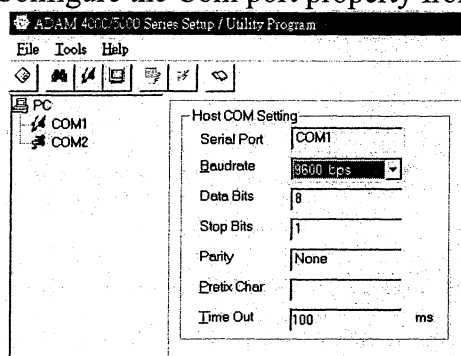
The buttons on the menu bar
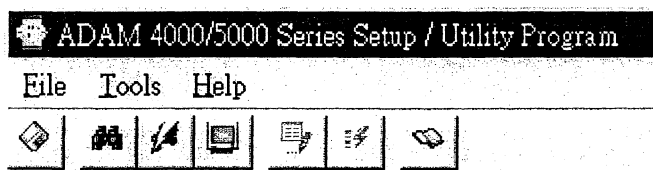
    Press it to search the ADAM modules on 485 networks

    Terminal, issue commands to the modula manually

    Data scope, used to monitor the data on the network form COM port

   IV. Set the Com port's baud rate the same as the Adam's
    V. If the baud rate of the modules is not found, connect the 'INIT*' pin to GND and reset the module. This will force the module into initial mode and the baud become 9600.
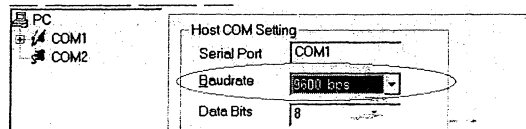
   VI. Once the module is found, there will be a Plus sign shown beside the COM port.
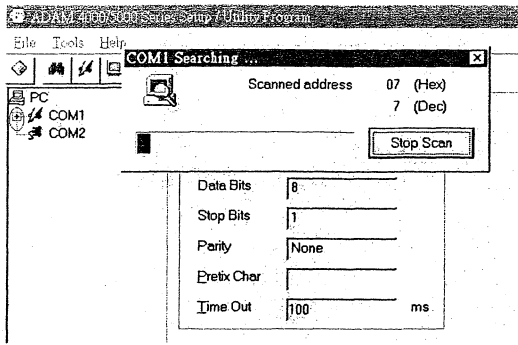
VII. After the scan there will be a module list under the COM port.

VIII. Save to file

Paper

Measurements of absorption and scattering properties using time-resolved diffuse spectroscopy – instrument characterization and impact of heterogeneity in breast tissue

Johannes Swartling[1], Antonio Pifferi[2], Eleonora Giambattistelli[2], Ekaterine Chikoidze[2], Alessandro Torricelli[2], Paola Taroni[2], Magnus Andersson[1], Anders Nilsson[1], Stefan Andersson-Engels[1]

[1]Department of Physics, Lund Institute of Technology, P.O. Box 118, SE-221 00 Lund, Sweden

[2]INFM-Dipartimento di Fisica and IFN-CNR, Politecnico di Milano, Piazza Leonardo da Vinci 32, 20133 Milan, Italy

The effects of tissue heterogeneity on measurements of the scattering and absorption properties of breast tissue was investigated, when time-resolved diffuse spectroscopy and a homogeneous inverse-model is used. Two systems based on picosecond-pulse lasers and single-photon counting detection were employed. The first system utilizes diode lasers at 660 and 785 nm as light sources. The second employs a Ti:sapphire and a mode-locked dye laser to produce tunable pulses in the range 610 – 1000 nm. Using solid tissue phantoms, the systems were rigorously characterized and compared in terms of absolute accuracy of the measured scattering and absorption coefficients, the linearity over the parameter range, the precision with respect to injected light energy, the stability over time, and the reproducibility of the results. The systems were then applied to the problem of *in-vivo* characterization of the absorption and scattering in breast tissue, with the aim of investigating the effects of small heterogeneities always present in real tissue. The results show significant changes in the absorption and scattering properties depending on the subject. Also, measurements at different interfiber distances resulted in distinct optical properties, correlated with the uneven distribution of breast constituents.

Introduction

Measurements of the absorption coefficient μ_a and the reduced scattering coefficient μ_s' of turbid media have become an important part of the developing field of tissue optics. Optical measurements can be performed non-invasively and *in vivo* on patients, and new techniques are emerging as feasible methods for diagnostics of some pathological conditions. An additional advantage of optical methods is that they pose no known health risks, in contrast to for example x-rays. Special attention has been directed to the possibility of detecting cancer tumors in breasts[1]. When applied using a spectroscopic approach, optical methods in the red and near infrared (NIR) region provide the means to yield functional information of the tissue, specifically the abundance of oxygenated and deoxygenated hemoglobin (Hb), water and fat[2,3]. This information could be used to develop

1

contrast functions to distinguish malignant tissue. The goal of this research is an imaging modality which would provide a spatial map of the optical properties over the breast volume[4-10]. By applying spectroscopic evaluation techniques, this information can then be translated to images of the blood perfusion, oxygen saturation, and relative amounts of water and fat. The scattering properties can also provide information on malignancy, because the scattering coefficient will also be affected by structural changes of the tissue.

An important part of this development is to be able to accurately measure the optical properties locally, over small volumes, where μ_a and μ_s' can be assumed to be constant. Spectroscopic *in-vivo* measurements of this kind have been done in order to determine the parameter range of μ_a and μ_s' for healthy tissue, which is strongly influenced by factors such as age and hormonal cycle[2,3,11-13]. The measurement techniques employed are usually either based on frequency-modulated light sources[14] or time-resolved diffuse spectroscopy[15,16]. In general, the breast structure of young women is characterized by dense, glandular and thus water-rich tissue. The post-menopausal breast, in contrast, presents a reduction in the glandular volume, and the relative amount of adipose tissue increases. The structures in the breast are a heterogeneous mix of glandular and adipose tissues. When performing non-invasive measurements *in vivo*, the skin layer presents an additional type of tissue with its own scattering and absorption properties. Previous phantom studies have concluded that the accuracy of the time-resolved technique and homogeneous model is better than 10%[17]. However, there is a growing concern that spatial heterogeneities in the tissue may result in much higher variation. One of the primary aims of this work is to investigate and quantify the effects of the tissue heterogeneity in breast tissue on the evaluated values, performed under the assumption that the tissue is homogeneous when applying the inverse model to deduce the optical properties.

Before using the time-resolved diffuse reflectance systems to examine breast tissue *in vivo*, the performance of the systems was investigated. To this end, we present a rigorous strategy for characterization of instruments, or measurement systems, that are designed for *in-vivo* measurements of the optical properties of tissue. The strategy involves measurements on a set of solid tissue phantoms. The protocol is demonstrated for two time-resolved diffuse spectroscopy systems, whose characteristics are analyzed. Finally, measurements of the optical properties of *in-vivo* breast tissue are presented, involving measurements on four volunteers. The *in-vivo* measurements were performed using different inter-fiber distances, ρ, and thus different sampling depths were probed. A main objective of this examination was to investigate the effects of inhomogeneity of the tissue at

various depths. The results are then discussed in terms of tissue heterogeneity and repeatability of the measurements.

Materials and Methods

Diode-laser based time-resolved system

The first system, henceforth called the "diode laser system," is a portable system constructed at the Lund Medical Laser Centre, Lund, Sweden. The system, schematically depicted in Fig. 1, was designed with the primary objective to perform *in-vivo* measurements of the optical properties in a clinical environment, and specifically the oxygen saturation of the tissue. Moreover, measurements are carried out using relatively small inter-fiber distances, $\rho < 2$ cm, to enable small sampling volumes. This means that the instrument response function (IRF) of the
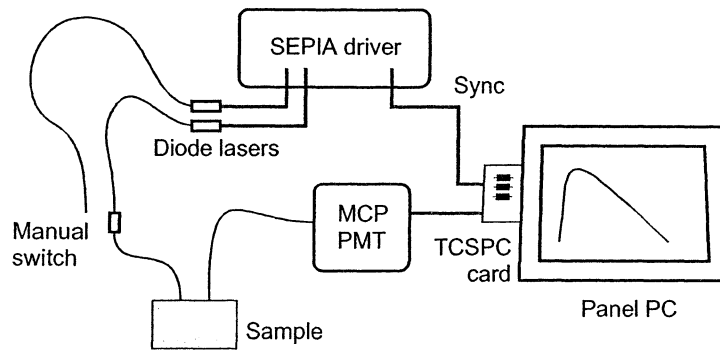
Fig. 1   Schematic picture of the diode laser system.

system must be short, with a full width at half maximum (FWHM) of less than 100 ps. In addition, it means that the average laser power can be kept relatively low, around 2 mW, and the light collection of the detection system does not require the use of thick fiber bundles. As light sources, diode lasers at 660 and 785 nm were used, driven by a SEPIA controller (PicoQuant GmbH, Germany). The light was guided to the sample using 50-μm gradient index fibers. A simple probe was constructed, which enabled diffuse reflectance measurements at different ρ by means of linear translation of the source and detection fibers. To collect the light, a 600-μm step index fiber was used. The length of the collection fiber was < 1 m to minimize mode dispersion broadening of the pulses. A cooled microchannel-plate photomultiplier (MCP-PMT) (R2566U, Hamamatsu Photonics K.K., Japan) was used for detection. The system utilizes the time-correlated single-photon counting (TCSPC) technique to obtain the temporal point-spread function (TPSF)[15]. An SPC-300 computer card (Becker & Hickl GmbH, Germany)

3

provides the electronics for the TCSPC detection, and the system is controlled from a flat panel PC with a touch-sensitive screen. The FWHM of the instrument response function (IRF) for the detection part was approximately 30 ps, and the width of the laser pulses was about 70 ps when the output intensity after the fiber was kept below 2 mW. This resulted in a total IRF of < 100 ps.
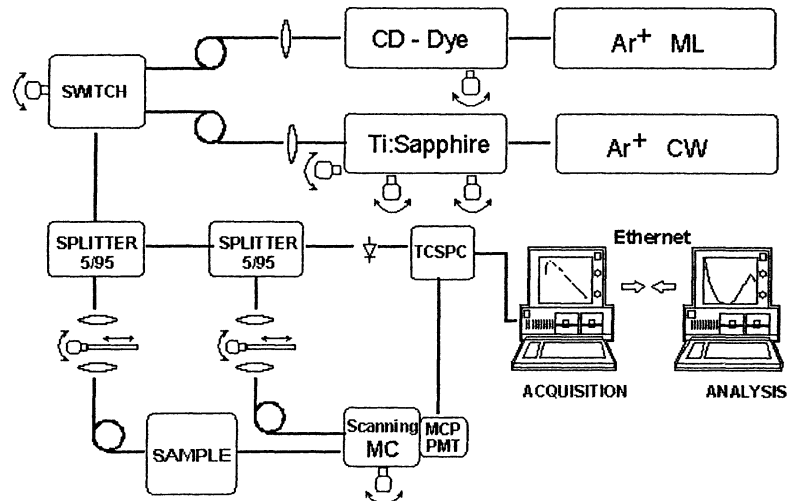
Fig. 2   Schematic picture of the spectroscopy system.

Fully spectroscopic time-resolved system
The second system, henceforth called the "spectroscopy system," is based on wavelength scanning of tunable mode-locked lasers. Figure 2 shows the scheme of the system set-up. A synchronously-pumped mode-locked dye (DCM) laser was used as the excitation source from 610 to 695 nm, while an actively mode-locked Titanium:Sapphire laser provided light in the wavelength range of 700 to 1000 nm. A 1.0-mm plastic-glass fiber (PCS1000W, Quartz et Silice, France) delivered light into the tissue, while diffusely reflected photons were collected by means of a 5 mm diameter fiber bundle. The power density at the distal end of the illumination fibre was always limited to less than 10 mW. A home-built caliper allowed us to position the fibres at the relative distance of 1.5 – 4 cm, parallel to each other and normal to the tissue surface. A cooled MCP-PMT (R1564U with S1 photochatode, Hamamatsu Photonics K.K., Japan) and an electronic chain for TCSPC were used for detection. A small fraction of the incident beam was coupled to a 1.0 mm fiber (PCS1000W, Quartz et Silice, France) and fed directly to the photomultiplier to account for on-line recording of the IRF. Overall, the IRF was <120 ps and <180 ps FWHM in the red and near-infrared, respectively.

4

Time-resolved reflectance curves were collected every 5 nm from 610 to 1000 nm. In order to allow measurements to be carried out *in vivo*, the system for the acquisition of time-resolved data was fully automated and the analysis and display of the measured spectra were performed in real time. A PC controlled the laser tuning and power, the monochromator scanning, and the optimisation of the IRF, by automatically adjusting the laser cavity length. The overall measurement time (for data acquisition and system adjustment) was 5 s/wavelength.

Evaluation of time-resolved data

The absorption and transport scattering coefficients, μ_a and μ_s', respectively, were obtained by fitting the solution of the diffusion equation for a semi-infinite homogenous medium with the extrapolated boundary condition[18] to the measured data. The diffusion coefficient, D, was assumed to be independent of the absorption of the medium, *i.e.*, $D = 1/3\mu_s'$.[19] The theoretical curve was convolved with the IRF. The resulting curve was fitted to the data over a range starting at 80% of the maximum intensity on the rising flank and ending at 1% on the trailing flank. The fit was performed with a Levenberg-Marquardt algorithm[20] by varying μ_a and μ_s' in order to minimize χ^2. The same software was used for evaluation of data for both systems.

Solid tissue phantoms

A set of 25 phantoms was prepared from clear, solvent-free epoxy resin (NM 500, Nils Malmgren AB, Ytterby, Sweden), according to the guidelines given by Firbank et al.[21,22]. As scatterer, TiO powder was used (Sigma-Aldrich, T-8141). As absorbing pigment, toner from the copying machine was used, which had a fairly flat absorption spectrum throughout the visible and NIR region. The toner also had some scattering characteristics, which means that, unfortunately, the absorption coefficient is not trivially obtained from spectrophotometer readings alone. The concentrations of TiO and absorbing pigment are shown in Table 1. The concentrations were selected to reflect a range of μ_a and μ_s' typical of biological tissues. Cylindrical polypropylene cups were used as molds, resulting in phantoms with a diameter of 6.5 cm and a height of 5.5 cm. After hardening, the upper surface was machined smooth. To provide independent validation of the scattering and absorption properties of the phantoms, an integrating sphere set-up was used[23,24]. For the integrating sphere measurements, cuvettes were made of microscope slides into which about 1 ml from each phantom was poured before the epoxy hardened.

5

Protocol for characterization of the two systems

The measurement protocol to characterize the systems consists of five parts, where the first involves determination of the absolute *accuracy* of the measured values. Next, the *linearity* of the results over the parameter range of interest is

Table 1. Concentration of TiO and black pigment added to the phantoms

Phantom (increasing μ_s')	TiO (mg/g)	Phantom (increasing μ_a)	Black pigment (μg/g)
A	0.79	1	6.4
B	1.20	2	13.8
C	1.61	3	21.1
D	2.02	4	28.5
E	2.42	5	35.9

evaluated. The third point is to assess the *precision* of the measurements in terms of the sensitivity with respect to the injected light energy during the recording. Finally, the *stability* of the results over time, and their *reproducibility* between measurement sessions, are evaluated. It should be noted that these points apply to the entire process of determining the optical properties, and thus also depend on the evaluation model used to deduce the scattering and absorption coefficients from the time-resolved data. The system is in this respect viewed as a "black box," where the measurement data are acquired at one end, and the resulting optical properties are obtained at the other. This makes the protocol versatile and useful for any system, from pure research set-ups to commercial instruments. However, the implications of the various parts of the process for determining the optical properties will also be discussed in this paper.

For the measurements of accuracy, linearity, stability and reproducibility, the acquisition time was adjusted so that at least 100 000 counts were collected for each TPSF curve. This represented the minimum desired number of counts during realistic *in-vivo* measurements. Depending on the optical properties of the sample, this meant acquisition times, per TPSF curve, ranging from a few seconds up to a few minutes for the diode laser system at the maximum inter-fiber distance and scattering and absorption coefficients. To determine the absolute accuracy, the whole set of 25 phantoms was measured with the diode laser system. For the spectroscopy system, due to the longer time required to acquire a whole spectrum, 3 scattering series out of 5 were measured, for a total of 15 samples. Thus, the phantoms B1 – B5 and D1 – D5 (cf. Table 1) were excluded from the investigation with this system. To reflect the optimal inter-fiber distances that

each system was designed for, using the diode laser system, $\rho = 1.5$ cm, and using the spectroscopy system, $\rho = 2.0$ cm.

In the next part of the protocol, the precision of the measurements was evaluated by measuring at different amounts of injected light energy per measurement. To this end, a set of 3000 repeated measurements were performed, each 0.1 s long, on one sample (C1, according to Table 1). The inter-fiber distances were $\rho = 1.5$ cm for the diode laser system, and $\rho = 2.0$ cm for the spectroscopy system, to reflect the normal working conditions for each system. These measurements each represented the lowest value of injected energy per measurement. The coefficients μ_a and μ_s' were evaluated for each of the measurements in the set, and then the coefficient of variation (CV) for the results was calculated as

$$CV = \frac{\sigma}{<x>}$$

where σ is the standard deviation and $<x>$ is the mean of either μ_a or μ_s'. In the next step, the measurements were paired, and the average of each pair taken to form a new set, representing twice the value of injected energy per measurement, and new values of μ_a, μ_s', and CV were calculated. This procedure was repeated for increasing values of injected energy, doubling in each step.

For the next step, the stability of the measurements over time was evaluated. Repeated measurements were performed over a period of 2 hours, to investigate any drift in the systems.

Finally, the reproducibility of the measurements was assessed by repeating measurements on the same phantom, with identical measurement parameters, every day for 5 days.

In-vivo measurements
Four healthy volunteers, ages 26, 28, 39, and 50 years, were enrolled for the *in-vivo* measurements after informed consent. The subjects were sitting in an upright position, and the measurement probes were placed on the breast with minimal pressure. Using the diode laser system, measurements were recorded on the right breast of each subject, at five positions: the four quadrants and on the areolar complex. With the spectroscopy system, the whole spectrum from 610 to 1010 nm was acquired on the upper outer quadrant. In addition, with this system, a measurement of the transmitted light was performed when mild compression was applied to the breast. Reflectance measurements were performed at $\rho = 1.0$ and

1.5 cm with the diode laser system, and $\rho = 1.5$, 2.0, 3.0 and 4.0 cm with the spectroscopy system. Changing the inter-fiber distance also changes the sampling depth, and one objective of this examination was to investigate the effects of depth-dependent heterogeneity of the tissue.

For one of the subjects, age 50 years, an additional measurement series was performed repeatedly around one position on the upper outer quadrant of the breast, using the diode laser system and inter-fiber distances of 1.0, 1.5 and 2.0 cm. The probe was placed at six positions over a 1.5 cm by 3 cm area. The objective of this examination was to explore the effects of possible small-scale spatial variations in the composition of the breast, which could have important implications for the repeatability of the measurements when the probe is removed and then replaced at approximately the same postion.

Results

System characteristics

An example of the spectral characteristics of the solid phantoms, measured with the spectroscopy system, is presented in Fig. 3. The peaks in the absorption spectrum around 900 nm stems from the epoxy. Below 800 nm, the epoxy absorption has been reported to be fairly flat at 0.01 cm^{-1},[22] so most of the absorption in this region is due to the black pigment. The determined values of μ_a and μ_s' for both systems, at 660 nm, are presented in Fig. 4. The values for μ_s' from the integrating sphere meaurements are also shown for comparison.
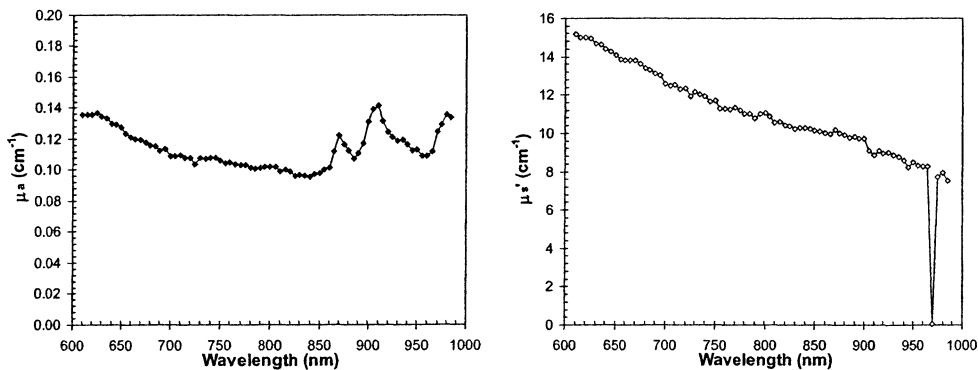

Fig. 3 (a) Absorption spectrum of phantom C2, measured with the spectroscopy system. (b) Scattering spectrum.

Results for the linearity in μ_a are presented in Fig. 5, for both systems, with $\rho = 1.5$ cm for the diode laser system, $\rho = 2$ cm and for the spectroscopy system.

The absorption coefficients are shown as function of the concentration of black pigment, evaluated at 660 nm, for the phantoms with lowest (row A) and highest (row E) scattering coefficient, respectively. The linearity in scattering is presented in Fig. 6, for the phantoms with lowest (row 1) and highest (row 5) absorption coefficient, respectively. The lowest values of scattering (row A) were left out when calculating the regression line in Fig. 6 (a). The results were similar for the evaluation of the diode laser system at 10 mm (data not shown). Since only three scattering concentrations were measured using the spectroscopy system, it is difficult to evaluate the linearity in this case, but the data in Fig. 6 (b) is included for completeness.

The results from the evaluation of precision are presented in Fig. 7. The evaluation of the stability over time of the systems revealed that no drift was apparent when performing measurements over a period of 2 hours. During the measurement series, the only varition in the readings was the stochastic variation as shown in Fig. 7. Finally, the reproducibility measurements, taken every day over 5 days, showed a slightly higher standard deviation, but the *CV* was in all cases less than 5%.

In vivo measurements of breast tissue
Figure 8 (a) compares the absorption spectra obtained on the 4 volunteers for $\rho = 2$ cm in the upper outer quadrant of the breast. The corresponding scattering spectra are reported in Figure 8 (b).

Figure 8 (c) reports the absorption spectra for the 26-year-old volunteer. Three measurements are reported, corresponding to reflectance spectra with $\rho = 1.5$ cm (empty diamonds) and $\rho = 4.0$ cm (filled diamonds), together with the transmittance spectrum (empty squares). The scattering spectra on the same volunteer are displayed in Fig. 8 (d).
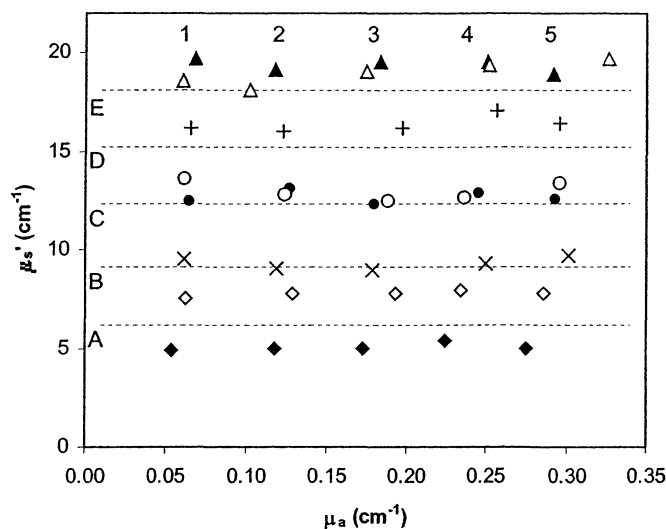
Fig. 4 Values of absorption and scattering coefficients of the phantoms, at 660 nm, evaluated with both systems. Filled and crossed symbols are for the diode laser system, and empty symbols are for the spectroscopy system. Note that rows B and D for scattering were not measured with the spectroscopy system, so the data shown are for rows A, C and E for this system. The dashed lines represent the average values from the integrating sphere measurements for rows A – E. Absorption data from the integrating sphere is not shown.

Fig. 5 Linearity test showing the absorption coefficient as a function of the concentration of black pigment in the phantoms. Data are shown for rows A and B, according to Table 1. (a) The diode laser system. (b) The spectroscopy system.

The results from the measurements using different inter-fiber distances are shown in Fig. 9. Finally, the results from the measurement over a 1.5 by 3 cm grid on the upper outer quadrant of the 50-year-old volunteer are presented in Fig. 10.

Discussion

System characteristics

In terms of absolute accuracy of the determined values of μ_a and μ_s', some problems are associated with the solid phantoms. The exact properties of the phantoms are unknown, although the independent integrating sphere measurements likely give values of μ_s' that are within 5% accurate. Integrating sphere measurements are less accurate for the absorption coefficient, but it is reasonable to assume that the true absorption is linearly related to the concentration of black pigment. When preparing the phantoms, much care was taken to mix the resin, TiO, and black pigment, both mechanically and using an
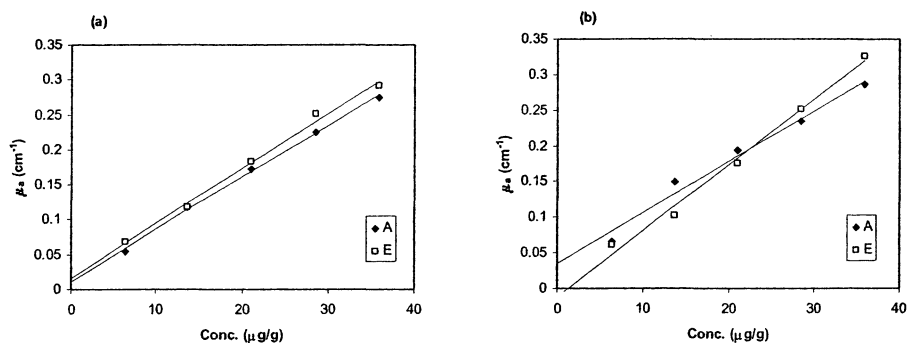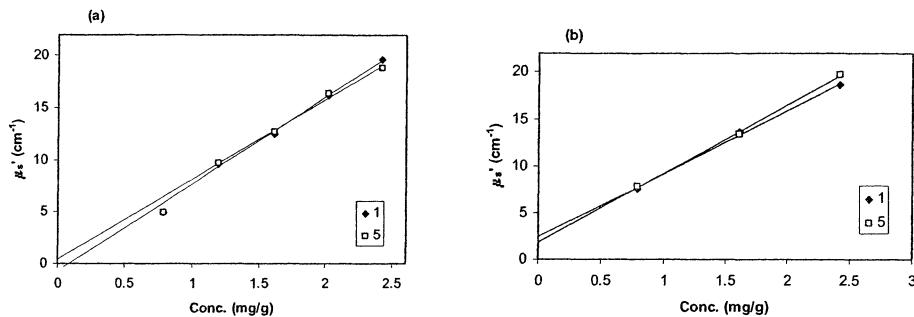

Fig. 6 Linearity test for the scattering coefficient as a function of the concentration of TiO in the phantoms. Data are shown for rows 1 and 5, according to Table 1. (a) Diode laser system. Note that the data points for the lowest scattering were left out of the calculation of the regression line. (b) Spectroscopy system.

ultrasonic bath, and it is unlikely that there were significant inhomogeneities in the phantoms. The results presented in Fig. 4 indicate that the accuracy for both systems is better than 10% within the parameter range defined the B – C phantoms, but slightly worse for the low-scattering A phantoms.

With respect to linearity, from Fig. 5, it is apparent that the evaluation of μ_a was linear over the entire parameter range. Turning the attention to the scattering coefficient, the expected linear behavior of μ_s' deviates slightly for the lowest concentration of scatterer. This may be the result of entering the regime where the diffusion approximation used in the evaluation is no longer entirely valid, i.e., the detection position cannot be regarded as far away from the source. The results were similar for all inter-fiber distances, which is somewhat surprising, since one would expect worse linearity for short inter-fiber distances where the diffusion approximation loses validity. The explanation may be that there was a break-point somewhere between the phantoms with the lowest scattering coefficients, which

11

was not detected because the concentration step (from 0.79 to 1.20 mg/g TiO) was too large. The conclusion is that μ_a was linear over the entire range up to 0.3 cm^{-1}, while μ_s' was linear for $\mu_s' > 9$ cm^{-1}, and slightly underestimated (20 – 30%) at 6 cm^{-1}. It is difficult to draw conclusions about the linearity of the spectroscopy system based on only three points. It is possible that the larger collection area of the fiber bundle, which made the inter-fiber distance less well defined, became more important for the low-scattering samples.

In the next part, the precision of the measurements was investigated in terms of CV for various levels of injected energy per measurement, as presented in Fig. 7. For time-resolved instruments, CV is largely determined by the number of counts in the TPSF, N, primarily due to the noise, which is proportional to $N^{1/2}$. The contribution of noise by the dark current in the detectors was negligible for both systems. Translated to injected energy per measurement, the relationship with N is dependent on the average power, the collection efficiency and sensitivity of the detection system, the inter-fiber distance, and the properties of the sample. Due to
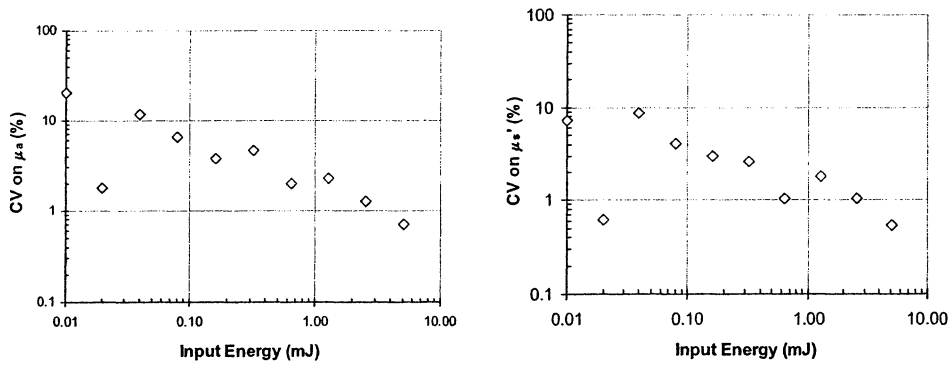

Fig. 7 Results from the precision measurement, showing CV as a function of the input energy during the recording. (a) CV on μ_a for the spectroscopy system. (b) CV on μ_s' for the spectroscopy system. The count rate was 100 000 counts/s during the measurement.
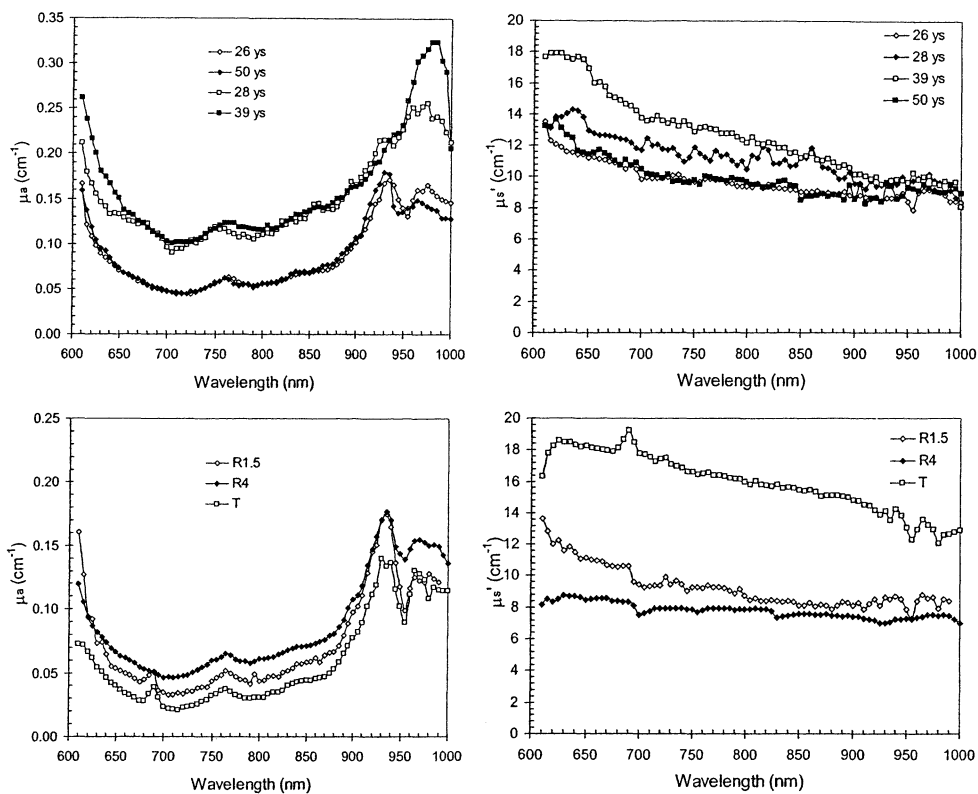
Fig. 8 (a) Absorption spectra from all volunteers, presented for ρ = 2.0 cm. (b) Scattering spectra. (c) Absorption spectra from the 26-year-old volunteer, presented for ρ = 1.5 cm and 4 cm, as well as in transmittance mode. (d) Scattering spectra.

the much lower collection efficiency of the diode laser system, higher levels of injected energy per measurement were needed to get gthe same order of CV as for the spectroscopy system.

The stability results revealed no drift in any of the systems. TCSPC measurements are largely insensitive to drift in the intensity of the laser pulses, but temporal shifts can cause problems if the IRF is not monitored simultaneously with the measurements. On-line monitoring of the IRF was performed for the spectroscopy system, but not for the diode laser system. In this test, no drift was apparent in the diode laser system, but nevertheless, we recommend that on-line measurements of the IRF are carried out.

The final part of the solid-phantom protocol was the reproducibility of the results. It was evident that $CV < 5\%$ for measurements performed under identical

13

conditions on different days. The conclusion is that reproducibility is not a limiting factor as far as the instrumentation is concerned.

In-vivo measurements on breast tissue
Results presented in Fig. 8 (a) – (b) clearly shows marked variations in the breast spectral features of the 4 volunteers. Concerning the absorption spectra, there are differences in the red region of the spectrum possibly ascribed to a different blood concentration as well as an uneven contribution of water and lipids absorption around 970 and 930 nm, respectively. The scattering spectra are less diverse, but can be revealed as differences both in absolute value and in slope. Overall, these spectral differences are not correlated with the age of the subject but seem to be rather dependent on the breast structure. Indeed, according to the standard classification of x-ray mammographies, different breast types can be identified depending on the glandular or adipose tissue prevalence. Upon increasing the age the lipid content augments, but large variations in breast types are observed for the same ages.The spectra in Fig. 8 (c) – (d) reveal that upon increasing the inter-fiber distance in reflectance, the absortion coefficient shows a significant increase between 700 and 850 nm as well as beyond 950 nm in the water absorbing region, whereas the lipid peak around 930 nm is almost unchanged. The transmittance spectrum is always lower in absorption and shows an almost balanced contribution of the lipid and the water peak. This behavior is indicative of an increase in the water content upon increasing the inter-fiber distance, counterbalanced by a lower lipid content. Also the hemoglobin contribution is increased for larger ρ. For the transmittance measurement the water-to-lipid ratio increases even more, while blood absorption is evidently lower. Overall, these spectra are consistent with the known structure of the breast[25]. The more superficial regions-layer-tissues are more adipose and host major blood vessels. On the other hand the mammary gland – presumably water rich - is located in the core. These same observations are generally confirmed by the measurements obtained on the other 3 volunteers, even though the initial pattern was quite different in terms of prevalence of the water or of the lipid peak.

With regard to the scattering spectra, both the absolute values of μ_s', and the steepness of the slope, are abruptly increased for the transmittance measurement, as compared with the reflectance. Some differences between the reflectance spectra are also seen and correspond to a decrease in slope steepness upon increasing the interfiber distance. The same trend was confirmed on all the volunteers (data not shown). The dependence of the scattering coefficient on the

wavelength can be described by a power law derived – empirically – from Mie theory[26,27], where the exponent (i.e. the slope of the spectrum in a log scale) is related to the mean effective size of scattering centres, while the amplitude is affected by the density of scattering centres. Thus, the steepest spectrum observed in transmittance is characterised by a higher exponent of the power law that corresponds to smaller effective scattering centres. One could speculate whether this can be related to the presence of the mammary gland, with a typical fibrous structure of the parenchyma. The parenchyma is rich of small collagen fibrils, that can be responsible for a steep dependence on wavelength.

The data in Fig. 9, where the effect of different inter-fiber distances was investigated in more detail, reveal that in general, the variation between different inter-fiber distances is fairly small. The absorption changes somewhat according to the discussion above for the spectra, and a general effect seems to be higher scattering for the shortest ρ, an indication of higher scattering in the superficial layers that are then sampled. The conclusion is that in order to sample tissue that is representative of the deeper structures, measurements with more that approximately 1.5 cm should be carried out. It should be noted that some of the measurements on the areolar complex fitted very poorly to the diffusion equation, likely because of relatively high absorption and low scattering.

Fig. 9 Data from the diode laser system, with different inter-fiber distances over the four quadrants and the areola. Diamonds – upper inner quadrant; squares – lower inner quadrant; triangles – lower outer quadrant; crosses – upper outer quadrant; cross/vertical bar – areola. (a) The 26-year-old volunteer. (b) The 28-year-old volunteer.
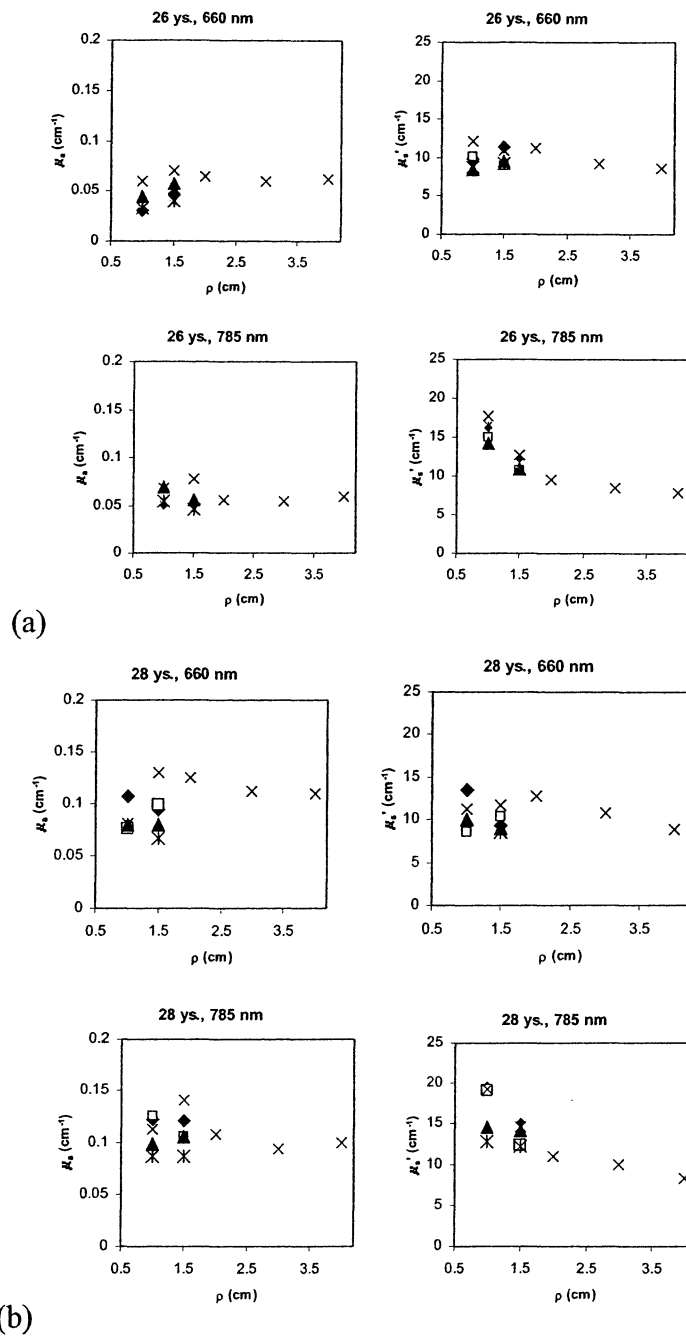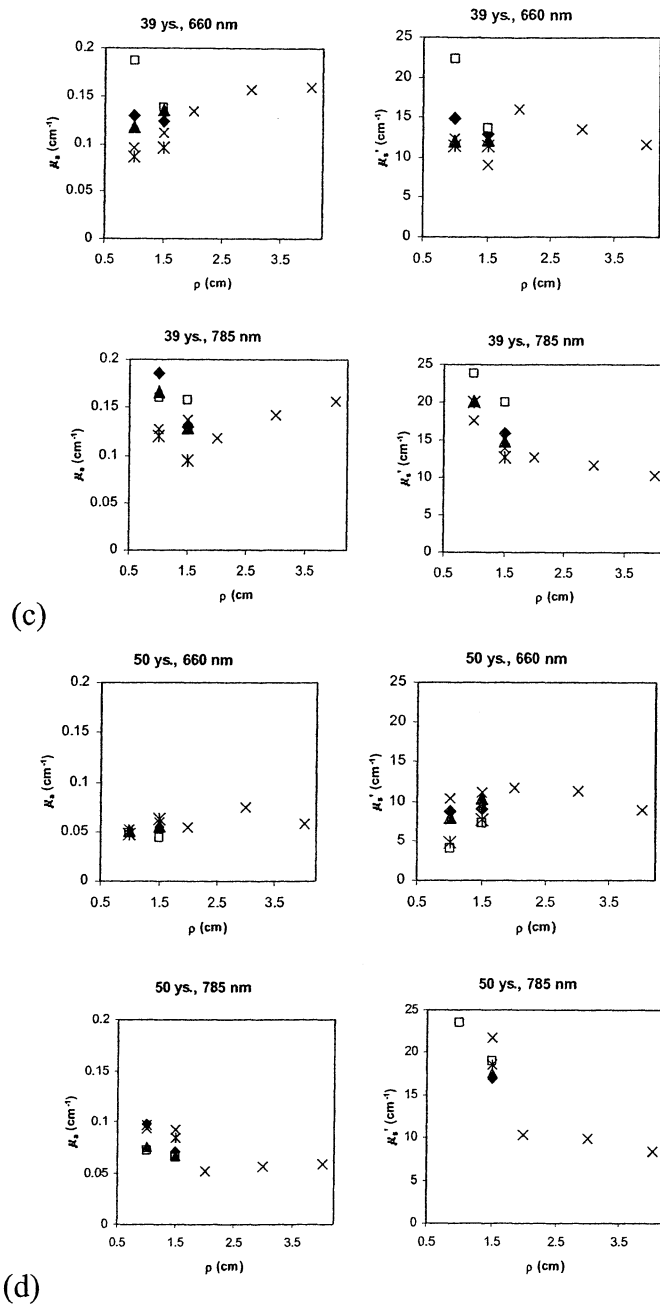
(c)

(d)

Fig. 9 Data from the diode laser system, with different inter-fiber distances over the four quadrants and the areola. Diamonds – upper inner quadrant; squares – lower inner quadrant; triangles – lower outer quadrant; crosses – upper outer quadrant; cross/vertical bar – areola. (c) The 39-year-old volunteer. (d) The 50-year-old volunteer.
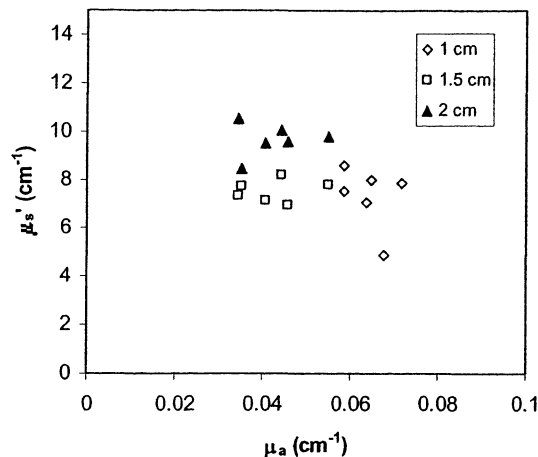
Fig. 10 The results when when moving the probe over a 1.5 cm by 3 cm area on the upper outer quadrant.

Additional important observations can be made in Fig. 10, where the measurement probe was shifted slightly around one position of on the breast. The determined values of μ_a and μ_s' – for each inter-fiber distance – are relatively closely confined. Thus, lateral spatial heterogeneity on the scale of around 1 cm does not seem to have major influence on the measurements.

Conclusions

In conclusion, two time-domain diffuse spectroscopy systems were characterised in terms of accuracy, linearity, precision, stability and reproducibility. The results show that the systems were capable of determining the absorption and reduced scattering coefficient with an accuracy of 10% within the parameter range $9 < \mu_s' < 20$ cm^{-1} and $0 < \mu_a < 0.3$ cm^{-1}. For lower scattering, down to 6 cm^{-1}, the relative error in μ_s' was slightly worse at about 20 – 30%. The precision of the measurements was better than 1% if 100 000 counts per TPSF curve were acquired. In terms of stability, no drift in the readings was detected, and the day-to-day reproducibility was better than 5%.

In an effort to investigate the effects of heterogeneity when performing *in-vivo* measurements on breast tissue, different inter-fiber distances were employed in reflectance mode, and a transmittance measurement was also performed. The results indicate that the absorption coefficient is influenced by the different chromophores at different depths from the skin surface, but the variation between subjects was much larger than the variation due to different sampling depths or

18

different positions in the breast. In terms of the reduced scattering coefficient, higher values were obtained for the shorter inter-fiber distances, when mostly the skin and the very superficial layers are probed, and the results show that to obtain representative information about the deeper tissue structures, larger inter-fiber distance than about 1.5 cm is needed.

Acknowledgements

References

1. R. Berg, O. Jarlman, and S. Svanberg, "Medical transillumination imaging using short-pulse diode lasers," Appl. Opt. **32**, 574-579 (1993).
2. R. Cubeddu, A. Pifferi, P. Taroni, A. Torricelli, and G. Valentini, "Noninvasive absorption and scattering spectroscopy of bulk diffusive media: An application to the optical characterization of human breast," Appl. Phys. Lett. **74**, 874-876 (1999).
3. N. Shah, A. Cerussi, C. Eker, J. Espinoza, J. Butler, J. Fishkin, R. Hornung, and B. Tromberg, "Noninvasive functional optical spectroscopy of human breast tissue," Proc. Natl. Acad. Sci. USA **98**, 4420-4425 (2001).
4. S. Fantini, S. A. Walker, M. A. Franceschini, M. Kaschke, P. M. Schlag, and K. T. Moesta, "Assessment of the size, position, and optical properties of breast tumors *in vivo* by noninvasive optical methods," Appl. Opt. **37**, 1982-1989 (1998).
5. D. Grosenick, H. Wabnitz, H. H. Rinneberg, K. T. Moesta, and P. M. Schlag, "Development of a time-domain optical mammograph and first in vivo applications," Appl. Opt. **38**, 2927-2943 (1999).
6. M. J. Holboke, B. J. Tromberg, X. Li, N. Shah, J. Fishkin, D. Kidney, J. Butler, B. Chance, and A. G. Yodh, "Three-dimensional diffuse optical mammography with ultrasound localization in a human subject," J Biomed Opt **5**, 237-247 (2000).
7. J. C. Hebden, H. Veenstra, H. Dehghani, E. M. C. Hillman, M. Schweiger, S. R. Arridge, and D. T. Delpy, "Three-dimensional time-resolved optical tomography of a conical breast phantom," Appl. Opt. **40**, 3278-3287 (2001).
8. C. H. Schmitz, M. Locker, J. M. Lasker, A. H. Hielscher, and R. L. Barbour, "Instrumentation for fast functional optical tomography," Rev. Sci. Instrum. **73**, 429-439 (2002).
9. R. Cubeddu, G. M. Danesini, E. Giambattistelli, F. Messina, L. Pallaro, A. Pifferi, P. Taroni, and A. Torricelli, "Time-resolved optical mammograph for clinical studies beyond 900 nm," in *OSA Biomedical Topical Meetings, OSA Technical Digest,* Proc. Opitcal Society of Ametica, Washington DC OSA, 2002), pp. 674-676.
10. T. O. McBride, B. W. Pogue, S. Poplack, S. Soho, W. A. Wells, S. Jiang, U. L. Österberg, and K. D. Paulsen, "Multispectral near-infrared tomography: a case study in compensating for water and lipid content in hemoglobin imaging of the breast," J Biomed Opt **7**, 72-79 (2002).
11. B. J. Tromberg, N. Shah, R. Lanning, A. Cerussi, J. Espinoza, T. Pham, L. O. Svaasand, and J. Butler, "Non-invasive in vivo characterization of breast tumors using photon migration spectroscopy," Neoplasia **2**, 26-40 (2000).
12. A. Cerussi, A. J. Berger, F. Bevilacqua, N. Shah, D. Jakubowski, J. Butler, R. F. Holocombe, and B. J. Tromberg, "Sources of absorption and scattering contrast for near-infrared optical mammography," Acta Radiol. **8**, 211-218 (2001).
13. A. E. Cerussi, D. Jakubowski, N. Shah, F. Bevilacqua, R. Lanning, A. J. Berger, D. Hsiang, J. Butler, R. F. Holcombe, and B. J. Tromberg, "Spectroscopy enhances the information content of optical mammography," J Biomed Opt **7**, 60-71 (2002).
14. S. J. Madsen, E. R. Anderson, R. C. Haskell, and B. J. Tromberg, "Portable, high-bandwidth frequency-domain photon migration instrument for tissue spectroscopy," Opt. Lett. **19**, 1934-1936 (1994).
15. S. Andersson-Engels, R. Berg, O. Jarlman, and S. Svanberg, "Time-resolved transillumination for medical diagnostics," Opt. Lett. **15**, 1179-1181 (1990).
16. R. Cubeddu, M. Musolino, A. Pifferi, P. Taroni, and G. Valentini, "Time resolved reflectance: a systematic study for the application to the optical characterization of tissue," IEEE J. Quant. Electr. **30**, 2421-2430 (1994).
17. R. Cubeddu, A. Pifferi, P. Taroni, A. Torricelli, and G. Valentini, "Experimental test of theoretical models for time-resolved reflectance," Med. Phys. **23**, 1625-1633 (1996).

18. R. C. Haskell, L. O. Svaasand, T.-T. Tsay, T.-C. Feng, M. S. McAdams, and B. J. Tromberg, "Boundary conditions for the diffusion equation in radiative transfer," J. Opt. Soc. Am. A **11**, 2727-2741 (1994).

19. K. Furutsu and Y. Yamada, "Diffusion approximation for a dissipative random medium and the applications," Phys. Rev. E **50**, 3634-3640 (1994).

20. W. H. Press, S. A. Teukolsky, W. T. Vetterling, and B. P. Flannery, *Numerical recipes in C: The art of scientific computing*, (Cambridge University Press, New York, 1992).

21. M. Firbank and D. T. Delpy, "A design for a stable and reproducible phantom for use in near infra-red imaging and spectroscopy," Phys. Med. Biol. **38**, 847-853 (1993).

22. M. Firbank, M. Oda, and D. T. Delpy, "An improved design for a stable and reproducable phantom material for use in near-infrared spectroscopy and imaging," Phys. Med. Biol. **40**, 955-961 (1995).

23. A. M. K. Nilsson, R. Berg, and S. Andersson-Engels, "Measurements of the optical properties of tissue in conjunction with photodynamic therapy," Appl. Opt. **34**, 4609-4619 (1995).

24. J. Swartling, J. S. Dam, and S. Andersson-Engels, "Comparison of spatially and temporally resolved diffuse-reflectance measurement systems for determination of biomedical optical properties," (2002). Manuscript.

25. S. Thomsen and D. Tatman, "Physiological and pathological factors of human breast disease that can influence optical diagnosis," Ann. N. Y. Acad. Sci. **838**, 171-193 (1998).

26. J. R. Mourant, T. Fuselier, J. Boyer, T. M. Johnson, and I. J. Bigio, "Predictions and measurements of scattering and absorption over broad wavelength ranges in tissue phantoms," Appl. Opt. **36**, 949-957 (1997).

27. A. M. K. Nilsson, C. Sturesson, D. L. Liu, and S. Andersson-Engels, "Changes in spectral shape of tissue optical properties in conjunction with laser-induced thermotherapy," Appl. Opt. **37**, 1256-1267 (1998).